Title Page

Principal Investigator:

Ugur Ozbay, Ph.D., Pr. Eng.
Professor of Mining Engineering
Colorado School of Mines
1500 Illinois Street
Golden, Colorado 90401

Tel: 303 273 3710
Email: mozbay@mines.edu

Title:

Improving the understanding of dynamic failures and massive collapses in coal mines using numerical modeling

Grant number

1R01OH009764-01

The project starting and ending dates

09/1/2009 – 08/31/2013

Final Report Submission

November 8, 2013

Table of Contents

List of Figures

List of Tables

List of Terms, Abbreviations, and Symbols

Terms

Unstable failure: A sudden failure of rock due to release of stored potential energy accompanying violent expulsion of rock or coal fragments.

Failure stability: Whether failure in rock occurs in a stable or unstable manner.

Rockburst: An unstable failure in a mine or underground excavation that results in injury to personnel or damage to equipment or underground workings that cause operational delays.

Coal bumps: Same as rockbursts, but occur in coal mines.

Slip-type event: Unstable failure which initiates in shear along a large discontinuity plane, such as faults bedding planes.

Longwall mining: A method of full extraction mining where large movable hydraulic shields are used to temporarily prevent the immediate roof from collapsing while a shearer mines the longwall face.

Room-and-pillar mining: A method of partial extraction in which an array of rock pillars is left in place throughout mining to support the roof and overburden.

Retreat mining: A form of secondary mining in room-and-pillar layouts in which primary support pillars are mined and the roof is allowed to cave behind the active mining area.

Coal rib or rib: Refers to vertical excavation sides or unconfined pillar sides.

Abbreviations

Universal Distinct Element Code	UDEC
Continuously yielding	CY
Uniaxial compressive strength	UCS
Finite Element Method	FEM
Boundary Element Method	BEM
Discrete Element Method	DEM
Finite Difference Method	FEM
Fast Lagrangian Analysis of Continua	FLAC
U.S. Bureau of Mines	USBM
National Institute for Occupational Safety and Health	NIOSH
Particle Flow Code	PFC
Mohr-Coulomb	MC
Mohr-Coulomb strain softening	MCSS

Symbols

normal stress (Pa).	σ
normal strain	ε
stiffness (Pa/m)	k
loading system stiffness (Pa/m)	k_{ls}
post-peak stiffness (Pa/m)	k_{pp}
shear stress (Pa).	τ
coefficient of friction	μ
elastic modulus (Pa)	E
Poisson’s ratio	ν
shear displacement (m).	u_s
friction angle (deg)	ϕ
failure or “bounding” shear stress (Pa).	τ_m
material density (kg/m3]	ρ
Mohr-Coulomb friction angle (deg.)	ϕ
plastic strain	ε_p
excess energy (J)	E_e
boundary work (J)	W_b
gravitational potential energy (J)	Wg
elastic strain energy (J)	U
plastic work (J)	W_r
kinetic energy (J)	E_k
damped kinetic energy (J)	Wk
strength of pillar (Pa)	S_p
cubic compressive strength of rock (Pa)	S_t
height of pillar (m)	h
length of pillar (m)	L
width-to-height ratio of a pillar	w/h

Abstract

Events of violent rock failures in deep coal mines, which are commonly known as “bumps”, pose a serious threat to the safety of mine workers. The infamous Crandall Canyon disaster in Utah in 2007 was a tragic large coal bump event that claimed nine lives. Bumps of such magnitudes are low frequency, high impact events, although smaller magnitude bumps are also a reason for concern in deep coal mines. The underlying mechanism of bump events is complex and involves “unstable” failures in excavation walls triggered by a sudden release of stored energy from the surrounding rockmass. The objective of this research is to improve the mechanistic understanding of unstable failures to develop design methodologies for protecting miners against the perils of coal bump events. This report describes the research carried out for improving the mechanistic understanding of unstable failures using numerical modeling and presents the results obtained. In addition to this report, the research outcomes are also published in three PhD theses and several technical publications in scientific journals and conference proceedings.

The research makes use of the commercially available finite difference and discrete element based numerical modeling codes, namely FLAC, FLAC3D, UDEC, 3DEC, PFC, and PFC3D. In all modeling cases, the rockmass is modeled as an elastic material in the pre-failure state and as a plastic or brittle material during failure. Significant emphasis is placed on validating the ability of these models to identify failure stabilities under compressive and shear loads. The failure stability concept is based on the theory that a failure becomes unstable if the failing rock is unable to fully absorb the strain energy provided by the elastically loaded rockmass.

The FLAC/3D modeling focuses on developing instability identifiers that can be used for evaluating the locations and relative magnitudes of unstable failures within a rockmass. An energy balance is introduced for calculating the excess energy released as a result of unstable equilibrium in a rockmass. The identifiers and excess energy calculations provide a generalized methodology for assessing unstable failures within potentially complex mine models. They may be applied to the design of mine layouts in bump-prone conditions or to perform backanalyses on unstable failures in select mining layouts. The UDEC modeling studies cover rock failures under compression and discontinuity shear loading conditions. Using a double shear test model, methodologies are introduced for identifying shear failure stabilities both in laboratory and in-situ scale models. The modeling results show that rock-coal interfaces may fail in a stable or unstable discontinuity shear mode depending on the post-peak characteristics of the discontinuity interface and the shear stiffness of the interface. Also shown is that unstable coal sidewall and mining face failures can occur when a sudden de-confinement is triggered by an unstable failure at the rock-coal interfaces or by the existence of weak contact regions along the interfaces. The PFC simulations focused on failure stability analyses in compression using the bonded particle and the displacement softening contact models. A mechanically coupled finite difference and discrete element model of coal is utilized to study the effect of geometry and loading system stiffness on pillar failure stability. A transition from stable to unstable failure was observed when the loading system stiffness was less than the post-peak stiffness of the coal. Stiffness measurements showed unstable and stable failures by assigning different moduli to the loading system. Damping work in PFC simulations appears particularly useful as a failure indicator as it is observed to be consistently higher during unstable failures. The results reveal shortcomings in the bonded particle model and promote the displacement-softening contact model for continued studies of rock failure stabilities.

Section 1 of the Final Progress Report

Significant Findings: The study enhances the mechanistic understanding of unstable failure events commonly known as “bumps” in deep coal mines through applications of advanced numerical models. The newly introduced numerical modeling procedures are shown to aid in assessing the propensity of potential bump events.

Evaluations of the available numerical modeling software have shown that explicit, time-dependent codes are well suited for the studies of unstable failures of rocks. Both two- and three-dimensional versions of the explicit finite difference codes FLAC, UDEC, and PFC were found to be suitable for such studies. The Mohr-Coulomb strain-softening constitutive model was adapted for modeling compression-induced softening that may lead unstable failures in rock. Careful determination is required when selecting zone size for the strain-softening model to prevent failure from localizing along unrealistically small-width bifurcation planes. The continuously yielding joint constitutive model in UDEC and 3DEC is found to model unstable failures in shear along existing large geological discontinuities while the strain-softening model operates in the compressive failure regions. For FLAC3D modeling, identifiers of unstable failures are developed to assess the onset, duration, and location of instability. Maximum unbalanced forces and accelerations correspond to the point of greatest instability when the difference is highest between the applied stress and the residual strength of the specimen. Maximum velocities result from sustained accelerations during instability and correspond to the final point of instability as the rock system regains static equilibrium. An energy balance equation was developed which provides a determination of the magnitude of excess energy released as a consequence of unstable equilibrium. When using strain softening material, the magnitudes of excess energy released in FLAC3D UCS tests match theoretical calculations of energy released due to unstable failure. The same tests using perfectly plastic Mohr-Coulomb rock properties show only nominal releases of excess energy as is expected from this inherently stable material. 2D models of local loading stiffness for 1:1 and 2:1 width-to-height ratio pillars behave similarly in failure to slender UCS test specimens. Wider pillar geometries of 3:1 and greater introduce a more complex failure mode which progresses from the rib and propagates into the strong central core of highly confined rock. Unstable failure was observed in the 1:1 to 5:1 pillars for all cases in which the Young's modulus of the rockmass was modeled as 2 GPa or less.

Several conditions are found to affect the potential for and intensity level of unstable discontinuity shear failures. Mining advances change the loading stiffness of the surrounding rockmass, which in turn affects the stability of discontinuity shear failures and can result in both stable and unstable shear failures along existing rock discontinuities. The signatures of unstable failures in UDEC models are found to be sudden, discontinuous changes in stress and displacement along the discontinuity planes in the rock material, as compared to smooth and gradual response in the case of stable failures. Competent wall rocks with unaltered rough surfaces coupled with extensive mining are favorable factors for unstable shear failures to occur in underground mines. The likelihood and intensity of unstable shear failures are observed to increase with i) increased normal stress on the discontinuity, ii) the extent of mining, iii) decreasing distance between the discontinuity and excavation, and iv) reduced elastic modulus of rock. Unstable shear failures at coal-rock interfaces can also cause unstable compressive failures in coal layers resulting in violent rib failures. Patches of weak regions at coal-rock interfaces possibly promote de-confinement which causes unstable compressive failures at mining faces and sidewalls.

A genetic algorithm was developed to calibrate the many input parameters of DEM to achieve desired macro properties in a straightforward manner through multi-objective optimization. The brittle bonded-particle discrete element models which were developed simulated unstable failures observed in controlled laboratory UCS tests using DEM software PFC3D. The post-failure modulus of the bonded-particle model in PFC3D was found to be highly dependent on loading rate even for previously assumed quasi-static loading conditions. No characteristic post-peak strength behavior could be defined for the UCS specimen, even in cases of stable failure. Long computation times, limited applicability to study large rock structures, and post-failure modulus load rate dependency of the bonded-particle model made its use infeasible for the intended studies on mine layouts and realistic underground mining conditions. Overall, application of discrete element modeling is a promising, and potentially the most appropriate, code for modeling rock brittleness. However, it is not yet a sufficiently practical model for modeling unstable failures for day-to-day mine design in bump or rockburst prone mines.

<u>Translation of findings:</u> The study furthers the knowledge on mechanisms of bump events as they occur in coal mines. Using the modeling methodologies introduced, mine designers can perform failure stability analyses for comparing bump proneness in different mine layouts. Many numerical modeling algorithms called through FISH functions have been developed from the study which may be used in developing numerical models for failure stability analysis.

For an effective application of the numerical modeling methodologies, the rockmass properties within an area of interest need to be known in sufficient detail. This aspect is still outstanding and limits the use of the modeling methodologies as a coal mine bump mitigation tool. Extensive backanalysis studies are needed to improve the efficacy of numerical modeling as a design tool in bump prone mines.

<u>Outcomes / Impact:</u> The advances made through this research enhance the effectiveness of numerical modeling practices for failure stability analysis in deep underground mines. The numerical modeling methodologies introduced by this research offer additional dimensions to mine design. The improved mechanistic understanding of failure stabilities and the ability to evaluate available excess energy released during unstable failures are likely to reduce the safety risk associated with coal bumps. Using best estimates of rockmass properties, comparison modeling of different mine designs can be performed for ranking them by their bump potential. If used frequently, the modeling methodologies developed by this research should show increasingly improved bump related safety in coal mines within a few years.

The developed modeling methodologies need to be calibrated and validated extensively against well documented case histories of bumps. As modeling practices improve with increased case history backanalysis efforts, their importance in mine design is likely to further develop from complementing empirical designs with rationally based numerical approaches in bump prone conditions

This report presents the main body of the research work with sufficient explanations to put the methods into practice in order to benefit from these research findings. Readers interested in further details of the numerical models and related codes are referred to the three Ph. D. theses which are fully based on the work of this research project and referenced in the “Publications” section of this report.

Section 2 of the Final Progress Report

1. BACKGROUND

Rock around underground mining excavations may fail if its strength is overcome by the stresses induced by progressive mining. Generally, the stress induced failure occur gradually and failed rock around excavations is supported or left alone depending on the safety considerations and other factors such as the mining method being practiced. In certain cases of mining being conducted at considerable depths in brittle rock, the stress induced failures may take place suddenly, resulting in rapid ejection of rock fragments from the excavations walls. Such violent failure events, which are known as rockbursts in hard rock mines and bumps in coal mines, pose a serious threat to worker safety. In coal mines, violent failures may involve ejection of several tons of coal fragments from coal faces without much warning. The infamous Crandall Canyon disaster [20] that took lives of nine persons in 2007 is an example of a high magnitude bump event. An improved understanding of the mechanisms of bump events can help designing safer mining layouts and practices against injurious bump events in deep coal mines.

A historical view of rockburst and bumps

The earliest documented rockburst event seems dates back to 1738, which was associated with mining in the British Derbyshire lead ore mine [7]. Since then, rockbursts have been recorded in many countries for underground mining operations in both hard rock mines and coal mines. Rockbursts were observed in ore mining in Czech Republic, United Kingdom, South Africa and Australia; in salt mining in Germany and France; and in stone and underground coal mining.

In South Africa, rockbursts became a major hazard in the Witwatersrand gold mines at the beginning of the 20th century [13]. It was believed that the very deep and extensive tabular mining were the factors that made rockburst hazards in this region the most severe ones in the world [44]. These hazards used to account for as many as 100 fatalities per year [21]. In Canada, the first recorded rockburst occurred in 1928 [44]. In the beginning of 1980's, rockbursts became a growing problem in Northern Idaho hard rock mines. From 1984 to 1986, there were about 325 rockburst events occurred in Eastern Canada, as shown in Table 1-1 [23]. In Australia, rockbursts were first recognized as a major but relatively occasional problem in the Kalgoorlie district in the early 1900's [23]. With increasing extraction ratios and depths of orebodies, an increased prevalence of rockburst problems had been experienced in the last decade of the 20th century. In India, the occurrence of a rockburst was first reported in the Kolar Gold Field in Mysore in 1928. The Kolar Gold Field is located in southeast India, and the mining operations were at depth of 2000 meters and greater [33]. As mining became deeper and more extensive, widespread damage caused by rockbursts started to affect main infrastructure [44], and resulted in many fatalities and costly damage [35]. In the U.S., the first rockburst was reported at the Atlantic copper mine in Michigan in 1904 [6]. Rockbursts started to occur in the Coeur d'Alene Mining District in Northern Idaho since the 1920's [33]. By the late 1930's, rockbursts became a serious concern regarding the safety in this mining district [6].

Table 1-1 Rockbursts in Ontario mines, 1984-1986 [23].

Mining District	1984	1985	1986
Red Lake	26	5	10
Elliot Lake	59	88	22
Sudbury	16	31	56
Kirkland Lake	5	3	4
Total	106	127	92

In underground coal mining, rockbursts occurred mostly in Poland, Czech Republic, Germany, France, Slovenia, Russia, India, China, USA, Canada and Australia [7]. In China, many deep mines have experienced rockbursts. According to the available literature, the first rockburst event in China occurred in 1933 at Shengli Coal Mine in Fushun City, Liaoning province [46]. Since then, rockbursts have been reported at 102 coal mines that located in many major mining districts in China [39]. Among the reported rockburst events, approximately 83.6% occurred in coal mines. The coal mines with rockburst problems are mostly located in the east part of China [40].

In the US, the first bump event in coal mines in the U.S. occurred in 1936 based on the United States Bureau of Mines (USBM) coal bump database. However, several documents indicated that possible bump problems existed in coal mines predating 1936 USBM database [25]. The USBM database shows that bump related accidents had caused 78 fatalities between 1930 and 1995, as listed in Table 1-2. Among the 42 fatalities resulted from the rockbursts occurred between 1960 and 1995, 14 are in the Eastern U.S. and 28 are in the Western U.S. More recent statistics report that, from 1983 to 2007, at least 187 bump events occurred in coal mines in the United States. These bumps caused 229 injuries and 19 fatalities [33].

Table 1-2 Chronological distribution of rockburst events in the USBM coal bump database.

Time Period	Number of Bumps	Fatalities	Injuries
1930-1939	1	1	0
1940-1949	9	7	18
1950-1959	38	28	43
1960-1969	27	13	36
1970-1979	30	10	21
1980-1989	52	19	32
1990-1995	9	0	8

Coal bumps have been documented extensively in the United States since the 1920s [26]. A large loss of life from bumps occurred as recently as the 2007 Crandall Canyon disaster in which 9 miners and rescuers were killed, and 6 more were injured [20]. During a single bump event, over one-half mile of coal pillars failed within seconds. The sudden release of energy was observed as a 3.9 Richter magnitude event as over half of a million tons of coal were crushed in an instant (Fig.1.1) Factors known to contribute to bump events include deep cover [43,1], hard competent roof strata [36], retreat mining [42], and unfavorable stress concentrations from multiple seam [41] or longwall mining [16, 22]. The majority of these factors were found to contribute to the Crandall Canyon disaster with the exception being multiple seam mining. Computer models had been used in the design of the Crandall Canyon mine prior to the collapse; however these models were shown to overestimate the strength of the coal pillars in the mine and disregarded the potential for unstable failures [20]. Poor mine planning and faulty numerical analyses directly led to the disaster and highlighted why recommendations need to be made for assessing the threat of unstable failure within numerical models.

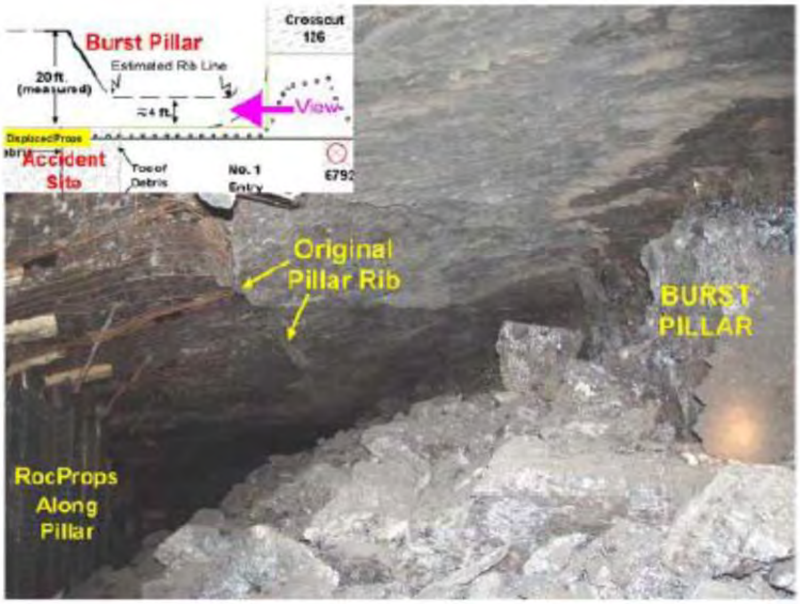

Fig. 1-1 Example of a fatal unstable failure at Crandall Canyon coal mine after massive bump event [20].

Coal bumps have represented a significant hazard to underground mining operations over the last century. Case histories have long described these events as the violent ejection of rock and debris into the working areas of the mine which causes damage to the mine or leads to the injury or death of workers. The magnitude of the damage caused by coal bumps ranges from small localized forms of unstable failure such as rib and face failures to the massive collapse of entire mine panels. The conditions necessary for coal bumps to occur are fairly well defined by early research in this area [13, 24, 48, 1], however eliminating their occurrence is difficult in practice due to the complexities of measuring and predicting the interactions between rockmass strength and brittleness, and the loading system stiffness which develops from in situ ground conditions and mining geometry. Additionally, information of the failure process of large rockmass structures is limited due to a lack of detailed knowledge of how these failures propagate as mining advances. The speed of failure and the substantial damage which results further restrict the amount of information that can be gained about the process of unstable failures in full scale mining scenarios. Numerical models may be applied to address many of these issues to develop a better understanding of the propagation of unstable failure across a range of mining environments and site specific conditions. These numerical tools hold significant value for assessing the potential for coal bumps and may lead to the design of safer layouts in bump prone conditions.

Many of the fundamental issues surrounding coal bumps have been described in studies of mining disasters and notable failures. The conditions which lead to unstable failure have been identified in these past cases and numerical models of coal bumps may be assessed from the lessons learned from these examples. The focus of our research is on the factors leading to coal bumps which are commonly found in western US coal mines. These factors include deep cover, pillar retreat mining, strong roof and floor strata, and failure along major discontinuities such as faults and bedding planes which rapidly redistribute stresses around the mine.

Significant bump event case histories exemplify these contributing factors for coal bumps with these examples representing ideal conditions for future numerical studies. The Springhill mine suffered from a series of catastrophic coal bumps from 1952 to 1958. The mine practiced retreat mining in strong roof and floor conditions and early researchers identified that failure of the surrounding strata led to the coal bump events [24, 11]. The failure of existing faults and discontinuities in the surrounding rockmass led to similar coal bumps at the Sunnyside mine until 1958. The bumps which resulted have been described in extensive detail by researchers of this era [11, 45, 47] and in more recent studies [54]. Longstanding problems specific to retreat mining were addressed due to a series of catastrophic failures at the Gary No. 2 and Gary No. 6 mines. Common design practices were established from these failures which dictated that regular pillar sizing and a uniform mining front reduce uneven stress concentrations and the potential for coal bumps [26].

Longwall mining has gained more favor as a safer approach for full extraction at depth, however repeated cases of floor heaves and bumps in gateroads has led to a major redesign of these layouts in some of the deep mines in Colorado and Utah. The Sunnyside mine experimented successfully using a single entry system [34], however common practice in the western coal mines has developed to rely on smaller sized yield pillars to reduce the potential for chain pillar bumps [17, 34]. More recently, barrier pillars have been implemented in some of the longwall mines in Utah to minimize stress interaction between longwall panels. The sizing of these pillars is still being explored and additional research is required for designing optimal longwall layouts.

Current methods of bump mitigation in US coal mines

Underground mining operations take significant steps to reduce the likelihood of damaging unstable failures, however eliminating their occurrence is difficult in practice due to the uncertainty of rock stresses, strains, strengths, stiffnesses, rockmass properties, and discontinuity characteristics. Current bump mitigation methods have mostly been derived empirically with little backing from the mechanistic understanding as derived from analytical and numerical modeling efforts. Retreat mines rely on empirically established pillar safety factors and pillar extraction sequences while yield pillar dimensions in deep longwall gate roads are determined from broadly based design criteria. In comparison to pillars, violent rib and longwall face failures seem to have received less attention from numerical modelers. Face bumps and sudden tailgate heaves are a major concern for some longwall mines in the west however the mechanisms involved in these failures are not fully understood. Bumps also affect tailgate corners in deep longwall mines and the effectiveness of separating longwalls by barrier pillars has been proposed and recently implemented in some of the deep mines as a counter measure to tailgate corner bumps. An improved mechanistic understanding of the barrier pillar layout performances using excess energy concepts may substantially contribute to the design of safer mine layouts in bump prone conditions at depth.

The state of the art in coal pillar design relies heavily on empirical pillar strength formulae such as the Mark-Bieniawski formula to calculate appropriate pillar sizing for a given overburden load. It is sufficient in most applications to rely on the ultimate strength of pillars to design a given mine layout, however in bump scenarios the post-peak response of a pillar plays an integral role in the design of a layout. Notable examples of post-peak pillar design include retreat mining and the use of yield pillars. Studies which focus on coal bumps demand that even greater attention be given to the post-peak behaviors of the rockmass and support structures in order to address the risks presented by potentially unstable, brittle rockmass systems. The underlying mechanisms of bump events have not been studied in sufficient detail by considering the post-peak response and loading stiffness of coal measure rocks. Gaining further insight into unstable failure mechanism and associated energy release magnitudes using advanced numerical modeling programs can significantly contribute to the current efforts of mitigating bump events in deep coal mines.

2. FAILURE STABILITY AND ITS MODELING

For a bump event to occur, two conditions have to be satisfied. First, the strength of the rock must be exceeded by the stresses induced by mining advances so that failure occurs. Second, the failure occurs in an “unstable” manner; that is part of the potential energy stored within rockmass is translated into kinetic energy through rapid expulsion of rock fragments from sidewalls. Gradual breaking up of surrounding rock with mining increments without a significant kinetic energy release is considered a “stable” failure. An additional qualifier for an unstable failure to be called a “bump” event is that the event should involve worker injury or production delay. This study focuses on the mechanisms of failure stabilities rather than the definition relating to the additional qualifier in the case of bumps.

The sketches in Fig. 2-1 illustrate the stable (left) and unstable failure (right) modes as considered in this study. The failure stability is defined by the post-peak response of a failing rock system and the displacement characteristics of the loading strata. The graphs in the illustration can be interpreted for either compressive or discontinuity shear loading cases. The line labeled “Stiff loading” represents a rockmass system whose stiffness is sufficiently high that an energy deficiency exists in the system and additional mining is required to continue to fail the brittle support rock or discontinuity. The “Soft loading” line demonstrates ground loading characteristics with an excess of potential energy which cannot be stored or absorbed through static processes in the post-peak regime. The shaded area under the soft loading line is proportional to the excess energy available to the system to fuel the dynamic motion of rock fragments.

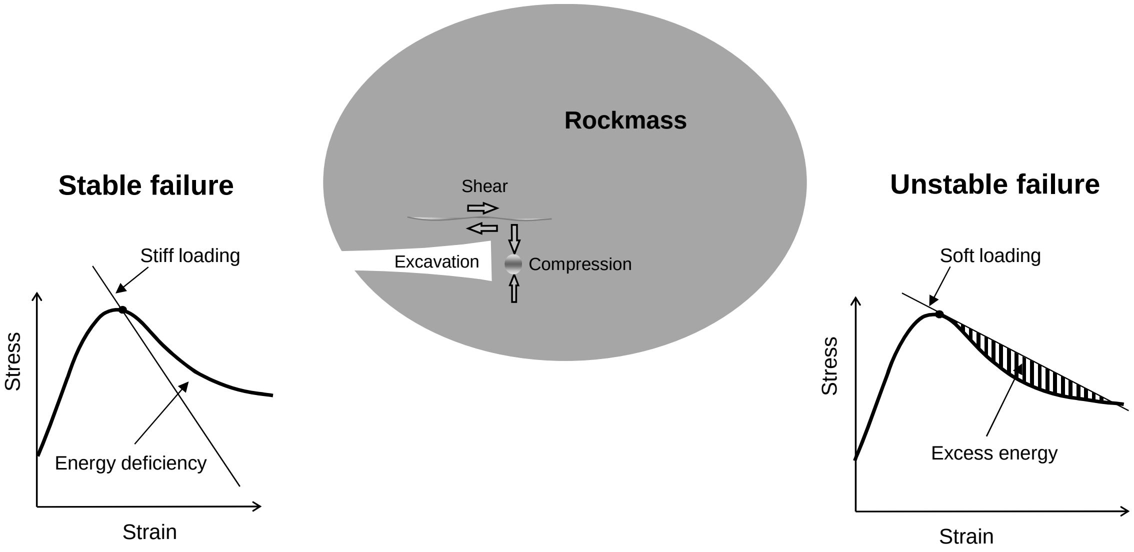

Fig. 2-1 Stable and unstable failures.

Large unstable failures in compression come in form of massive collapses or cascading pillar failures. Unstable failures in form of discontinuity slips may take place along large discontinuity planes such as bedding planes and faults and may cause significant damage to mine workings. More localized forms of unstable failures may affect smaller areas of a mine or isolated sections of a single pillar or sidewall. Regardless of these different expressions of unstable failures, the phenomenon at its fundamental level involves a sudden release of potential energy from rock which rapidly fails support rock and leads to an ejection of broken rock and debris into mine workings. Major focus of this project has been the identification of such unstable failures and their mechanisms in various idealized mine settings using numerical modeling. In relation to unstable failure event intensity, numerical modeling methodologies were also developed for determining the excess energy magnitudes for given mining conditions.

Validation of the selected numerical models' ability for modeling failure stability

As mentioned in the previous section, failure stability in this study is determined by the by the rock's post-peak behavior during compressive or shear loading. Unstable failures may also to occur when the confining stresses suddenly drop during face advances or top or bottom coaling. The commercial programs FLAC, UDEC, and PFC and their 3D versions, developed by Itasca [27, 28, 29, 30, 31, 32], were chosen for failure stability modeling since these incorporate the softening constitutive models for both compressive and discontinuity failure cases. The FLAC/3D simulations were used for the continuum modeling cases and applied to pillar and excavation face failures. UDEC and 3DEC codes were applied to the cases of failure stability modeling along large discontinuities such as bedding planes and faults. Since UDEC has the compressive softening capability, it was also used for modeling unstable failures resulting from deconfining effect of mining in high stress conditions. PFC simulations were used mostly for rockmass failing under compression and discontinuity failures at coal-rock contacts. Combined FLAC-PFC hybrid models were also used for modeling mining advances in situ conditions.

Prior to modeling of in situ mining scenarios, detailed investigations were carried out to confirm the applicability of the selected numerical codes to failure stability modeling. Each code was tested separately its applicability in assessing rockburst proneness. Evaluations of the codes in modeling failure stability were based on selected laboratory tests cases, such as uniaxial compressive strength (UCS) tests and direct shear test of discontinuity surfaces.

In this study, the failure stability criterion originally proposed by Cook [12] is adopted. Fig. 2-2 illustrates Cook's concept of the stable and unstable failure conditions that can occur during UCS testing of a rock specimen. The stress-strain curve shown with a solid line represents the specimen's characteristic behavior, which can only be obtained under stable loading conditions with a sufficiently stiff or servo-controlled loading machine [13]. Stability of loading in the post-peak region is not a given but is determined by the relative stiffnesses of the specimen's characteristic softening behavior and the testing machine. Stable failure occurs as long as the softening slope is shallower than the slope of the machine load line, as in the case of the dashed line, "Stiff Loading System" in Fig 2-2. If the machine load line is shallower than the softening slope, i.e. the case of "Soft Loading System" line in the same figure, the specimen cannot meet the machine's load demand in terms of the strain energy stored in the machine and unstable failure occurs [12]. The intensity of such failure is determined by the difference between the material post-peak stiffness and the stiffness of the loading system in other words, by the angle θ in Fig. 2-2

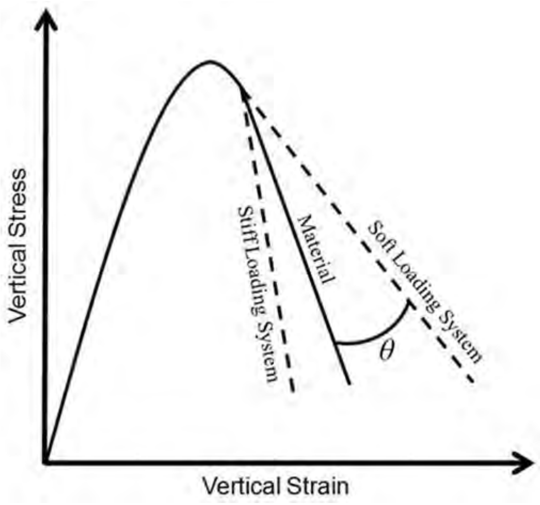

Fig. 2-2 Cook's stability theory of UCS testing [13].

Numerical modeling of UCS tests and the measurement methods were developed based on the failure stability concept described above. The model UCS specimen has material properties close to those of the coal seams being mined in the western United States. Assuming Mohr-Coulomb failure criterion, the strength of such coal is defined by a friction angle of 30°, and cohesion of 2.4 MPa. The specimen is cylindrical in shape with a diameter of 1 m and height of 2 m placed between a pair of 1 m high 1 m diameter steel platens as shown in Fig. 2-3). The load is introduced by applying constant axial displacement at the ends of the platens in a configuration shown in the figure. The idealized complete characteristic stress-strain curve of the model specimen exhibits strain-softening behavior similar to shown in Fig.2-3 (right). The interface at the steel–specimen contact is assigned a friction angle of 15°. The effect of loading system stiffness is then controlled by adjusting Young's modulus of the platens. The symbols E and E_{pp} refer to pre and post-peak moduli of the specimen.

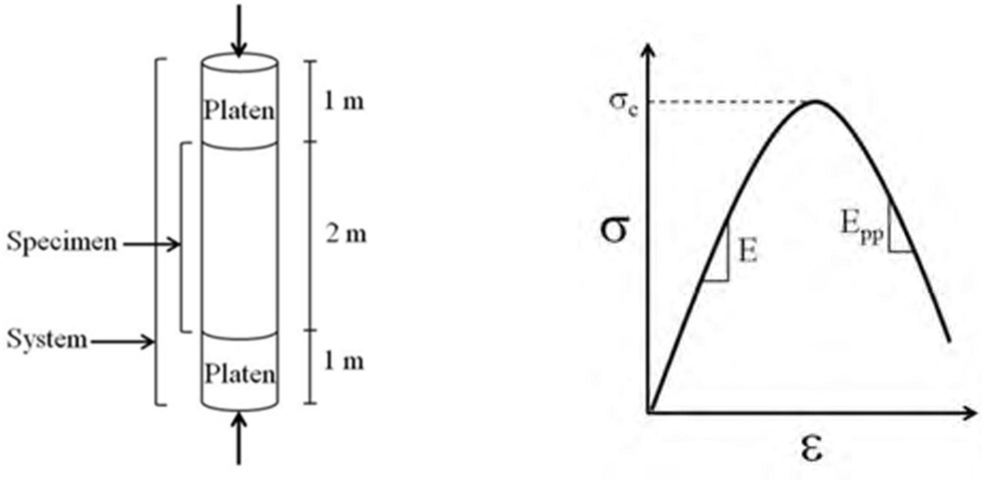

Fig. 2-3a Test model (left) and its idealized material behavior (right).

The results of the numerical modeling studies are presented in form of stress-strain plots based on the descriptions given in Fig. 2.3b. The solid line represents the characteristic response of the rock specimen when the specimen fails in a stable manner. The dashed lines represent the case of unstable failure. During unstable failure, strain measurements taken between the ends of the specimen (along L_{spec}) trace the elastic rebound of the platens. The measurements taken between the platen ends (along L_{sys}) plot the unstable failure as sudden, complete loss of load. The space between the peaks of the stable and unstable curves denotes the additional strain in the soft platens that rebound elastically at failure. The difference between the two stress-strain curves in the case of L_{sys} plots is due to the composite stiffness of the platen and specimen system.

The model compressive strength tests were performed using three numerical models; FLAC3D, 3DEC, and PFC3D. For each model, the tests were repeated for three different platen modulus values of 100 GPa, 10 GPa, and 1.5 GPa.

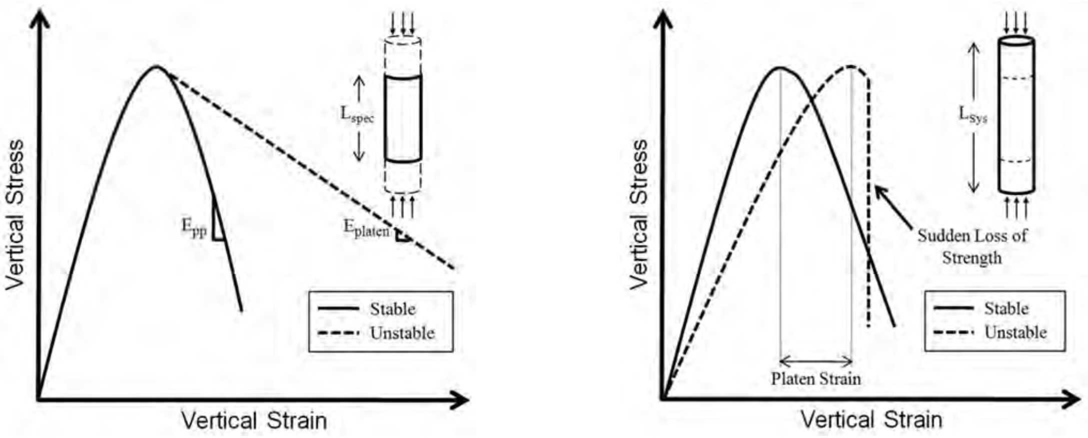

Fig. 2-3b Stress-strain response measured on specimen (left) and on platen ends (right).

Material calibration

A calibration process, unique to each numerical model type, was applied in order to generate a specimen with material properties approximating the material characteristics listed as "Target" values in Table 2-1. For the calibration process, the model specimen was loaded by applying constant axial displacement directly at its top and bottom surfaces. To ensure failures taking place in a stable manner during calibration modeling, platens of near rigid stiffness, 400 GPa, were used for the FLAC3D and 3DEC tests while rigid walls were used in the PFC calibration. Table 2-1 shows also the characteristic values of the modeled specimens as obtained from the three numerical models. The post-peak modulus for the models was determined as the slope of the line drawn between points on the specimen stress-strain curve at stress values found at 90% and 50% of peak stress during failure. For all models, elastic modulus and Poisson's ratio are both calculated using the origin and the point on the loading portion of the curve at 50% UCS.

Table 2-1 The material properties calibrated for the UCS validation test modeling

	Target	FLAC3D	3DEC	PFC3D
UCS (MPa)	7.6	7.5	7.6	7.5
E (GPa)	4.0	4.0	4.0	4.2
Epp (GPa)	-4.0	-4.0	-4.1	-5.75
ν	0.2	0.2	0.2	0.2

UCS modeling results

The UCS model test results in terms of stress-strain curves are shown in Fig. 2-4. As seen, the results somewhat differ from the target material for each of the numerical modeling method employed. The hardening response of the material closer to peak is more pronounced in FLAC3D and 3DEC models compared to PFC3D model. Also, fluctuations in the post-peak region show dissimilarities and indicate potential difficulties in obtaining the target value for E_{pp}. For the purpose of calibration studies, the use of E_{pp} is generalized in the sense that its average trend is compared to the platen stiffness in concluding whether the failure is stable or unstable.

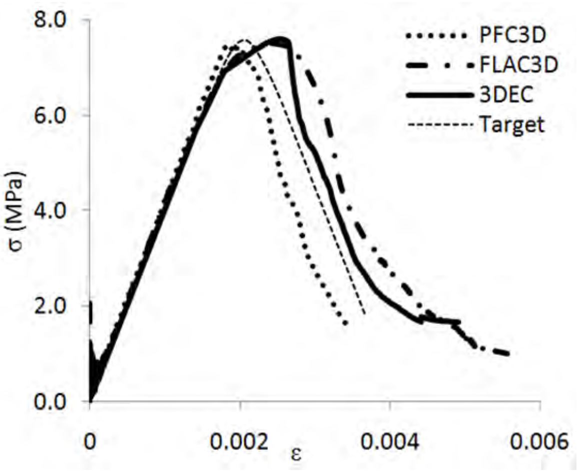

Fig. 2-4 UCS model specimen generated stress-strain curves.

FLAC3D models

A three-dimensional coal and platen UCS model was constructed in FLAC3D as is shown in Fig. 2-5. The platens were modeled elastically and the coal was represented using the strain-softening constitutive model. Interface contact behavior of friction angle 15^{o} is assigned between the coal and platens to simulate confinement effects at the top and bottom of the coal sample. Also shown in Fig. 2-5 is the calibrated strain-softening material property for the coal specimen. Within the strain-softening model, parameters for cohesion, friction angle and dilation angle in the coal specimen are adjusted as the specimen plastic strain achieves pre-defined values. For example, as shown in the table in Fig. 2-6, the third row in the “Cohesion” means that when the specimen plastic strain within a zone is 0.0090, the cohesion will be changed to 0.50 MPa for that zone. The calibrated set of parameters resulted in a sample material response which approximately represents the material properties listed in Table 2-1.

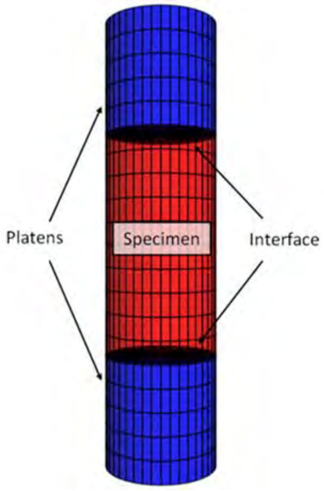

Cohesion (plastic strain, MPa)	0.0000,2.41 0.0005,2.41 0.0090,0.50 0.0155,0.26 0.0160, 0.26
Friction Angle (plastic strain, degree)	0.0000,0.10 0.0001,25.0 0.0010,30.0 0.0100,30.0
Dilation Angle (plastic strain, degree)	0.0000,0.00 0.0010,15.0 0.0070,15.0 0.0120,5.00

Fig. 2-5 FLAC3D test specimen and strain-softening parameters.

According to Fig. 2-3, the strength of the specimen should be lost suddenly due to platen rebound while no added system displacements would be required to fail the specimen. The system stress-strain response would therefore appear as a vertical drop in stress. This expected system response was confirmed in FLAC3D for the system loaded under unstable 1.5 GPa platen conditions as shown in Fig. 2-6. The response of the specimen appears as a linear response identical to the platen elastic modulus during unstable unloading or rebound. This behavior is confirmed in the specimen plot for the 1.5 GPa platen on the right in Fig. 2-6, where the specimen plot assumes an acute stress drop compared to plots of stable tests of 10 and 100 GPa platens.

A subtle result emerges when upon further study of the stress-strain curve of the system during failure in the case of semi-stable 10 GPa platens. The system curve represented by the dashed line in Fig. 2-6 (left) assumes a very steep slope of -147 GPa_at one point during the test of the semi-stiff platens. As shown in Fig. 2-7 (left), this behavior occurs only for a portion of the test but is an indication of unstable failure. In order to more closely study the system’s response when using 10 GPa platens, a modified loading procedure was applied to the system that included frequent pauses in the test as the specimen was failing. During each pause, the velocity boundary at the top and bottom of the platens was set to zero and the system was allowed to come to equilibrium. Under stable loading conditions, the system would quickly come to equilibrium after each pause. For unstable loading conditions where the stiffness of the platens was less than the stiffness of the coal, the specimen would continue to fail due to platen rebound even if the total system strain increment was paused. Fig. 2-7 (right) shows the specimen stress history during the 10 GPa platen test when using the modified testing procedure. The platens were paused after every 0.1 MPa drop in sample strength. As seen in the figure, a sudden drop in strength occurs in the specimen during a pause step at 5.3 MPa. The specimen continues to fail unstably until it reaches a residual strength of 4.4 MPa. At this point the system regains static equilibrium and no additional indications of instability are observed in the remainder of the test.

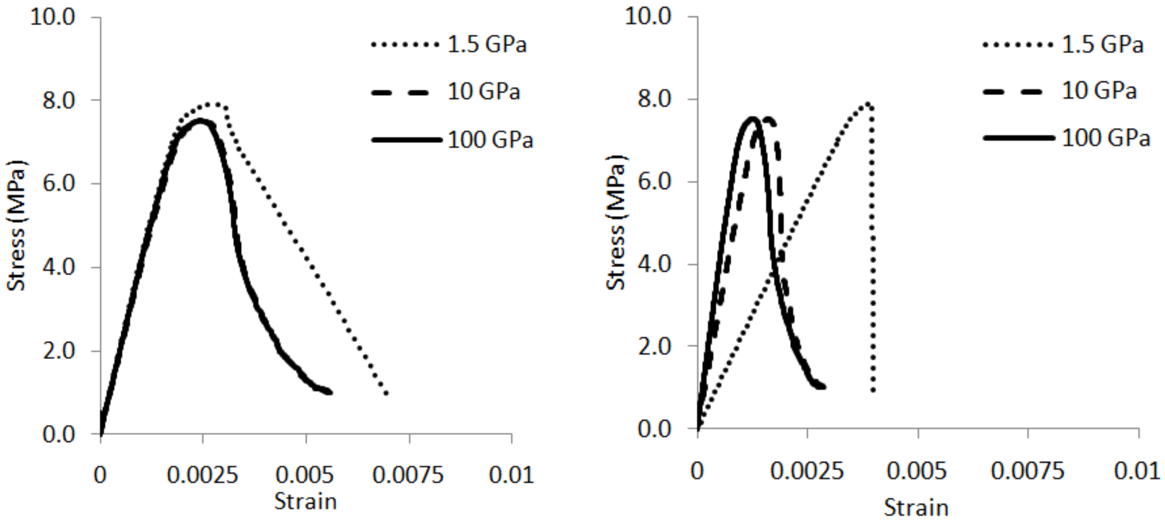

Fig. 2-6 FLAC3D stress-strain responses to UCS tests measured on the platen specimen contacts (left) and on the outer ends of platen (right).

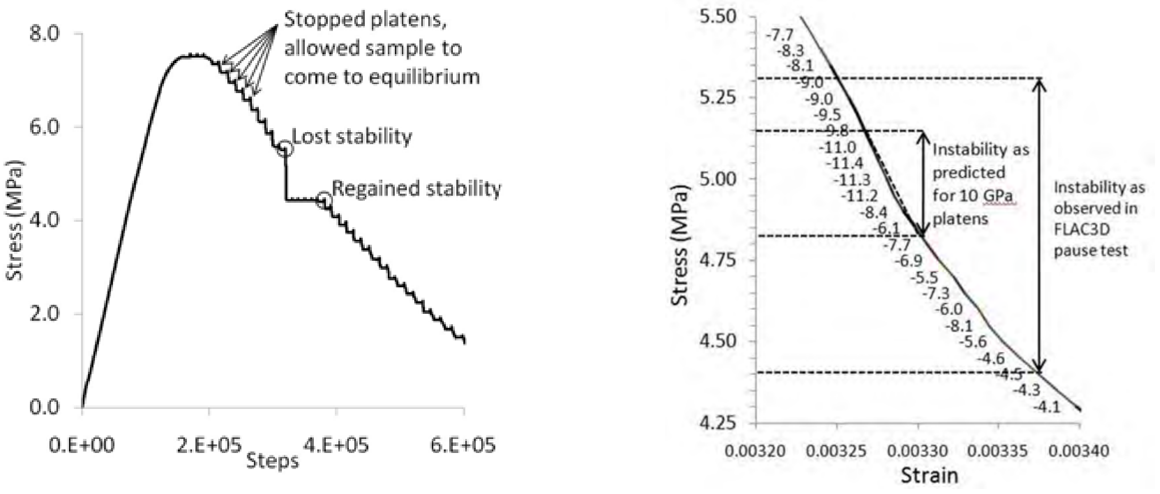

Fig. 2-7 Specimen stress vs. time step (left) and vs. strain plots obtained using modified testing procedure with pauses during failure (right).

3DEC Tests

The 3DEC UCS model geometry is shown on the left in Fig. 2-8. The model consists of two joint sets embedded in the specimen. The spacing is 0.4 m between horizontal joints, and 0.1 m between vertical joints. The joints are assigned as Coulomb slip model with the parameters listed in the table in Fig. 2-8. These joints intended to represent the face and butt cleats encountered in coal seam material. The blocks created by the joint sets are further discretized into zones of strain-softening material, while the platens are discretized into zones of elastic material with the properties of steel. The average length of the zone edge is 0.1 m and 0.2 m for the specimen and platens, respectively. The loading is induced by applying constant velocity of 7.5×10^{-3} m/s at both the top and bottom of the steel platens.

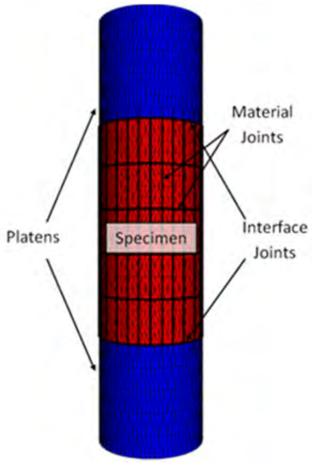

Parameter (Unit)	Value
Cohesion (MPa)	1.0
Friction Angle (Degree)	30.0
Dilation Angle (Degree)	15.0
Tensile Strength (MPa)	0.0
Normal Stiffness (GPa/m)	50.0
Shear Stiffness (GPa/m)	100.0

Fig. 2-8 3DEC model geometry with joint orientation (left) and material parameters (right).

The strain-softening parameters assigned to the zones of the specimen in the models are listed in Table 2-2. The specimen was calibrated to have similar properties as "Target" values listed in Table 2-1. The characteristic material stress-strain curve after calibration in 3DEC is shown in Fig. 2-9.

Table 2-2 3DEC strain-softening parameters.

Cohesion (plastic strain, MPa)	0.0000,2.15 0.0005,2.15 0.0272,0.12
Friction Angle (plastic strain, deg.)	0.0000,15.0 0.0001,25.0 0.0010,30.0 0.0070,30.0
Dilation Angle (plastic strain, deg.)	0.0000,0.0 0.0010,15.0 0.0070,15.0 0.0120, 5.0

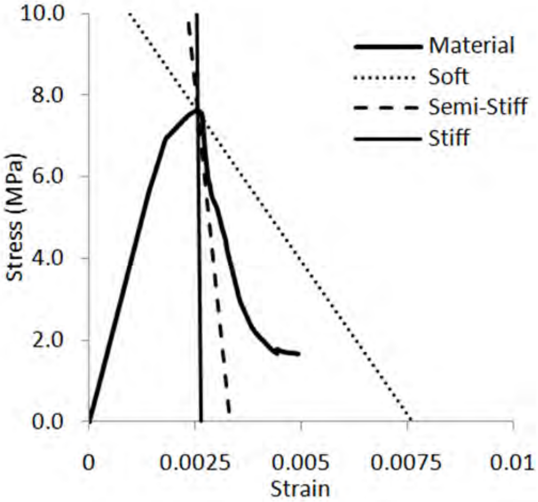

Fig. 2-9 Material response of 3DEC sample.

The specimen stress-strain curves for different platen stiffness loading are shown in Fig. 2-11. The results are similar to those obtained from the FLAC3D modeling. For the stiff and semi-stiff loading systems (100 GPa and 10 GPa), the post-peak behavior is similar to the material characteristic behavior, indicating that specimen failure took place mostly in a stable manner. For the soft loading system, the post-peak modulus approximates that of the steel platen modulus of 1.5 GPa, implying a rapid platen rebound during unstable failure as discussed in the previous sections of the FLAC3D tests. The residual strength in the graph is thought to be due partly to the residual strength assigned in the strain softening model and also to block interlocking occurring within the specimen.

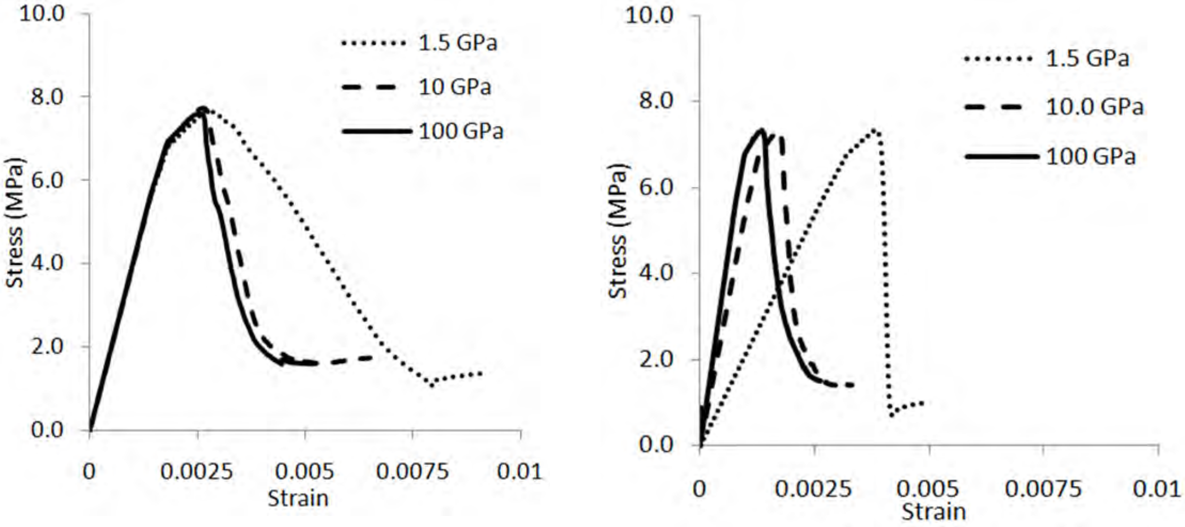

Fig. 2-10 3DEC stress-strain responses to UCS tests measured on the platen specimen contacts (left) and on the outer ends of platen (right).

The post-peak moduli of the specimen stress-strain curves for each test are shown in Table 2-3. In general the values in the table are in accord with the previously described stable/unstable failure conditions. Values in the darker shaded region list expected and measured specimen post-peak moduli for the unstable failure, and values in the lighter shaded region list expected and measured specimen post-peak moduli for the stable failure. For the unstable failure, the measured specimen post-peak modulus matches the platen modulus and for the stable failure the measured specimen post-peak modulus matches the characteristic material post-peak modulus.

Table 2-3 3DEC test post-peak moduli.

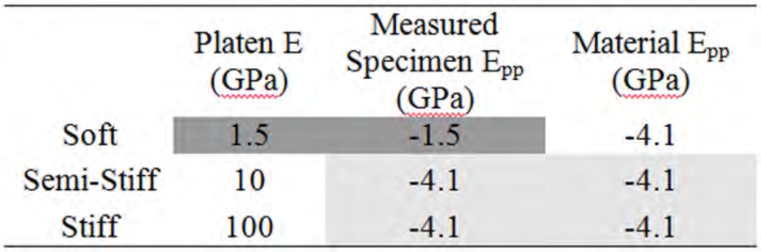

	Platen E (GPa)	Measured Specimen E_{pp} (GPa)	Material E_{pp} (GPa)
Soft	1.5	-1.5	-4.1
Semi-Stiff	10	-4.1	-4.1
Stiff	100	-4.1	-4.1

PFC3D tests

The PFC3D UCS model specimen consists of an assemblage of discrete spherical particles that are bonded together between two steel platens as shown in Fig. 2-11. Also shown in this figure is the micro parameters that are used to generate an in-situ coal specimen similar to the material described in Table 2-1. The micro-parameters shown in Fig. 2-11 were established using a specifically developed iterative calibration procedure.

The values of the parameters used in modeling are given in the table in Fig. 2-11. The specimen is comprised of particles with density, ρ, and a uniform particle size distribution determined by the ratio of minimum particle diameter, D_{min}, and maximum particle diameter, D_{max}, where D_{min} = 23 mm. The friction coefficient between the balls is denoted by μ. Stiffness of the particles and bonds is assigned by providing Young's modulus, E_c for balls and E_b for bonds, and the ratio of normal to shear stiffness, k_n/k_s and k_{nb}/k_{sb}. Other necessary bond properties include bond normal strength, σ_b, and bond shear strength, τ_b. The bond radius multiplier, λ, controls the diameter of the bond in reference to the smaller of the two bonded particles. Smaller bond radii result in higher bond stresses for the same displacement in shear or tension.

The model specimen is placed between a pair of infinitely strong elastic steel platens, also constructed from balls and bonds, having a specific elastic modulus and Poisson's ratio. The interface between the platens and the specimen is bonded with bonds of equal strength to those within the specimen. Three different tests were conducted by keeping the characteristic material same and varying the elastic modulus of the platens. Each test is loaded with a sufficiently slow strain rate to achieve a quasi-static loading condition. The 10 GPa and 100 GPa tests were run at a strain rate of 5% strain/second. To achieve a realistic platen rebound during unstable specimen failure, the 1.5 GPa test had to be run at 0.05% strain/second.

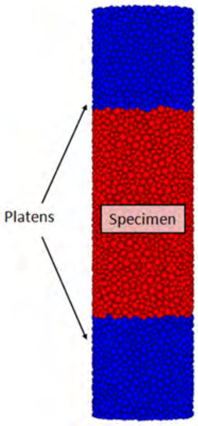

Particles	Bonds
$\rho = 1313$ kg/m^3	$\lambda = 1.0$
$(D_{max}/D_{min}) = 1.94$	$E_b = 4.48$ GPa
$E_c = 3.14$ GPa	$k_{nb}/k_{sb} = 1.62$
$k_n/k_s = 1.84$	$\sigma_b = 6.67 \pm 0.1$ MPa
$\mu = 0.49$	$\tau_b = 7.15 \pm 0.1$ Mpa

Fig. 2-11 PFC model geometry (left) and micro-material parameters (right).

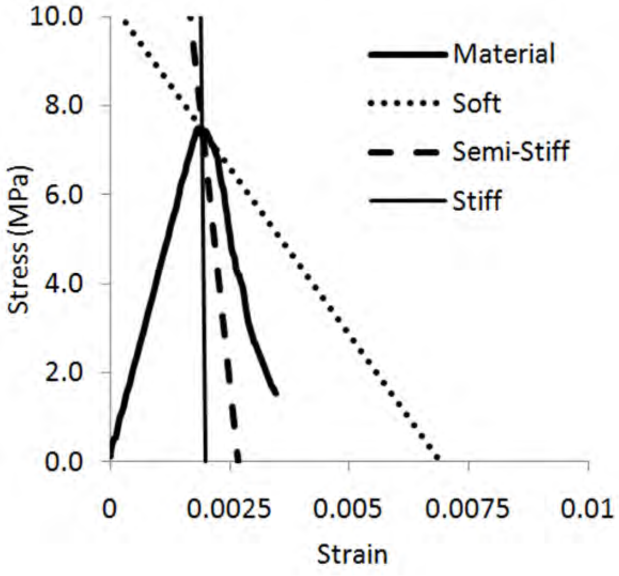

Fig. 2-12 Material response of PFC3D sample.

Fig. 2-13 shows the specimen and system stress-strain responses to loading. As in the case of FLAC3D and 3DEC, the plots show unstable failure for the soft (1.5 GPa) and stable failure for the stiff (100 GPa and 10 GPa) platens, where the specimen post-peak response follows platen rebound in the former and material characteristic curve in the latter.

Table 2-4 lists the post-peak modulus values obtained from the PFC3D model tests. These values are in agreement with the theory of unstable failure. Also, it conforms to the postulations set up in Fig. 2-3 that the specimen post-peak modulus should be similar to the platen modulus during unstable failure. In the stiff loading case, the specimen post-peak modulus is approximately the same as material pos-peak modulus.

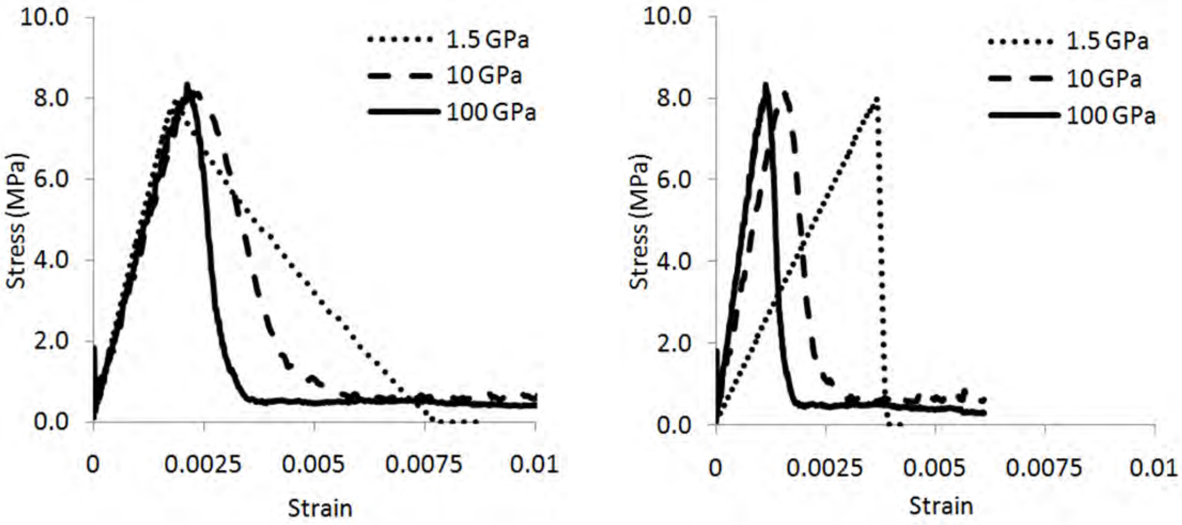

Fig. 2-13 PFC3D stress-strain responses to UCS tests measured on the platen specimen contacts (left) and on the outer ends of platen (right).

Table 2-4. PFC3D test post-peak moduli.

	Platen E (GPa)	Measured Specimen E_{pp} (GPa)	Specimen E_{pp} (GPa)
Soft	1.5	-1.35	-5.74
Semi-Stiff	10	-4.4	-5.74
Stiff	100	-10	-5.74

3. STUDIES OF FAILURE STABILITY MECHANISMS

Following the validation of the candidate numerical codes in modeling failure stability, this section focuses on establishing numerical modeling methodologies and parameters that can identify unstable failures when the stresses exceed rock strength around mining excavations. For failures in compression, FLAC/3D and PFC/3D are used. For failures along large discontinuities, the distinct element code UDEC is used.

FLAC3D analysis of compressive failure stability

In this series, the coal seam is taken as continuum material represented by the Mohr-Coulomb Strain Softening (MCSS) model. The material does not contain any major discontinuity planes that can be activated under shear loads or exhibit any anisotropic response. The in situ strength reduction due to small natural defects, such as small joints and fractures, are indirectly accounted for by adjusting coal’s intact strength and post-peak behavior.

Instability identifiers in UCS models

For the FLAC3D UCS tests, the values of the selected potential instability identifiers at the grid points and zones of the coal specimen are recorded. The grid point identifiers consisted of unbalanced force, acceleration, and velocity. The zone-level identifiers were shear strain rate and plastic shear strain rate. The maximum value of each identifier was recorded for all grid points and zones within the coal specimen.

A cylindrical coal specimen sized 1 m in diameter and 2 m in height was tested between two elastic platens each measuring 1 m in height. The combined system of platens and specimen is shown in Fig. 3-1.

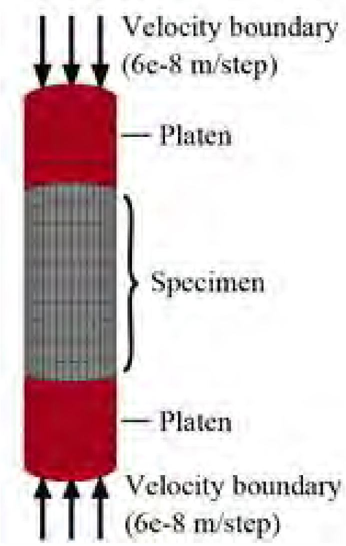

Fig. 3-1 Uniaxial compressive strength test configuration in FLAC3D model.

The elastic modulus of the platens was controlled between tests and spanned the range of 2 to 100 GPa. The mesh grid points were spaced at 0.2 m intervals in the vertical and the outward radial directions. A calibration procedure had been employed for the given zone sizes to achieve compressive strength behaviors approximate to those of coal. The specimen was calibrated to exhibit a peak strength of 7.9 MPa and a Young's modulus of 4.1 GPa. The specimen assumed a brittle failure response with a maximum post-peak drop of approximately 20 GPa.

A velocity boundary with a small rate of 6e-8 m/step was applied at the end of the platens to apply an increasing load onto the system until a specimen strain of 0.003 was achieved. At this point, the simulation was run for an additional 1000 steps and the system was allowed to come to static equilibrium.

The model was run in static solution mode with masses scaled artificially at the gridpoints. The ideal method for analyzing dynamic failure would be through a truly dynamic analysis, however uncertainties in the calibration of such a model and the length of time required to compute a dynamic solution made the static mode a more favorable option. The drawback of the static solution mode is that any measurements that are dependent on a time response hold little physical significance. Insight may still be gained by comparing a known stable failure case against an unknown, potentially unstable failure case. In this manner a measure of relative instability may be established.

A series of identical uniaxial compressive strength tests were run in which the coal specimen was represented using a plastic Mohr-Coulomb (MC) constitutive model. These tests provided insight into how loading system stiffness may directly affect the selected identifiers within the finite difference model. The specimen was calibrated to undergo plastic flow at a comparable stress value as the peak strength of the Mohr-Coulomb strain-softening (MCSS) model. The stable stress-strain response for the MCSS model is shown in Fig. 3-2 along with the Mohr-Coulomb (MC) plastic model response as a comparison.

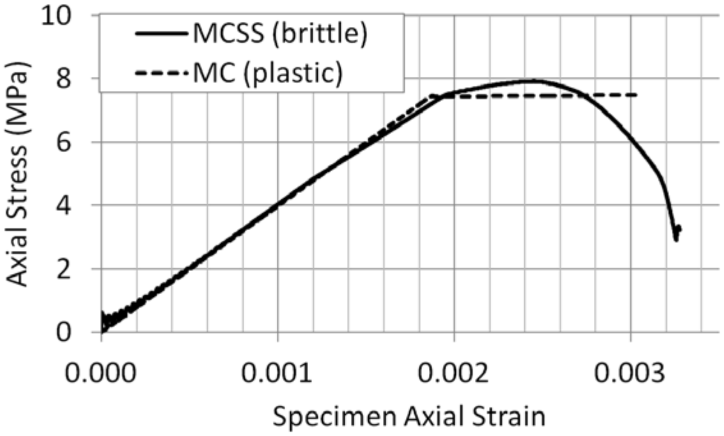

Fig. 3-2 Specimen stress-strain response of Mohr-Coulomb Strain-Hardening/-Softening (MCSS) and Mohr-Coulomb (MC) models.

Indicators of Unstable Failures

Axial stresses were calculated during the test from the sum of the applied boundary forces divided by the cross-sectional area of the specimen. Strains were then recorded from the displacements at the specimen-platen contacts. The stress-strain responses of the specimens were calculated from these values and their post-peak responses were recorded. For the platens with an elastic moduli ranging from approximately 16 to 100 GPa, the post-peak stress-strain response of the specimen was consistent between UCS tests. However, for lower elastic platen moduli, unstable failure conditions were initiated and the specimen assumed a post-peak response identical to that of the elastic behavior of the loading system. This is demonstrated for the stable 40 GPa and unstable 2 GPa loading cases shown in Fig. 3-3. The specimen in the unstable failure case assumed a -2 GPa post-peak stress-strain response which was identical to the elastic modulus of the loading system. For the platen Young’s moduli lower than 16 GPa, the unstable loading conditions were coupled with a dramatic increase in the maximum unbalanced force acting within the model. The second plot of Fig. 3-3 compares the response of the maximum unbalanced force between the unstable and stable loading conditions.

Low platen stiffnesses such as the 2 GPa case elicited an unstable failure response in the specimen as indicated by the stress-strain response and by the maximum unbalanced force in the specimen. These unbalanced forces were carried through the model to additionally cause large accelerations, velocities, and shear strain rates during unstable failure conditions.

Identifier values were recorded only after the vertical specimen strain reached 0.001 in order to isolate the identifiers associated exclusively with the failure of the specimen. The unbalanced forces were large for high platen stiffnesses during initial loading, as can be seen in Fig. 3-3.

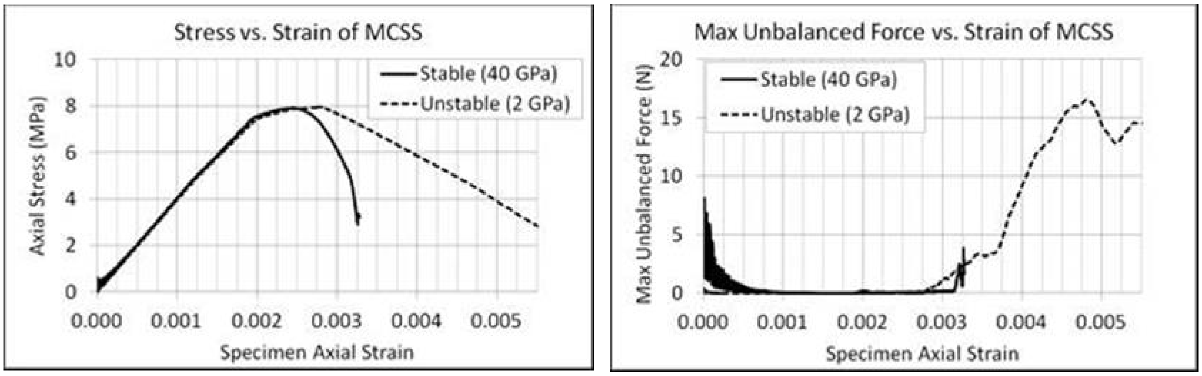

Fig. 3-3 Stress vs. strain of Mohr-Coulomb strain-softening specimen during stable (40 GPa platens) and unstable (2 GPa platens) failures with corresponding histories of maximum unbalanced forces.

The maximum values for the previously selected indicators were compared between the Mohr Coulomb plastic (MC) and the MCSS test cases to attempt to further isolate the unstable failure phenomenon from dynamic effects caused exclusively by changes to the loading system stiffness. The results from these tests are shown in semi-log plots in Figs. 3-4 through 3-7.

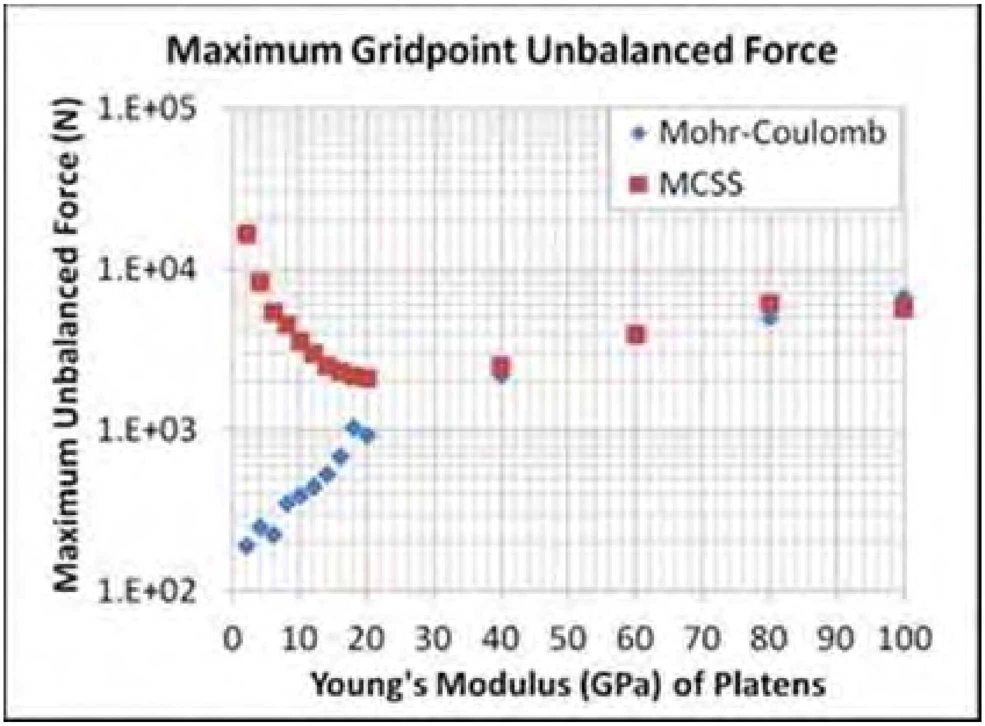

Fig. 3-4 Maximum gridpoint unbalanced force within specimen over a range of platen stiffnesses for both plastic Mohr-Coulomb and brittle Mohr-Coulomb strain-softening models.

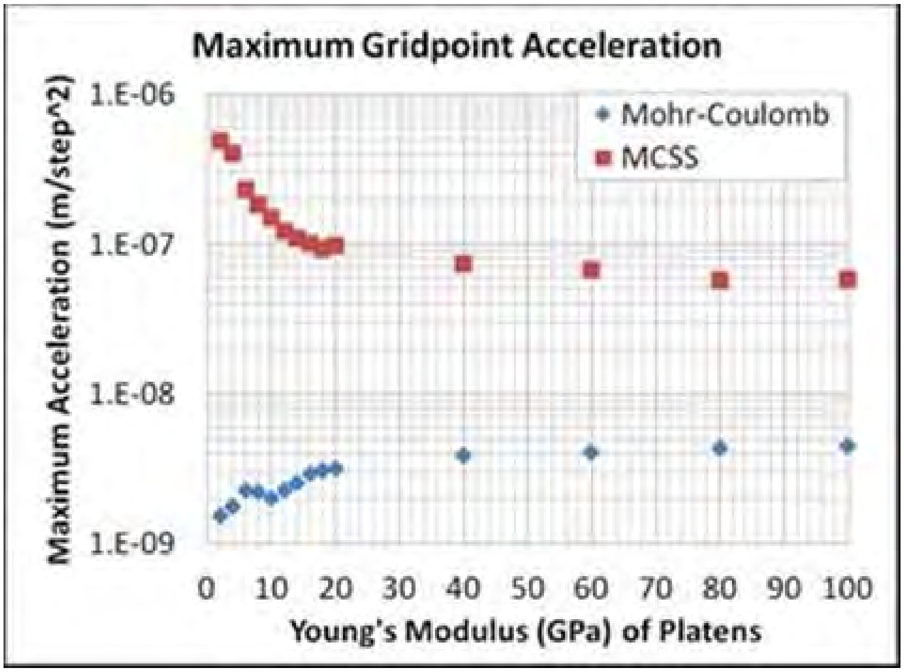

Fig. 3-5 Maximum gridpoint accelerations within specimen over range of platen stiffnesses for plastic Mohr-Coulomb and brittle Mohr-Coulomb strain-softening models.

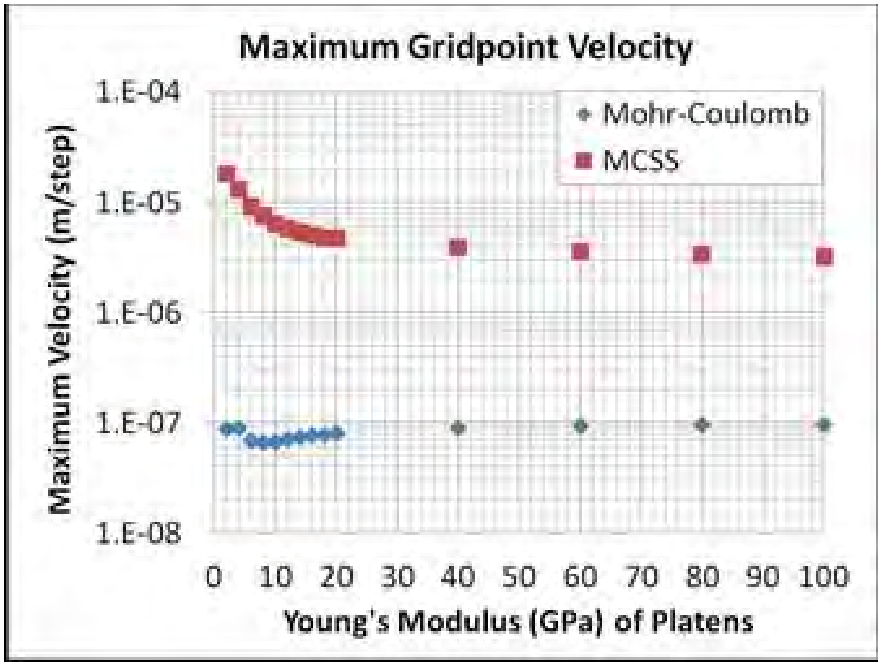

Fig. 3-6 Maximum gridpoint velocity within specimen over range of platen stiffnesses for plastic Mohr-Coulomb and brittle Mohr-Coulomb strain-softening models.

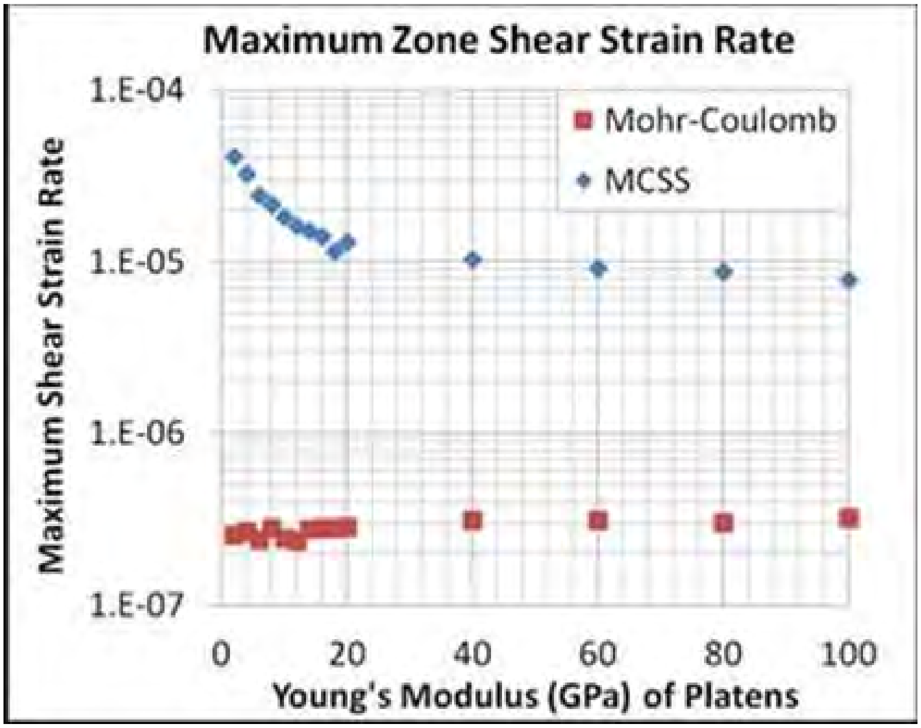

Fig. 3-7 Maximum zone shear strain rate within specimen over range of platen stiffnesses for plastic Mohr-Coulomb and brittle Mohr-Coulomb strain-softening models.

Note that the behavior of the indicators diverge between the MCSS and the MC cases with platen stiffnesses less than approximately 16 GPa. This change in behavior corresponded well with other measures of unstable failure and the previously assumed initiation of unstable failure for platens softer than the steepest portion of the specimen's stress strain response, which was approximately -20 GPa. By using the selected identifiers of instability, it was possible to directly distinguish between stable and unstable failures in the quasi-static model.

Triaxial compressive strength tests

Further tests were conducted to determine the adequacy of using the selected unstable failure identifiers in FLAC3D under confined loading conditions. The confined tests were conducted on the previously calibrated brittle coal specimen. Confining pressures of 1 MPa to 6 MPa were applied to the specimen. It was found that the specimen assumed a friction angle of 30° and cohesion of 2.3 MPa during these confined tests. Stable failures were induced using stiff 100 GPa platens and unstable failures were induced using soft 2 GPa platens. The stress-strain results of the confined tests are shown in Fig. 3-8 with stable and unstable results marked accordingly.

The specimen was found to assume a brittle yet strengthening stress-strain behavior for increasing levels of confinement when a stiff, stable loading system of 100 GPa platens was applied to fail the specimen. The post-peak slope assumed the stiffness of the soft 2 GPa platens for the unstable failure cases.

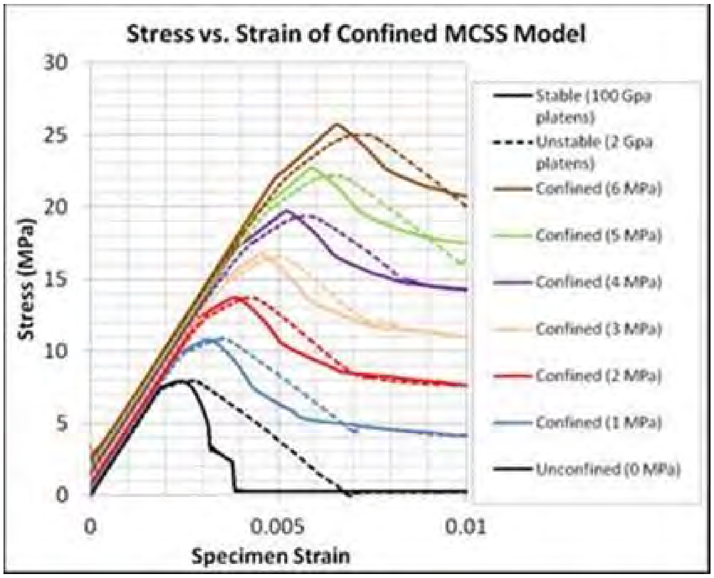

Fig. 3-8 Stress-strain responses of triaxially confined brittle coal specimens undergoing failure under unstable (2 GPa) and stable (100 GPa) platen loading conditions.

Identifying unstable failures in confined specimen

Numerical identifiers were applied to determine the location, duration, and magnitude of unstable failure during the confined tests. The maximum unbalanced force recorded during the test was compared between a stable and unstable test case under 3 MPa of confinement. The results from this trial are shown in Fig. 3-9.

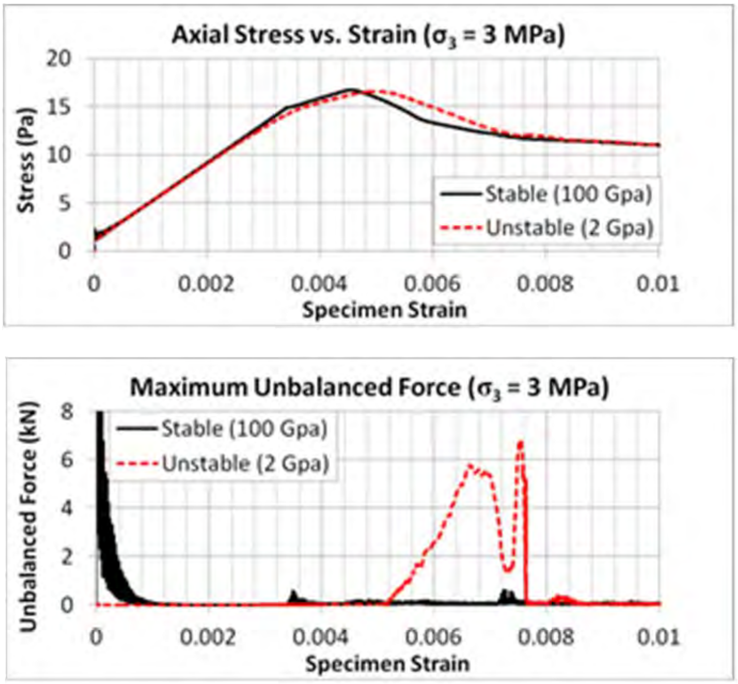

Fig. 3-9 Maximum unbalanced forces determined from 3 MPa confinement tests.

The time history of the maximum unbalanced force shows large unbalanced forces as the specimen lost stability during the unstable 2 GPa platen loading case. Large unbalanced forces were not observed past initial loading during the stable failure using 100 GPa platens.

The indicators of unstable failure which were previously proposed were extended to the triaxial compressive strength tests. The results for the maximum indicator values within the specimen were recorded for each test and are shown in Fig. 3-10. The maximum unbalanced force and acceleration were not calculated for the gridpoints located on the perimeter of the specimen during these confined tests due to numerical effects from the applied pressure boundary at these points. The velocity measurements were unaffected by the applied boundary and included a record of gridpoints at the perimeter of the specimen during the confined tests. The Mohr-Coulomb results from these trials have been included to provide a reference for how a fully stable, plastic model responded to changing platen stiffnesses and confinements as compared to the brittle Mohr-Coulomb strain-softening model which underwent unstable failure when the soft 2 GPa platens were used.

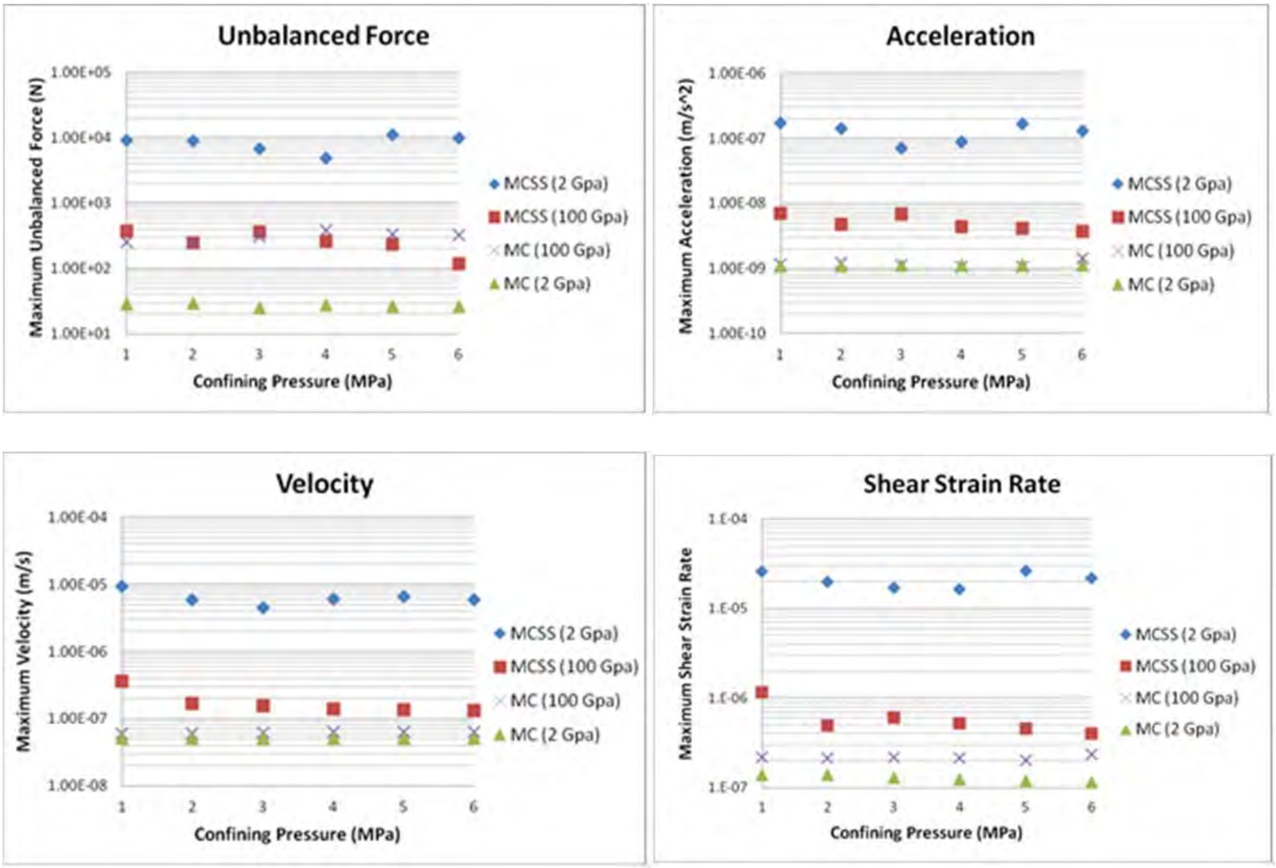

Fig. 3-10 Maximum zone shear strain rate within specimen over range of platen stiffnesses for perfectly plastic Mohr-Coulomb and brittle Mohr-Coulomb strain-softening models.

The maximum values for the indicators of unstable failure show clear distinction in the magnitudes between stable and unstable test cases. Large unbalanced forces were observed at all levels of confinement for the soft loading condition as compared to the stiff, stable case at the same level of confinement. Large unbalanced forces then led to increased accelerations, velocities, and shear strain rates in the model. The effect of physical instability in the specimen could be separated from direct changes to the loading system stiffness by comparing the MCSS results to the MC results, which actually showed the opposite trend for dynamic effects in that the magnitudes of the indicators were higher for the stiffer 100 GPa platen case than the softer 2 GPa platen case.

The results of these tests show good agreement with the uniaxial compressive strength tests. The selected identifiers of unstable failure all showed a trend of significantly increasing in magnitude during unstable failure.

Excess energy and Energy balance

During unstable failure, more potential energy is released from a rock system than is stored as strain energy and is consumed through plastic deformation. The resulting excess energy is not accounted for statically and is instead converted into kinetic energy through the dynamic motion of rock within the system. The total kinetic energy released by an unstable failure may thereby be determined from the excess energy of the otherwise static system. This concept is demonstrated for a simple uniaxial compressive strength test shown in Fig. 3-11 where a stiff loading system elicits a stable failure while a soft loading system provides excess energy which is then converted into kinetic energy as the brittle specimen is caused to fail in an unstable manner.

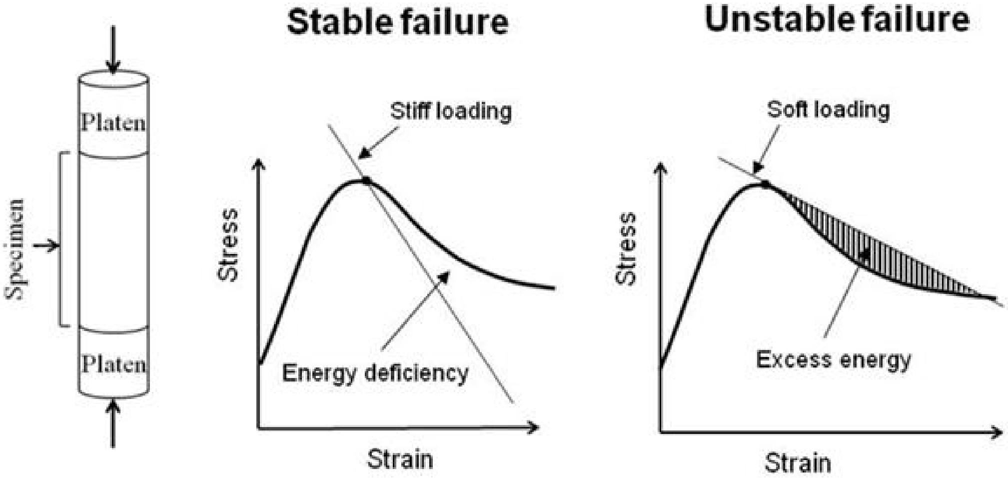

Fig. 3-11 Idealized representation of unstable failure and excess energy in UCS test case.

This concept of excess energy can be extended to the more complex loading conditions found in underground mines by calculating the static contributions of energy for a continuum numerical method. The calculation of excess energy, E_e, is given by the formula

$$E_e = (W_b+W_g) - (U+W_r)$$

where W_b is the total boundary work applied to the system, W_g is the contribution of gravitational potential energy, U is the elastic strain energy stored in the rock, and W_r is the work performed through plastic deformations of the rock [50]. This energy balance formula was implemented in FLAC3D to determine the total excess energy released during simulated unstable failures.

A FISH routine was written within FLAC3D to calculate boundary work and changes in gravitational potential energy. The built-in energy tracking module in FLAC3D was then used to calculate the elastic strain energy and work performed by plastic deformations in the model [30].

Fig. 3-12 shows the stress-strain results of stable and unstable failures of FLAC3D simulated laboratory triaxial compressive strength tests. Each confinement test was repeated using both stiff and soft loading platens to produce stable and unstable failures, respectively. When the failure is unstable, the specimen stress response follows the elastic rebound of the testing machine as represented by the dashed lines in the plot. As mentioned before, if the failure is stable, the specimen compression follows the characteristic peak-peak behavior of the specimen. The area between the dotted and solid line in the post-peak regime is proportional to the excess energy released in the case of unstable failures.

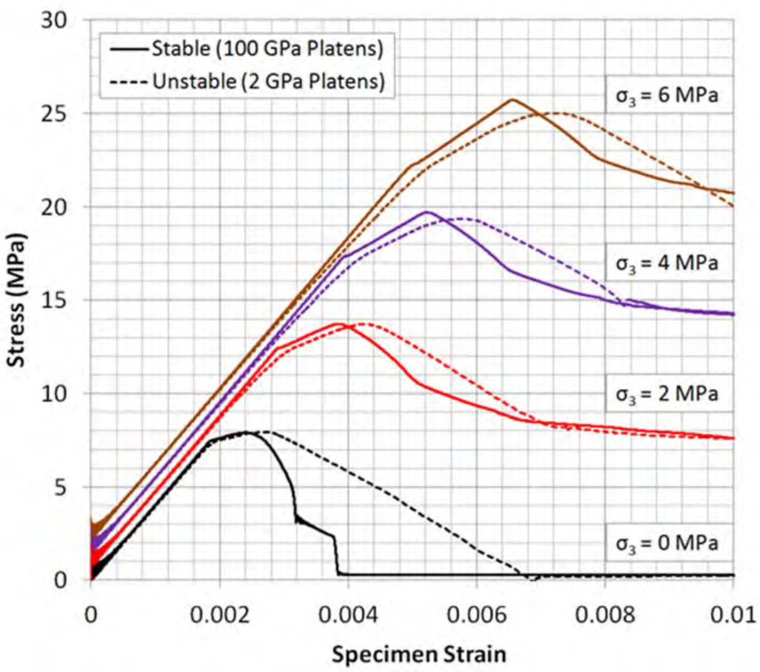

Fig. 3-12 Unstable and stable failures of triaxial compressive strength tests at different confinements.

To demonstrate the approach for determining the excess energy in Fig. 3-12, a set of uniaxial compressive strength tests were run in FLAC3D. First, a pair of stiff 100 GPa platens was used to fail a brittle rock specimen in a stable manner. The results of the energy balance in this case are shown in Fig. 3-13 where the calculated excess energy remained low throughout the test. Next, a pair of soft 2 GPa platens was used to cause unstable failure of the specimen with the resulting energy histories shown in Fig. 3-14. In this unstable case the excess energy increased during the specimen failure and matched expected values of energy released from the unstable system.

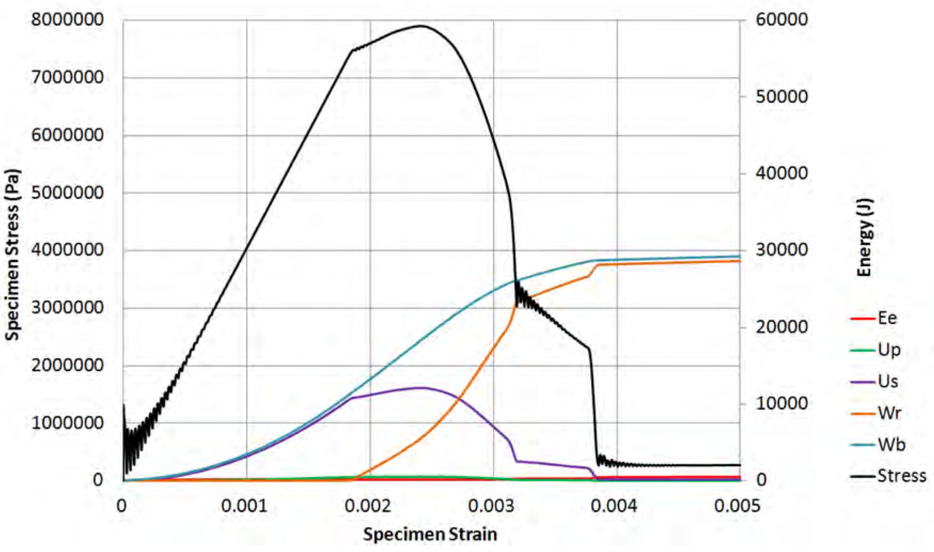

Fig. 3-13 Energy histories of stable UCS test with 100 GPa platens.

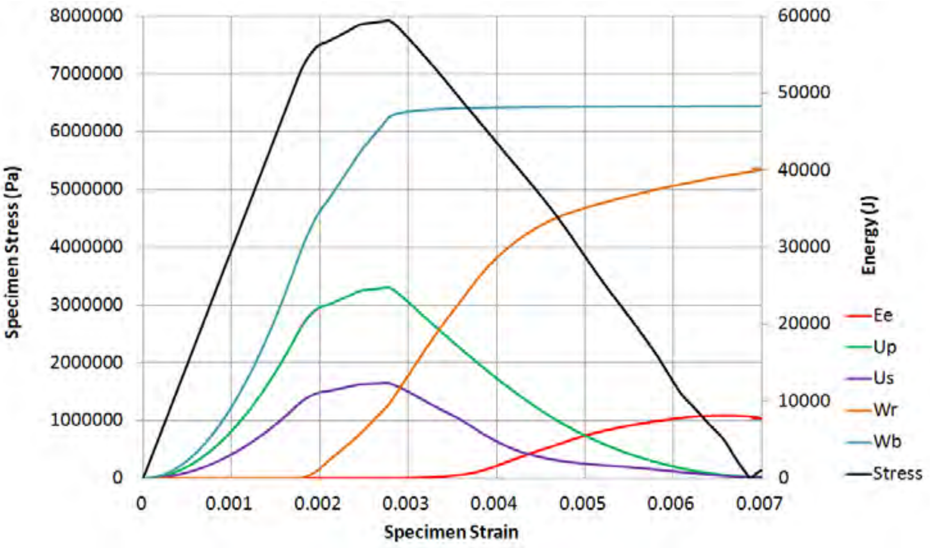

Fig. 3-14 Energy histories of unstable UCS test with 2 GPa platens.

Three-Dimensional tributary area models

Available numerical and constitutive models appear to simulate the stress-strain response of brittle rock while approximating the elastic and plastic energy stored or consumed during failure. Mine models may be constructed using these techniques to allow for unstable failure conditions to arise within simulated volumes of brittle rock. The explicit representation of failure given by FLAC3D allows for static energy calculations to be performed even while the system is unstable. The total excess energy may therefore be determined during simulated rock failure to provide an assessment of the bump-potential of a given mine layout.

The calculation of excess energy was implemented within a quarter-symmetry model of a pillar which represented an infinite room-and-pillar layout. Pillar geometries with width-to-height ratios from 1:1 to 5:1 were tested under these conditions to determine the excess energy released in each case. A coal seam of height of 2.4 m and an entry width of 6 m was assumed for the tests. The resulting model geometry is shown in Fig. 3-15.

A calibration procedure was applied to the simulated coal pillars to determine appropriate inputs for cohesion, friction angle, and dilation angle in the MCSS model. The ultimate strengths of the pillars were compared against the Bieniawski [5] and Salamon-Munro [49] pillar strength formulae as shown in Fig. 3-16. The post-failure modulus of the 2:1 and smaller pillars was also assessed against Wagner's classic in situ pillar tests [52]. The calibrated pillar responses shown in Fig. 3-17 were found to be within acceptable ranges for all pillar widths which were tested.

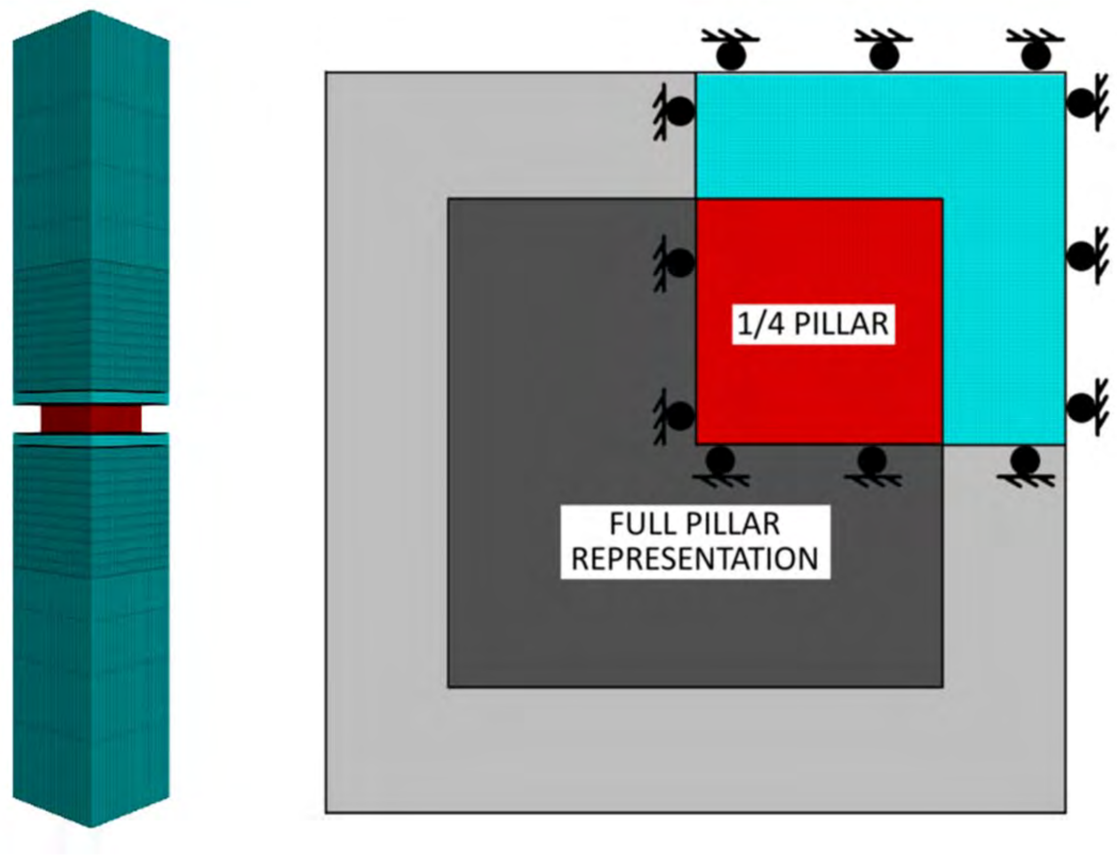

Fig. 3-15 Quarter-symmetry pillar model to represent an infinite room-and-pillar mining layout.

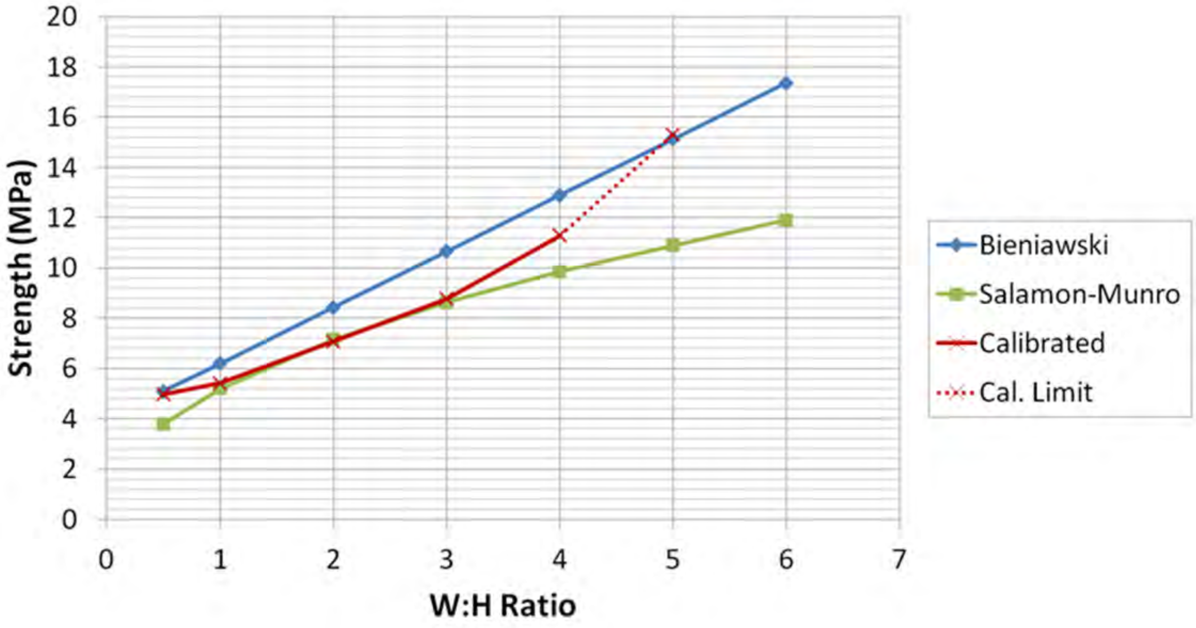

Fig. 3-16 Ultimate pillar strengths of calibrated coal pillars compared against classic coal pillar strength formulae.

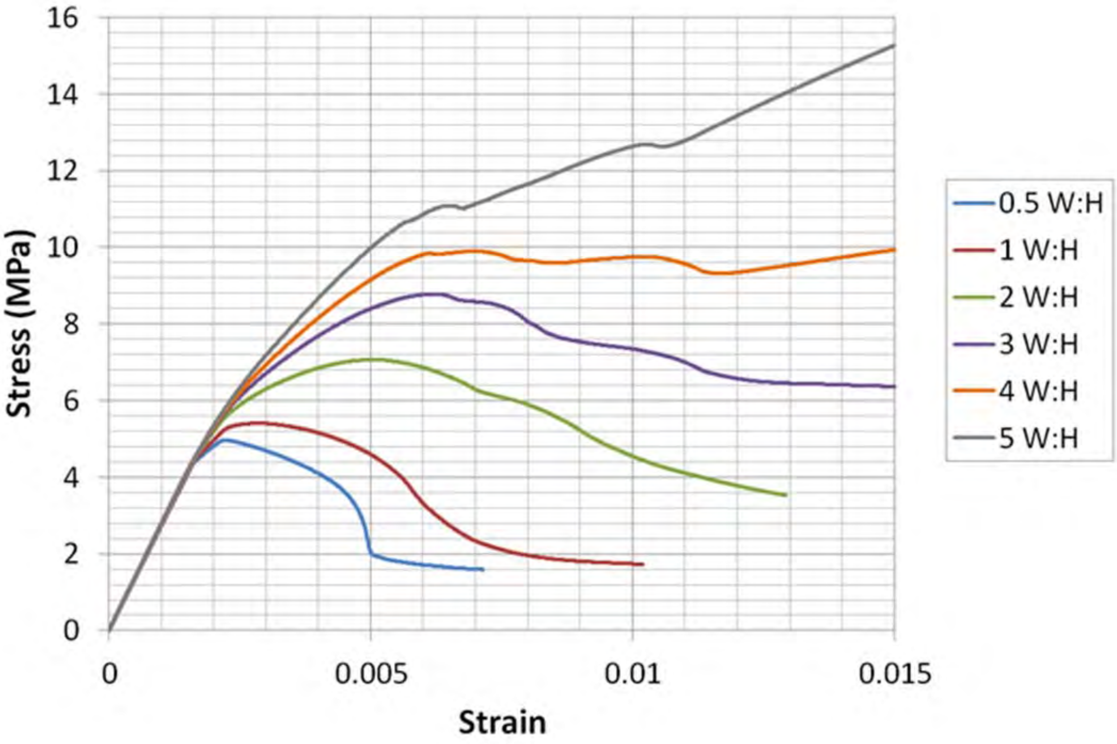

Fig. 3-17 Ultimate pillar strengths of calibrated coal pillars compared against classic coal pillar strength formulae.

Gravity was applied to the system and a pressure boundary was established at the top of the model to represent a tributary area load on the pillar. The pressure boundary was increased at a rate of 1 kPa per 100 steps until the pillar was caused to fail. Excess energy was calculated during these tests to assess the magnitudes of energy released due to unstable collapse of the room-and-pillar layouts.

Three-Dimensional model results

The role of gravitational potential energy was studied in the expression of unstable failure in the quarter-symmetry pillar models. The 1:1 to 3:1 pillars failed in a completely unstable manner which resulted in the unchecked downward displacement of the overburden. An example of the excess energy history is provided for the smallest 1:1 pillar in Fig. 3-18.

The 4:1 and 5:1 pillars were wide enough to maintain sufficient residual strength during failure to resist total collapse of the roof, however the formation of large shear failures in the wide pillars still resulted in temporary reductions in strength and subsequent losses of stability. This concept is demonstrated for the 4:1 pillar in Fig. 3-19 in which a small decrease in strength led to a significant increase in excess energy.

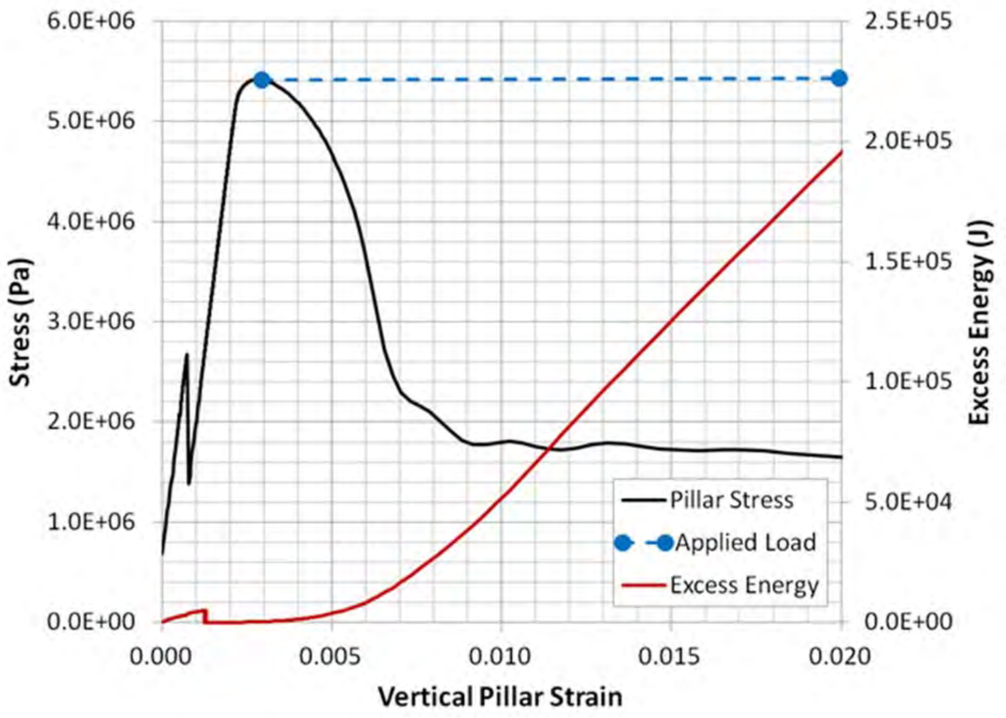

Fig. 3-18 Excess energy during unstable collapse of 1:1 pillar.

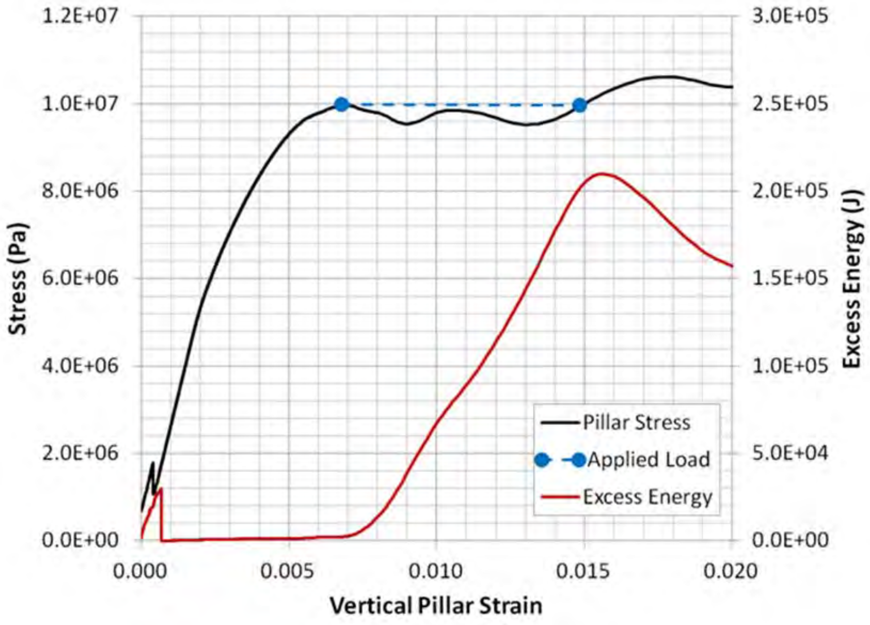

Fig. 3-19 Excess energy during failure of 4:1 pillar.

Fig. 3-20 shows the excess energy histories for the different pillar geometries normalized over the total development area. Larger magnitudes of normalized excess energy were recorded for the 1:1 through 3:1 pillars. The 4:1 and 5:1 pillars also showed some increase in excess energy as a consequence of large shear failures within the pillars.

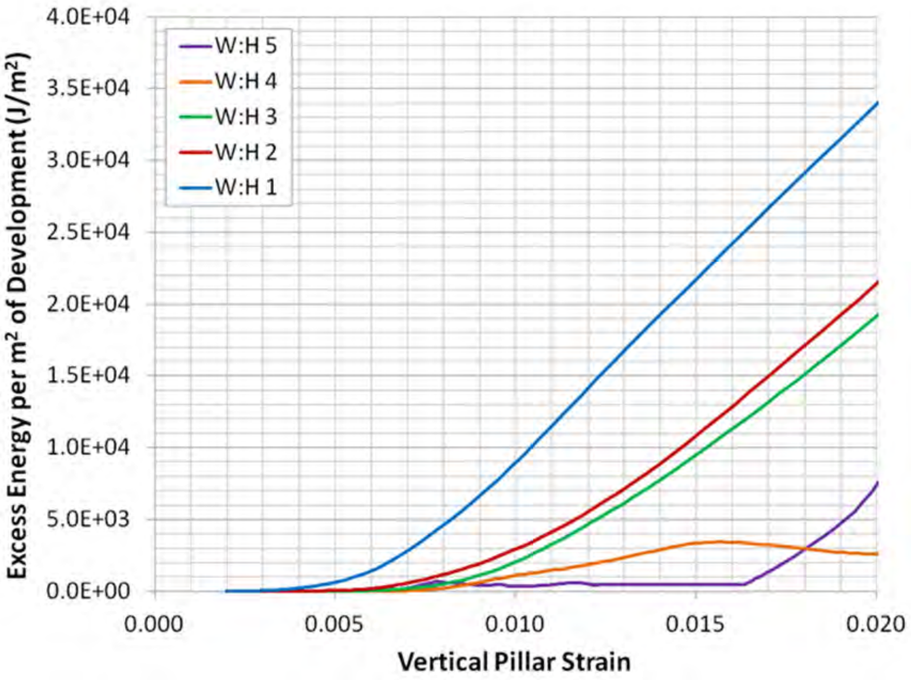

Fig. 3-20 Excess energy released per square meter of development for different pillar geometries.

The calculation of excess energy was shown to be a direct assessment of the stability of different room-and-pillar mine layouts. The results of the tests revealed that smaller pillars of widths 1:1 to 3:1 did not provide sufficient residual strength to resist downward displacement of the roof and a massive collapse was observed in these cases. The larger pillars led to more stable layouts however excess energy was still released due to temporary reductions in residual strength.

Two-Dimensional gateroad pillar models

To study the excess energy levels in the case of a gateroad pillars, a two-entry gateroad layout was assessed for pillar widths ranging from 1:1 to 5:1. The half-symmetry plane strain model shown in Fig. 3-21 was constructed in FLAC3D to represent an elastic rockmass loading a single gateroad pillar with two 6m entries to either side. Loads were increased in the system through a slow, constant velocity boundary at the top and bottom of the model. No gravitational loading was assumed for these simplified tests.

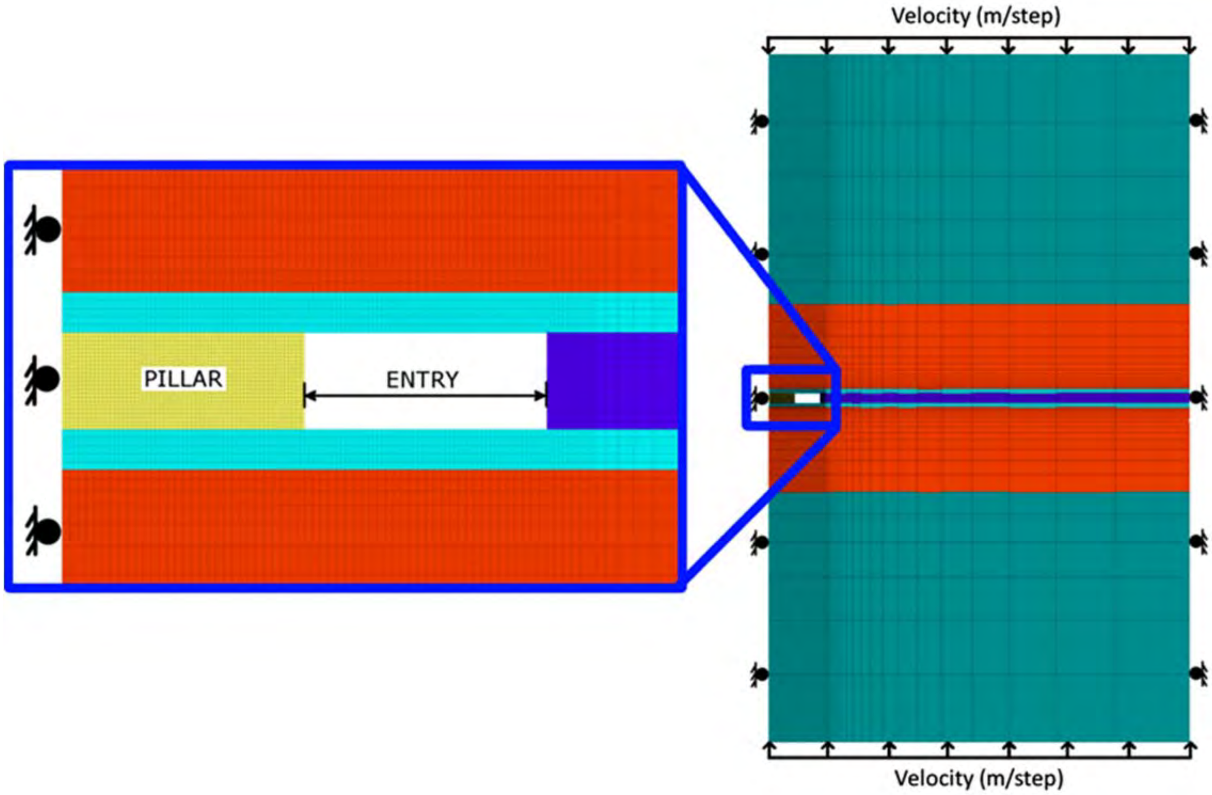

Fig. 3-21 Two-dimensional plane strain model of gateroad pillar.

The elastic modulus of the rockmass was adjusted between tests to allow more or less strain energy to be stored in the loading system prior to the failure of the pillar. Young's moduli of 2, 5, and 20 GPa were assigned to induce unstable, quasi-stable, and stable pillar failures, respectively. The stress-strain results of the 1:1 pillar are shown in Fig. 3-22 where the 2 GPa rockmass led to an unstable failure and a deviation of the post-peak pillar response from expected values.

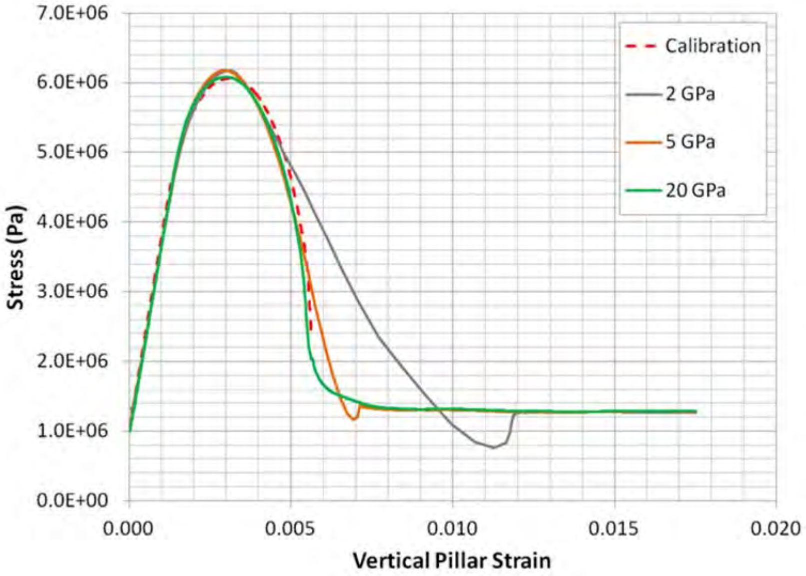

Fig. 3-22 Failure of 1:1 pillar by unstable 2 GPa, quasi-stable 5 GPa, and stable 20 GPa rockmass conditions.

The results of the excess energy calculations are shown in Fig. 3-23 for all test cases. Excess energy magnitudes increased with increasing widths in the unstable 2 GPa rockmass. These results revealed that more energy was released due to unstable failure conditions within the stronger, wide pillar cases.

Fig. 3-23 Excess energy released in gateroad models for increasing width-to-height ratio pillars.

The failure mode of the pillar played an important role in the stability of the simulated gateroads. Stress and strain measurements could be used for the smaller 1:1 and 2:1 pillars to directly identify the presence of unstable failure conditions however this approach became unsuitable for wider pillars which experienced complex, multi-stage failure modes. The calculation of excess energy provided the only direct assessment of unstable failure and bump-potential for the wider pillar geometries of 3:1 and greater. A more thorough discussion of the changing failure mode of pillars at different width-to-height ratios is provided in [Garvey, 2013].

UDEC analysis of discontinuity shear and compressive failure stability

In addition to the compressive failures discussed above, underground mining may also induce shear failures along major discontinuity planes. Such failures can occur in a stable or an unstable manner, depending on characteristic discontinuity shear stress–shear displacement behavior, stress field, and stiffness of the surrounding mine environment. Discontinuity failure stability has not been studied extensively and is still less understood than the concepts implied by the commonly used terms “strength” and “failure”. Failure stability impacts the occurrence of rockbursts and thus the damage they can do. Understanding failure stability is important especially in locations where rockbursts are likely, such as under high stress and in the presence of brittle discontinuity surfaces.

Past researchers have recognized unstable failures as the main cause of rockbursts, and identified post-peak softening as a contributor to unstable failure. But, rock discontinuities are still commonly treated as if they exhibit either elastic-plastic behavior or, less frequently, elastic-post peak softening behavior in their shear stress–shear displacement behaviors. Taking into account the correlation between unstable failure and softening post-peak behavior, Salamon [50] proposed a criterion for unstable shear failure based on the relative stiffness of the loading system and post-peak softening regime to express the conditions that result in rockburst events. Later, Rice [48] illustrated that the conditions for stable and unstable fault slips for a single degree-of-freedom system consisted of a slider and a spring. Both researchers suggested that an unstable shear failure of rock discontinuities occurs if the post-peak stiffness of the discontinuity shear stress-displacement curve is larger in absolute value than loading stiffness.

The objective of the slip-type bump mechanisms are first to develop a methodology for analyzing stable and unstable shear failures and then apply this methodology to better understand the mechanisms involved in slip-type rockbursts that are influenced by excavations, using an appropriate numerical model. The mechanistic analyses of unstable shear failures on rock discontinuities are carried out using the Universal Distinct Element Code (UDEC) [32]. The UDEC code was specifically developed for failure analyses in discontinuous rock mass, and incorporated a discontinuity “softening” constitutive model known as the continuously yielding (CY) joint model. The work done by Lemos [38] and Cundall and Lemos [14] indicated that UDEC with the CY joint model could be used to simulate unstable failure of rock discontinuities in the program’s dynamic analysis mode. We believed it might also be feasible to apply UDEC to model unstable failures in the more commonly used “quasi-static” mode. To evaluate this possibility, numerical simulations of laboratory shear test were performed, using test geometry similar to that of a typical double shear test configuration. The stiffness of the loading system was varied by changing the elastic modulus of the rock specimen, and the CY joint model developed by Cundall and Hart [**Error! Reference source not found.**] was adopted as the softening constitutive model. The results verified the program’s capability to simulate stable and unstable shear failures of rock discontinuities.

Following this, a model was built to achieve the second objective of the study: a better understanding of the mechanisms involved in slip-type rockbursts that are influenced by excavations. The model consisted of a geological discontinuity in the vicinity of an advancing underground excavation. Additional analysis aimed to determine how factors such as excavation extent, location of the discontinuity, and rock elastic modulus would influence loading stiffness and stability of the discontinuity.

Stiffness criterion of unstable discontinuity shear failure

The unstable failure criterion used in this study was based on Cook's [13] widely accepted criterion for unstable compressive failures of rocks, commonly known as strain-type rockbursts. Salamon [50] and Rice [48] extended this concept to account for unstable shear failures of discontinuities, commonly known as slip-type rockbursts. Fig. 3-24 illustrates the stiffness criterion for stable and unstable shear failures. In Fig. 3-24a, the block is subjected to a horizontal pull force T applied on the spring, resulting in a movement of δ_o. Depending on the magnitude of the normally applied stress σ_n, the block slides by an amount δ along the contact surface. The stiffness of the spring k is analogous to the loading stiffness in the case of a geological discontinuity. The characteristic behavior of the contact surface is represented by a post-peak softening stress-displacement behavior as shown in Fig. 3-24b. In this figure, the spring stiffness remains greater than the post-peak stiffness of the shear stress-displacement curve of the contact surface, which allows stable shear failure to occur at the contact surface. In Fig. 3-24c, a spring with a smaller stiffness than the post-peak stiffness of the contact surface can result in unstable shear failure at the surface, triggered at the point marked "instability."

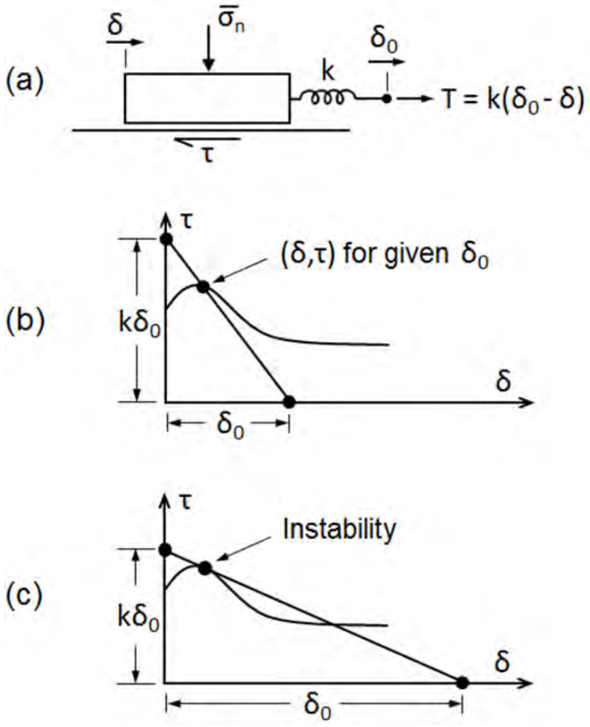

Fig. 3-24 Conditions for stable and unstable shear failure in a single degree-of-freedom system, after Rice [48].

Continuously yielding joint model

UDEC is a two-dimensional numerical program based on the distinct element method of modeling discontinuous media, such as a jointed rock mass. The discontinuous medium is represented as an assemblage of rigid or deformable discrete blocks separated by discontinuities [32]. One of the main reasons for using UDEC in this study is that post-peak softening behaviors of discontinuities can be effectively simulated by the CY joint model in the program. The CY joint model was originally intended to simulate internal mechanisms of progressive damage of discontinuities under shear [**Error! Reference source not found.**]. Unlike the Mohr-Coulomb plasticity model, the CY joint model accounts for joint shear and normal stiffness dependence of normal stress and non-linear hardening and, importantly, softening behavior in the post-peak stage, as normally observed in physical discontinuity shear tests.

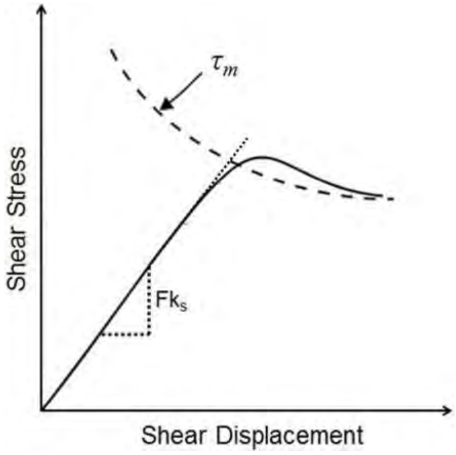

Fig. 3-25 Schematic of typical shear stress-displacement curve and the target shear strength τm of the CY joint model [32].

The discontinuity shear stress–displacement curve in a CY joint model always approaches a target shear strength τ_m by changing the instantaneous gradient of the curve based on the difference between strength and stress (Fig. 3-25). Dilation angle is considered as the difference between the apparent and the residual friction angles. The target shear strength τ_m is a function of normal stress and accumulated plastic shear displacement of the simulated discontinuity. As normal stress increases, target shear strength increases. The increase in the target shear strength results in an increase in shear strength of the modeled discontinuity. The target shear strength continuously decreases as the accumulated plastic shear displacement increases. This results in a softening behavior in the post-peak region of the discontinuity shear stress-displacement behavior. In this study, shear stiffness of a discontinuity is defined as the ratio of applied shear stress to shear displacement in a linear elastic regime, and has a unit of Pa/m. The shear stiffness of the CY joint model is controlled by the shear stiffness parameter k_s. Normal stiffness of discontinuity is defined as the ratio of applied normal stress to normal displacement and is expressed using the same unit as shear stiffness, Pa/m.

Double shear test model

To examine the ability of UDEC with the CY joint model in simulating stable and unstable shear failures of rock discontinuities, a series of laboratorial-scale double shear tests were simulated. The model consisted of three rectangular blocks, as shown in Fig. 3-26. Each block was made deformable by discretizing it into a mesh of triangular finite-difference zones, as delineated by the red lines in the figure. The top and bottom blocks in the Fig. represent two loading platens, and the middle block represents a rock specimen. The height of each block is 0.1 m, the width of the loading platens is 0.3 m and of the rock specimen is 0.2 m.

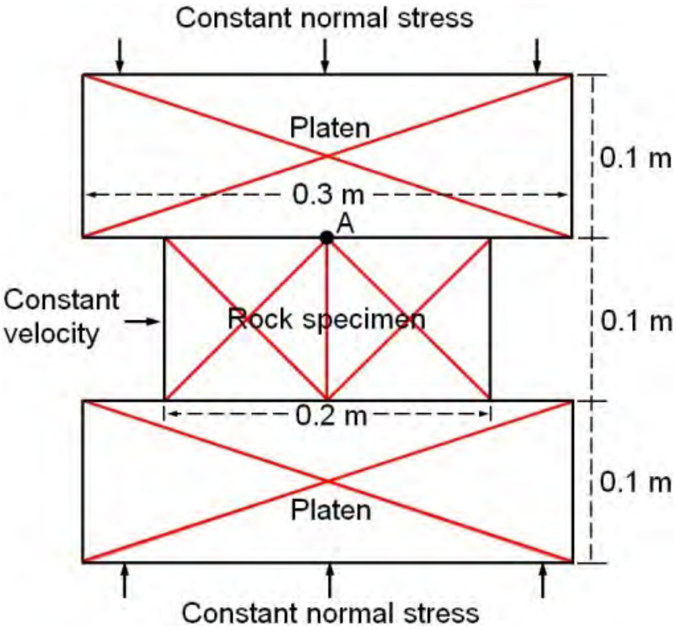

Fig. 3-26 Configuration of double shear test model in UDEC.

The loading platens are incompressible and free to move in the vertical direction, and were fixed in the horizontal direction. The rock specimen was modeled as an elastic material with varying elastic moduli among different tests. In this model, the interfaces between the rock specimen and the loading platens were assigned the CY joint model. These interfaces represent rock discontinuities on which shear failures can occur. A constant normal stress of 10 MPa was applied at the top and bottom of the model, as indicated by the vertical arrows in the figure, to simulate normal loading on the rock discontinuity. A constant horizontal velocity of 0.1 mm/s was applied over the left side of the rock specimen. Shear stress and shear displacement of point A, as indicated by the black dot at location "A" in Fig. 3-26, was recorded to represent the behavior of the middle section at the upper discontinuity.

Energy stored in the loading platens was minimized by assigning them an unrealistically high elastic modulus of 2000 GPa. As such, during shearing along the discontinuities, the loading system energy was available mainly from the elastic rock specimen. To simulate discontinuity stable and unstable shear failures, the loading stiffness was varied by changing the elastic modulus of the rock specimen in different tests. The loading stiffness is defined as a measure of the resistance offered by the elastic loading system to its deformation at a given point, and has a unit of GPa/m.

An elastic modulus of 200 GPa was assigned to the rock specimen in the first test to obtain the characteristic behavior of the discontinuity. Then, two tests were performed, each with smaller elastic moduli assigned to the rock specimen: one with an elastic modulus of 50 GPa to simulate the shear failure under stiff loading, and the other with an elastic modulus of 1 GPa to simulate the shear failure under soft loading. The elastic modulus of the loading platens was the same in all three tests. The input parameters of the elastic model for the three tests are shown in Table 3-1.

Table 3-1 Input parameters of the elastic model for different tests.

	Elastic Modulus [GPa]	Poisson's Ratio
Steel Platens	2000	0.2
Specimen-very stiff loading system	200	0.2
Specimen-stiff loading system	50	0.2
Specimen-soft loading system	1	0.2

For the discontinuity in the double shear tests, the CY joint model with a given set of properties was used, as listed in Table 3-2. The CY joint model using these input parameters was similar to a joint model with a friction angle of 38° and no cohesion.

Table 3-2 Input parameters of the CY joint model.

Description	Value
Joint normal stiffness	100 GPa/m
Joint shear stiffness	100 GPa/m
Joint normal stiffness exponent	0
Joint shear stiffness exponent	0
Joint intrinsic friction angle	30°
Joint initial friction angle	59.3°
Joint roughness parameter	0.1 mm

Discontinuity characteristic behavior

The shear stress-displacement behavior at point A for the case of specimen modulus of 200 GPa is shown by the black line in Fig. 3-27. This curve represents the characteristic behavior, which is defined as the behavior that a discontinuity exhibits during a shear test with loading stiffness is significantly greater than the post-peak stiffness of the discontinuity. As such, this curve represents the discontinuity behavior when the discontinuity undergoes a stable shear failure.

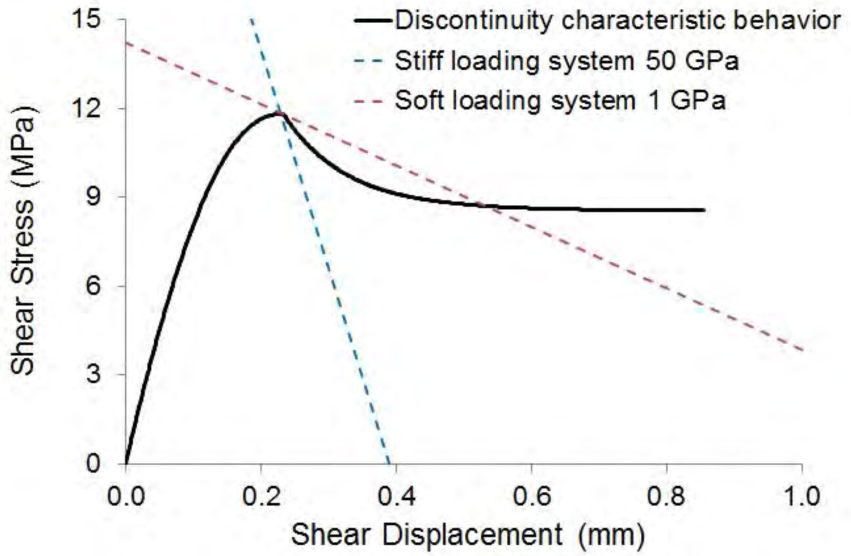

Fig. 3-27 Characteristic shear stress–shear displacement behavior of the middle section at the upper discontinuity, and the stiffness of the stiff and soft loading systems.

Loading stiffness

The test model is shown in Fig. 3-28. Due to the symmetry condition in the double shear test geometry, only the loading stiffness of point A on the upper half of the rock specimen was considered.

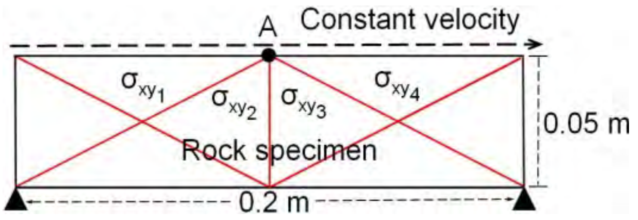

Fig. 3-28 Model of loading stiffness test.

The model was fixed at the bottom in both horizontal and vertical directions. A constant horizontal displacement was applied over the top surface of the model as shown by the arrow in the figure. During loading, shear stresses in the four zones adjacent to point A, as well as the horizontal displacement of point A, were monitored. According to the program's algorithm, one third of the shear stress within each adjacent zone contributes to the failure of the point. Therefore, the loading stiffness (LS) was calculated as follows,

$$LS = \frac{(1/3)(\sigma_{xy1} + \sigma_{xy2} + \sigma_{xy3} + \sigma_{xy4})}{d_A}$$

where σ_{xy_i} is the shear stress in zone i (i=1, 2, 3, 4) and d_A is the horizontal displacement of point A. The results of the stiffness tests with the rock specimen assigned elastic moduli of 50 GPa (the stiff loading system) and 1 GPa (the soft loading system) are shown in Fig. 3-27 as the blue and red dashed lines, respectively.

Stiff and soft loading conditions

Double shear tests were performed under stiff and soft loading conditions. The results are presented in three different formats in Figs. 3.29, 3.30, and 3.31. The time unit in the plots is a numerical time calculated by multiplying the time step by the number of steps used in the simulations. Although numerical, this time is an indicator of the suddenness of the failure, which in turn relates to the failure stability.

Fig. 3-29 shows the shear displacement–time curves of point A under the stiff (blue line) and soft (red line) loading system conditions. The smooth and continuous change in the shear displacement under stiff loading indicates discontinuity undergoing a gradual shear, which implies a stable shear failure. The slight variation in the blue line at 1.6 seconds marks the onset of stable failure. The rate of change in the shear displacement increases slightly after the stable failure takes place.

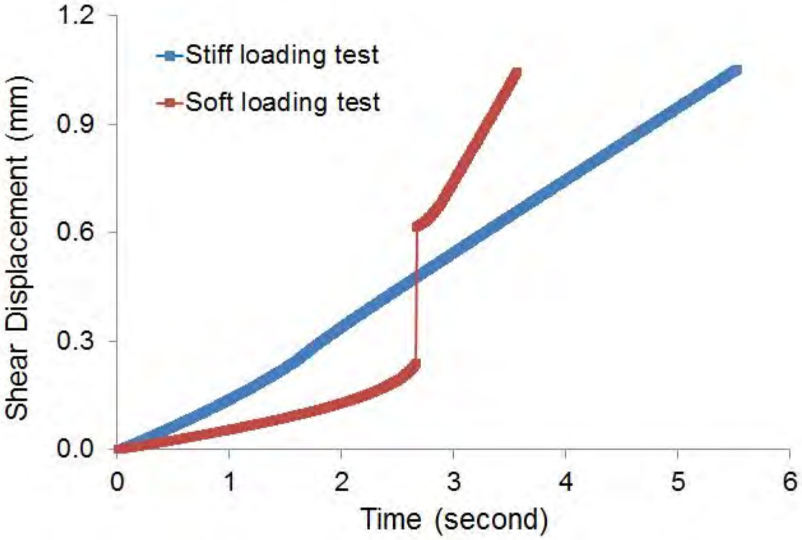

Fig. 3-29 Shear displacement–time curves of the middle section at the upper discontinuity under stiff (blue line) and soft (red line) loading conditions.

The interruption in the discontinuity shear displacement trend represented by the red line in the soft loading system test shows that the discontinuity goes through a rapid and discontinuous increase. The shear displacement rapidly jumps from 0.24 mm to 0.62 mm at the time of 2.7 seconds. This phenomenon implies a sudden shear process that can be postulated as an unstable shear failure. This postulation is further supported by the test results in Figs. 3.30 and 3.31.

Fig. 3-29 also shows that, for the unstable failure, the rate of change in shear displacement increases sharply in the post-failure region. However, the slopes of the red and blue lines are not directly comparable because the time scale is determined by the time-step, which is affected by the stiffness of the materials used in the model, and the rock material in these two models are assigned different elastic moduli.

Behaviors similar to those in Fig. 3-29 are observed in Fig. 3-30, where the results are plotted in the shear stress–time format. The gradual decrease in the shear stress, as shown by the blue line, suggests that the discontinuity undergoes a stable shear failure. Under the soft loading (red line), a rapid drop in the shear stress of the discontinuity from 12.3 to 8.3 MPa at 2.7 seconds indicates an unstable shear failure. As noted previously, the slopes of the pre-peak regions of the curves cannot be directly compared.

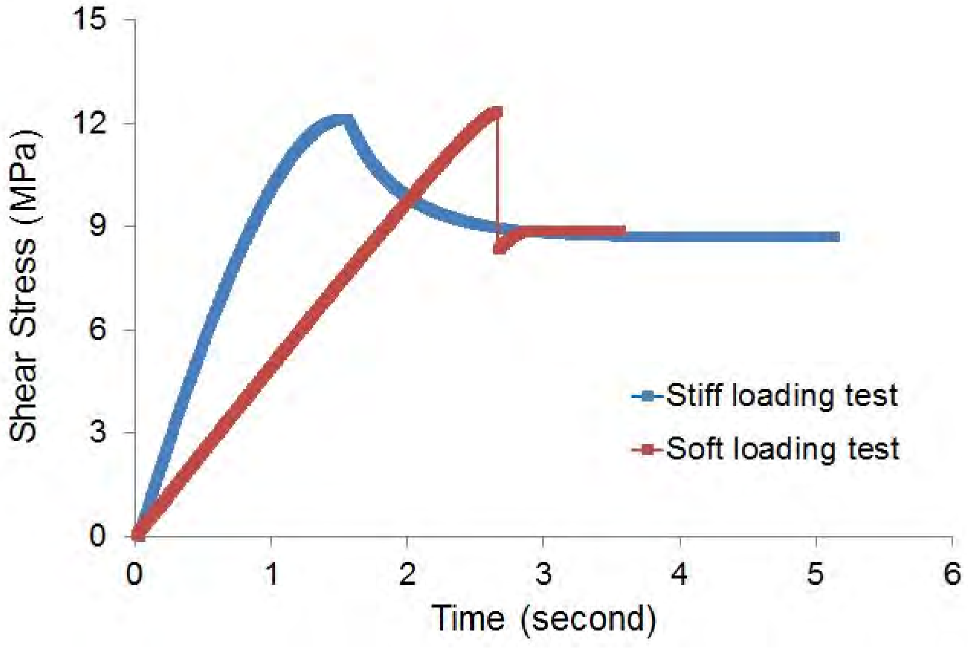

Fig. 3-30 Shear stress–time curves of the middle section at the upper discontinuity under the stiff (blue line) and soft (red line) loading system conditions.

The results of the stiff and soft loading system conditions are also presented in the form of shear stress–shear displacement plots in Fig. 3-31. The dashed lines in red and blue represent soft and the stiff loading conditions, respectively. The shear stress–shear displacement curves of the discontinuity under the stiff and soft loading both undergo a gradual increase in the shear stress in their elastic regions. The blue line is not visible in its elastic region because it is completely covered by the red line.

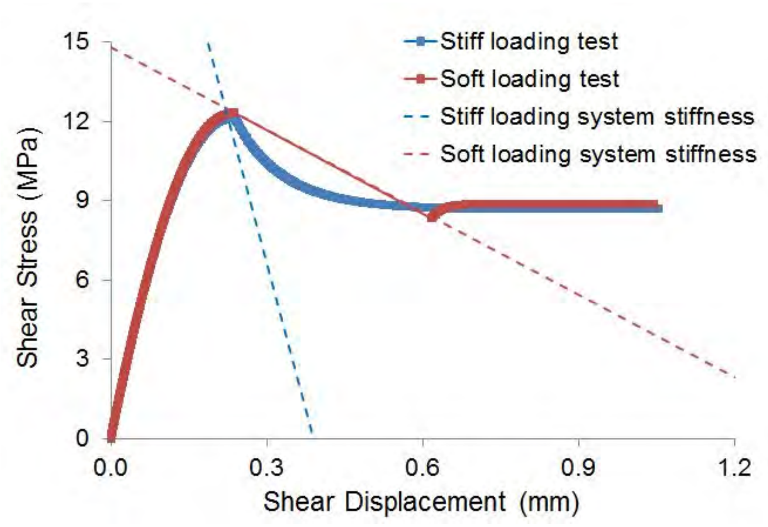

Fig. 3-31 Shear stress–shear displacement curves of the middle section at the upper discontinuity under the stiff (blue line) and soft (red line) loading system conditions.

Double shear tests under different normal stresses

It is generally accepted that the failure response of a discontinuity to shear loading can be significantly affected by the normal stress acting on the discontinuity [3, 48]. To study the ability of the model in realistic loading conditions, the double shear tests were repeated for a series of normal stress values ranging from 4 to 28 MPa. In this series, the CY joint model was adopted as the constitutive model and the loading stiffness was set excessively high (200 GPa) to ensure that the model produces the characteristic behavior of the discontinuity. The properties used for the discontinuity are the same as given in Table 3-2.

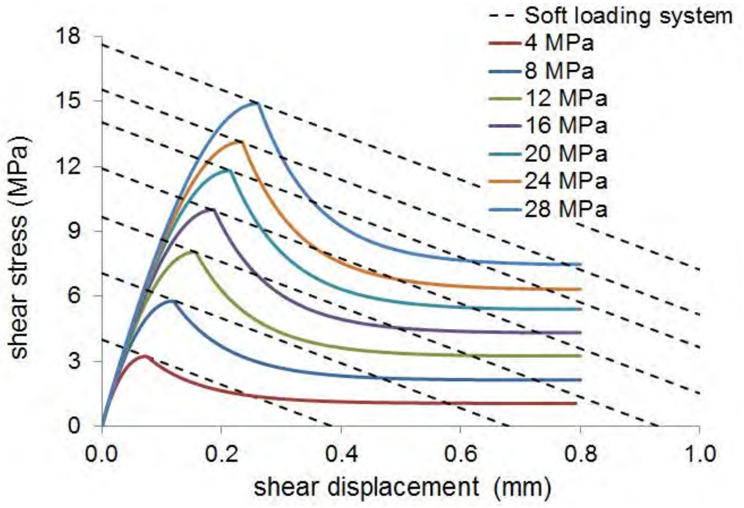

Fig. 3-32 Shear stress–shear displacement curves of the simulated discontinuity under different normal loading conditions.

The test results are shown in Fig. 3-32 in the form of shear stress–displacement relationship. The solid lines in different colors are the characteristic discontinuity stress-displacement responses to loading in shear under varying normal stress levels. The dashed lines represent a soft (1 GPa) loading system, which are superimposed on the characteristics lines to emphasize the magnitude of the variations in stress drop and excess energy as function of increasing normal stress. The shear stress drop magnitudes determined by subtracting the residual strength from peak strength for each line are presented in Table 3-3, which shows significant increase in stress drop with increasing normal stress. The plots also indicate that the excess energy magnitudes, which are defined by the area between the loading system and post-peak lines for each test, become increasingly greater with increasing normal stress. The shear stress drop magnitudes as determined from Fig. 3-32 are presented in Table 3-3, which shows significant increase with increasing normal stress.

Table 3-3 Shear stress (MPa) drop (Fig. 3-32) under different normal stress conditions.

Normal Stress	Shear Stress Drop
4	2.2
8	3.7
12	4.8
16	5.7
20	6.4
24	6.8
28	7.4

These results compare well with the findings from other researchers that both stress drop and excess energy increase with increasing normal stress [4, 18, 36, 48]. Also, such increases are often considered as the main causes of greater rockburst magnitudes as mining goes deeper where discontinuity failures occur under high normal stress conditions. Based on these findings, we conclude that the CY joint model appropriately simulates the variations in discontinuity behavior under different normal loading conditions.

Discontinuity model in mine scale

The model used in this section aimed analyzing the stability of a rock discontinuity and included an underground excavation and a pre-existing geological discontinuity, as shown in Fig. 3-33. The model had a width of 140 m and a height of 160 m. The discontinuity ran through the model in the horizontal direction. A rock layer, in which the excavation area was located, was set 2 m below the pre-existing geological discontinuity and assigned the same material properties as the rest of the rock mass in the model.

The shaded region in Fig. 3-33 represents the excavation area, with a width of 20 m and a height of 2 m. The inset in the figure is an enlarged view of the excavation area. In the inset, the horizontal solid black lines represent the numerical discontinuities. For the purposes of this study, the program was set to consider only the pre-existing rock discontinuity, labeled "Discontinuity" in the figure, as the real discontinuity that could fail in shear. The rest of the numerical discontinuities were taken as fictitious discontinuities that could not fail. The excavation area is divided into 80 slender blocks, which were further discretized into a mesh of triangular finite-difference zones.

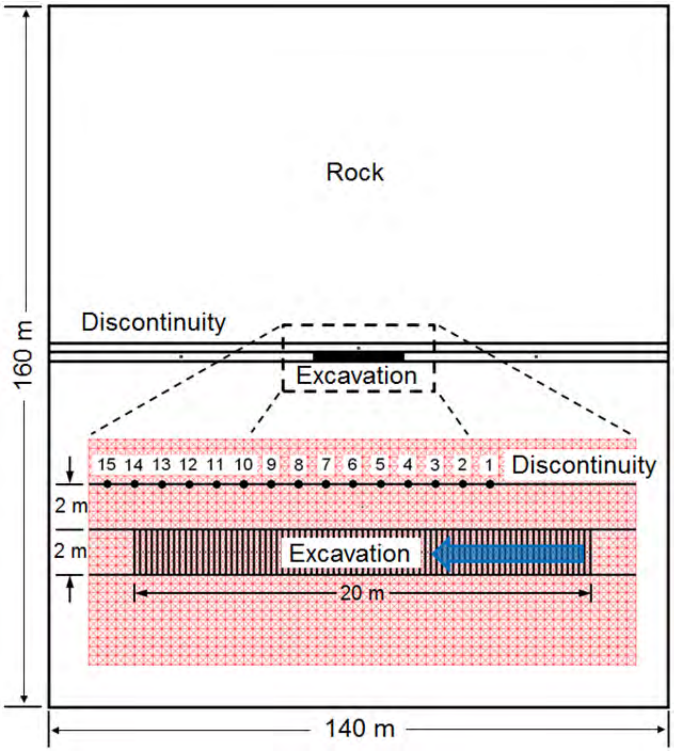

Fig. 3-33 Configuration of the model for discontinuity stability analysis.

The discontinuity was modeled as a CY joint model with its input parameters given in Table 3-2. The Mohr-Coulomb plasticity model was assigned to the fictitious discontinuities. An elastic modulus of 70 GPa and a Poisson's ratio of 0.2 were used in the elastic model for the rock layer and rock masses. The simulations were also run for 50 GPa elastic modulus. Considering the conditions of relatively deep underground mines, the model assumed an in-situ stress field of 17.5 MPa in the vertical direction and 5.25 MPa in the horizontal direction to simulate an excavation at 700 m depth with a coefficient of lateral stress k of 0.3. The left and right boundaries of the model were fixed in the horizontal direction, and the top and bottom boundaries were fixed in the vertical and horizontal directions to simulate far field boundaries.

Test procedure

Fifteen measurement points along the discontinuity shown in the inset in Fig. 3-33 were chosen. At each chosen point, shear displacement, shear stress and normal stress were recorded while advancing the excavation. The model was brought to equilibrium before any mining cut was introduced. The excavation area consisted of 80 successive mining steps. These steps were initiated sequentially in the direction indicated by the blue arrow in the inset. One mining step was simulated by removing one slender block at a time, then running the model to equilibrium. This procedure was repeated until all mining steps were complete.

Results on all measurement points

Recorded normal stresses for the points chosen for the stability analysis are plotted in Fig. 3-34 in the form of the normal stress–time curves. Positive normal stress indicates compressive loading. The different colors in the figure represent the responses of different measurement points. The squares indicate the recorded data. The small, step-like curved features in the plots show normal stress formation at the measurement points while the model is equilibrating after a mining cut. In a given curve, the vertical sections with less data points [not clear] represent the normal stress evolution in the process of excavation. Mining cuts change normal stress distribution on the discontinuity. As the excavation face approaches the location of the measurement points, the normal stresses at the points increase. The normal stresses reach their maximum values before the excavation face reaches the measurement points. As the excavation moves pass the points, the normal stresses decrease.

The shear displacement records of all measurement points are shown in Fig. 3-35 as shear displacement–time curves. The positive direction of shear displacement is indicated in the inset at bottom left. Points 1 to 5 initially experience increase-decrease processes of shear displacement in the positive shear direction as they are loaded and unloaded by the advancing excavation. They then undergo increases in shear displacement in the negative shear direction as the excavation face advances further. Points 6 to 9 undergo increase-decrease processes of shear displacement only in the positive shear direction. Points 10 to 15 experience only increases in the shear displacement in the positive shear direction. The shear directions for points 6 to 15 are not reversed in the process of excavating. The changes in the shear displacements of points 1 to 7 are gradual and smooth. Based on the results in Figures 3.29, 3.30, 3.31, these measurement points undergo stable shear failures. Rapid changes in shear displacement are observed at points 8 to 13, which implies the occurrence of unstable shear failures at these points.

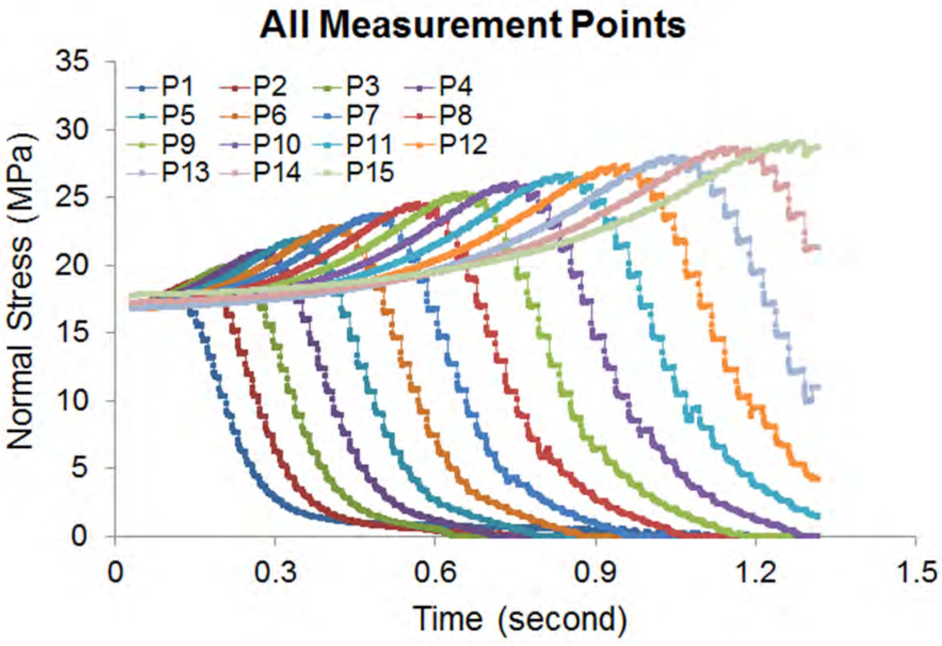

Fig. 3-34 Normal stress–time plots of all measurement points in the discontinuity stability test.

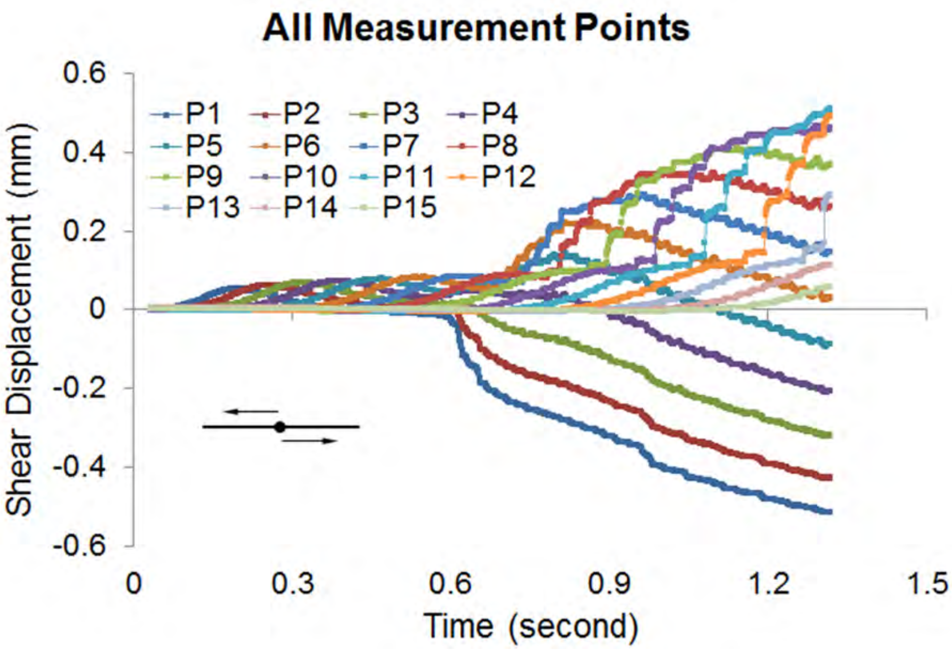

Fig. 3-35 Shear displacement–time plots of all measurement points in the discontinuity stability test.

The recorded shear stress at all measurement points is plotted in Fig. 3-36 in the form of the shear stress–time curves. The positive shear stresses indicate that the shear direction of the points is the same as that shown in Fig. 3-35. The advancing excavation results in changes in the shear stresses on the discontinuity. The shear stresses increase as the excavation face approaches the measurement points, and the maximum shear stress is approached when the excavation face is closer to the point. As the excavation moves away from the points, the shear stresses start decreasing. Points 1 to 6 sustain the maximum shear stress mobilized on them without failing. When the excavation face passes these points, their shear stress levels start to reduce. No failure occurs in this area until about 0.6 seconds. The changes in the shear stresses are gradual for points 1 to 6 in their failure process, which suggests that stable shear failures take place. The shear stresses at points 8 to 13 increase suddenly before they reach their maximum values. This is likely because shear stresses were unsustainable at contact points between the measurement points, which resulted in failure occurring prior to the measurement point, and contributed to the sudden increase in shear stresses. The shear stresses at these contact points are redistributed and transfer to the non-failed points (points 8 to 13). The additional shear stress exceeds the shear strength at points 8 to 13 and results in shear failures at these points. Rapid decreases in the shear stresses at the failure regions of points 8 to 13 imply the occurrence of unstable shear failures. Point 7 starts to fail at about 0.7 seconds and experiences a small rapid change in shear stress at this time, which can be considered as a transitional failure state between stable and unstable shear failure. This transitional failure state will be called a semi-stable failure in the remainder of this paper. Points 14 and 15 are in their elastic regimes in the entire excavation process.

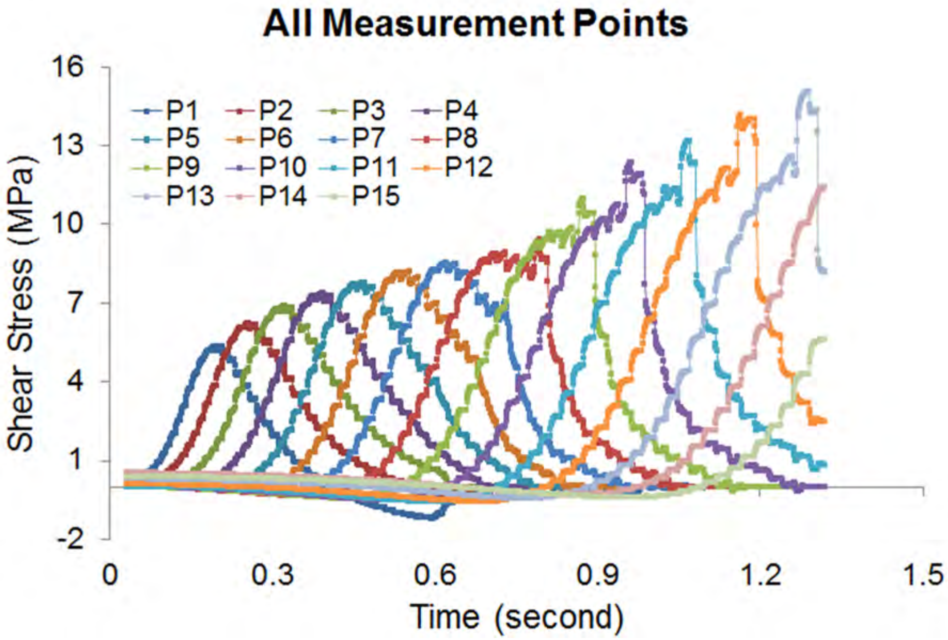

Fig. 3-36 Shear stress–time plots of all measurement points in the discontinuity stability test.

More information about shear failures at the measurement points is provided in Table 3-4. The table lists the time at which shear failures initiated, the x-coordinate of the measurement points, the location of the excavation face when shear failure occurred, the horizontal distance between each point and the excavation face when the point started to fail, and the failure stability in terms of stable, semi-stable, unstable. The origin at x=0, y=0 of the Cartesian coordinate system is located at the center of the model. The x-axis is in the horizontal direction and oriented to point to right. The y-axis is in the vertical direction and oriented to point upwards. In this coordinate system, the right side and the left side of the excavation area are located at 10 m and -10 m, respectively, on the x-axis.

It can be seen in Table 3-4 that, generally, shear failures occur in sequence at the measurement points: failures initiate from the points at the right-hand side and propagate to the left-hand side, from point 1 to point 15. However, point 1 and 2 do not follow this trend; they fail after point 5 fails. Table 3-4 also shows that shear failures of the points take place after the excavation face passes the locations of the measurement points. The horizontal distance between the measurement points and the excavation face at the instant of shear failure reduces as the failures propagate to the left of the model. Normal stresses at the measurement points when failures occur increase from 0.76 MPa for point 1 to 12.20 MPa for point 13. Higher normal stresses lead to higher shear strengths at the points. They also result in higher shear stress drops at points 8 to 13 (see Fig. 3-36), which indicates increased intensity of unstable shear failures. At the beginning of the excavation process, stable shear failures occur at measurement points 1 to 6. As the excavation face advances, unstable shear failures start to take place at points 8 to 13 with increased intensity—as signified by the amount of rapid shear stress drop. The change in failure stability of the points is caused by variations in stress distribution and loading stiffness that occur in the surrounding rock during the mining process.

Table 3-4 Information about the shear failures at the measurement points in the discontinuity stability analysis test.

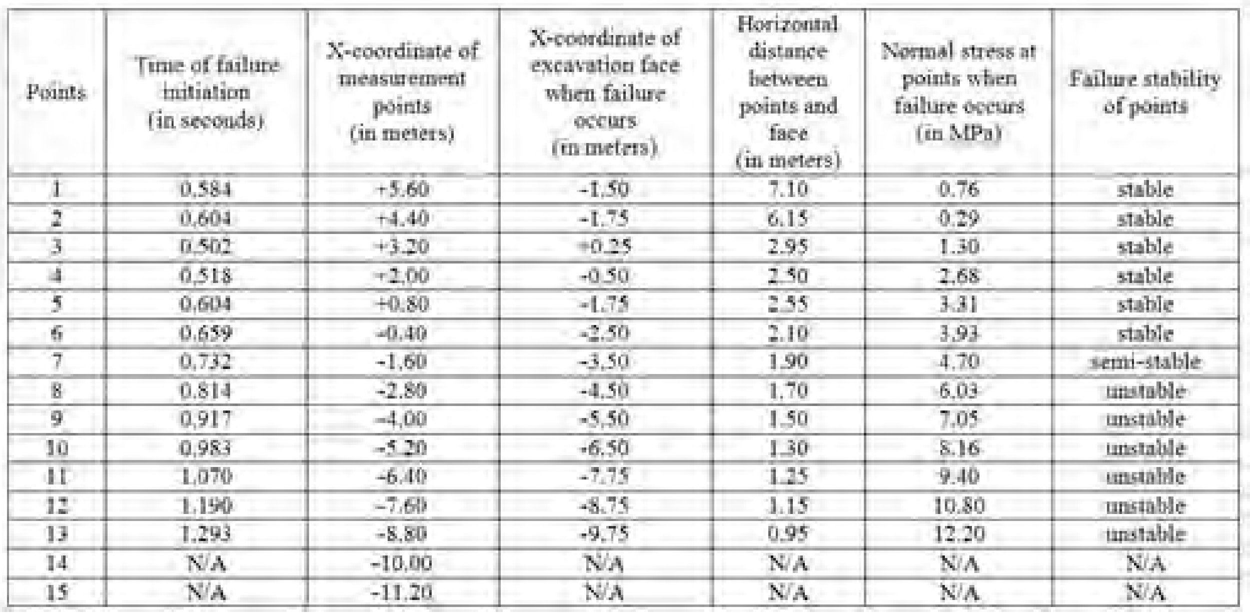

Points	Time of failure initiation (in seconds)	X-coordinate of measurement points (in meters)	X-coordinate of excavation face when failure occurs (in meters)	Horizontal distance between points and face (in meters)	Normal stress at points when failure occurs (in MPa)	Failure stability of points
1	0.584	+5.60	-1.50	7.10	0.76	stable
2	0.604	+4.40	-1.75	6.15	0.29	stable
3	0.502	+3.20	+0.25	2.95	1.30	stable
4	0.518	+2.00	-0.50	2.50	2.68	stable
5	0.604	+0.80	-1.75	2.55	3.31	stable
6	0.659	-0.40	-2.50	2.10	3.93	stable
7	0.732	-1.60	-3.50	1.90	4.70	semi-stable
8	0.814	-2.80	-4.50	1.70	6.03	unstable
9	0.917	-4.00	-5.50	1.50	7.05	unstable
10	0.983	-5.20	-6.50	1.30	8.16	unstable
11	1.070	-6.40	-7.75	1.25	9.40	unstable
12	1.190	-7.60	-8.75	1.15	10.80	unstable
13	1.293	-8.80	-9.75	0.95	12.20	unstable
14	N/A	-10.00	N/A	N/A	N/A	N/A
15	N/A	-11.20	N/A	N/A	N/A	N/A

Characteristics of stable, semi-stable and unstable failure mechanisms

Stable failure

The shear displacement–time plot of point 5 is shown in Fig. 3-37. Point 5 starts to fail at 0.6 seconds, which is marked by the black dashed line in the figure. Prior to the failure, shear displacement magnitude increases. The interval to the left of the line is the pre-failure regime, and the interval to the right is the post-failure regime. In the pre-failure regime, all elastic shear displacements are in the positive shear direction, although the displacement magnitudes start decreasing as the mining face passes by. In the post-peak regime, the shear displacement first decreases to zero and then becomes negative and starts increasing in magnitude.

As the excavation face advances, the shear stress at point 5 first increases and then decreases until it reaches a constant value of zero. The maximum shear stress is achieved when the excavation face is located close to point 5. No shear failure occurs at point 5 until about 0.6 seconds. Then, the gradual, continued decrease in shear stress indicates the occurrence of a stable shear failure.

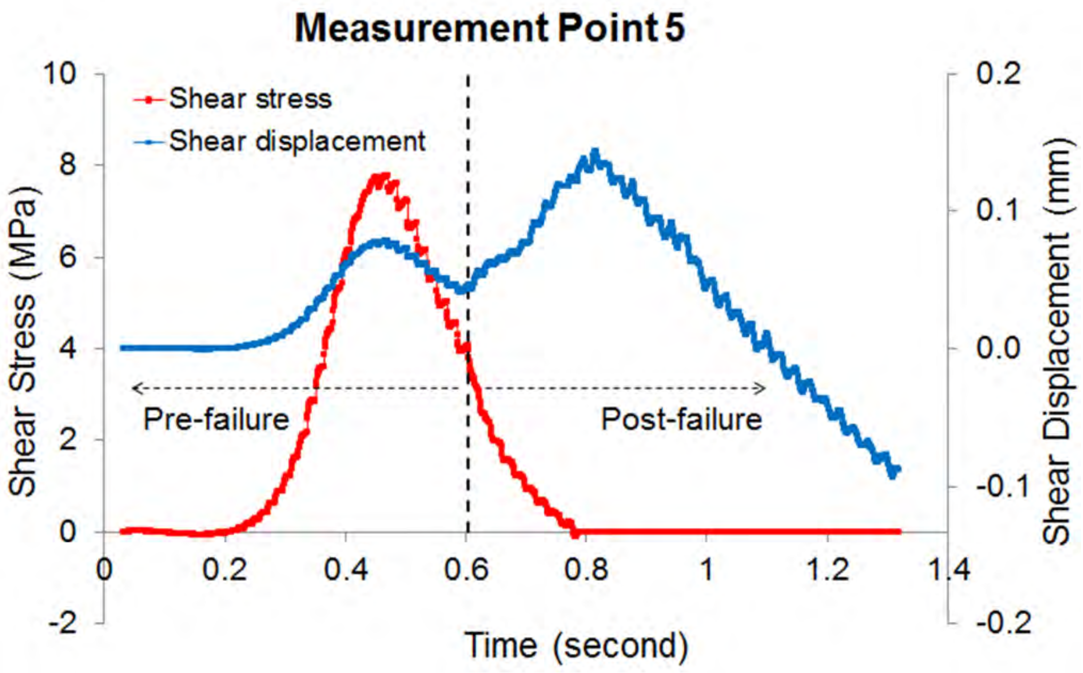

Fig. 3-37 Shear displacement–time plot of measurement point 5.

Further details of the shear behavior of point 5 are depicted as five distinct stages in Fig. 3-38. In the first stage, the shear stress and shear displacement increase as the mining face moves toward the left. The shear stress and shear displacement reach their peak values when the mining face barely passes the measurement point (Fig. 3-38a). In the second stage, the shear stress and shear displacement start decreasing as the mining face moves away from the point, which signifies an elastic unloading process (see Fig. 3-38b). With the initiation of shear failure at the point in the third stage, the shear stress keeps reducing until it reaches zero, and the shear displacement begins to rise again until it reaches the second peak value of the displacement (Fig. 3-38c). In the fourth stage, the shear stress remains at zero, and the shear displacement decreases to zero in the positive direction (see Fig. 3-38d). This stage exists because the lower section of the failed discontinuity at point 5 is free to move and pulled left by the redistributed stress as the mining face advances. In the fifth stage, the shear displacement becomes negative and increases in magnitude, which indicates that the shear movement shown in Fig. 3-38e has occurred

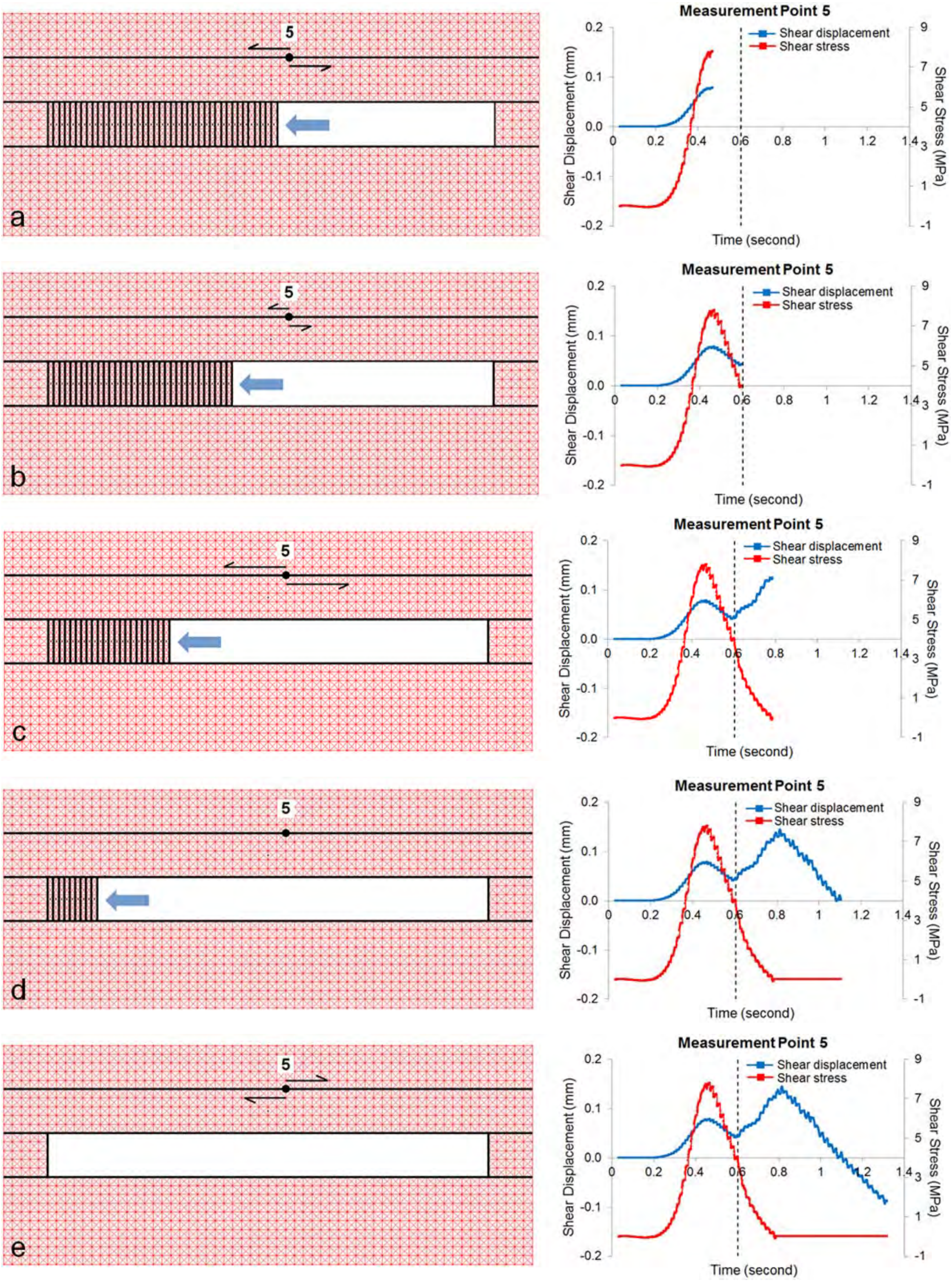

Fig. 3-38 Shear stress–time plot of the measurement point 5.

.

Semi-stable failure

Fig. 3-39 shows the shear displacement–time and shear stress–time plots of measurement point 7. Point 7, like point 5, exhibits two peaks in its shear displacement records. The pre-failure regime is similar to that of point 5. In the post-failure regime, however, there are rapid, discontinuous increases in the shear displacement. These are indicated by the sparse data points, implying the initiation of failure at the point has been less stable.

Similar signatures of the failure at point 7 are observed in the shear stress–time plot in Fig. 3-39, also suggesting the failure is not completely stable. Hence, the shear failure at point 7 is considered to be a semi-stable failure.

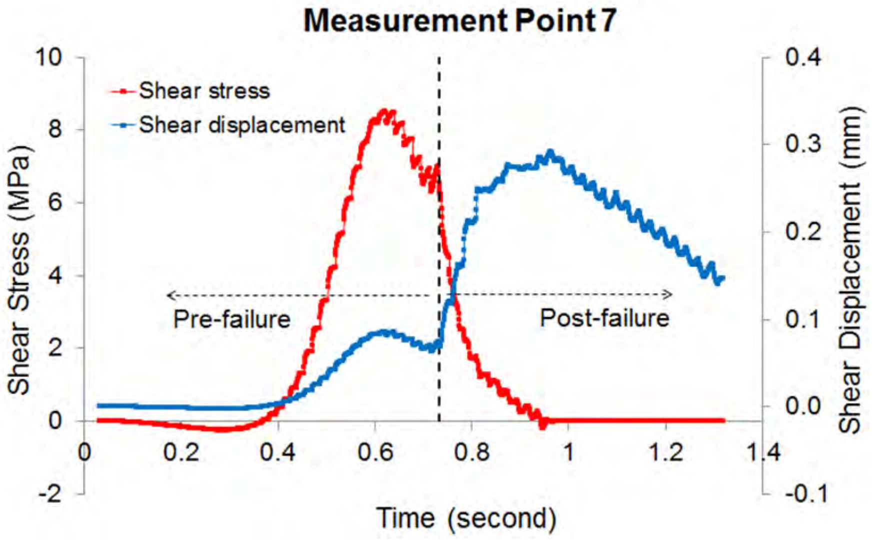

Fig. 3-39 Shear displacement–time and shear stress–time plots of measurement point 7.

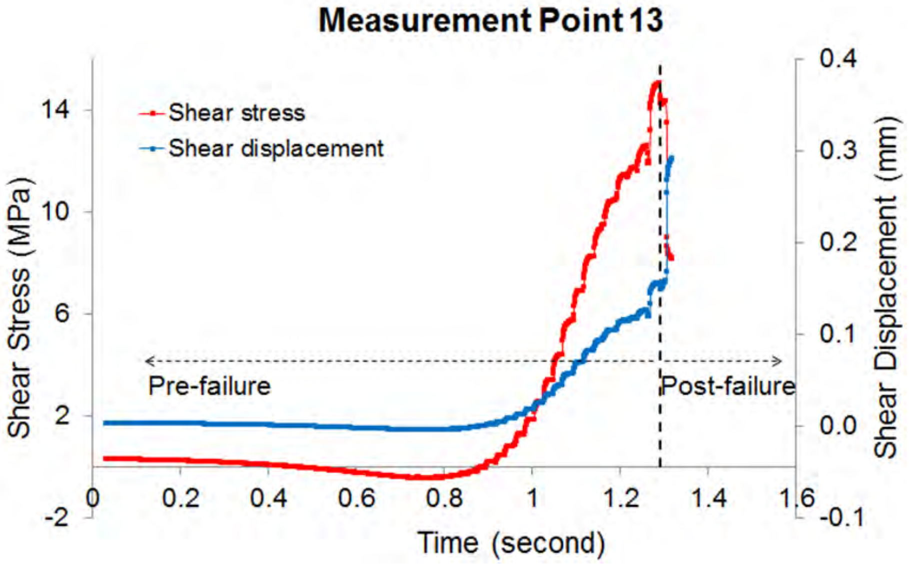

Fig. 3-40 Shear displacement–time and shear stress–time plots of measurement point 13.

Unstable failure

The shear displacement–time and shear stress–time plots of point 13 are shown in Figs. 3.40. There is a small but rapid increase in shear displacement as well as in shear stress in the pre-failure regime. This is caused by the unstable failures at the contact points located at the right side of point 13 on the discontinuity. In the post-failure regime, a large, rapid increase in shear displacement and a decrease in shear stress—along with sparse data points—signify the shear failure at point 13 is unstable. Point 13 regains equilibrium after the unstable failure process. The equilibrium state is indicated by the gradual changes in shear displacement and shear stress with dense data points in the post-failure region.

Analyses of loading stiffness

At a given point along the discontinuity, the loading stiffness plays a significant role in governing the stability of shear failures of rock discontinuities. The greater the loading stiffness, the smaller the probability of unstable failures becomes. Loading stiffness is affected by the extent of the excavated area, the location of the point being considered on the discontinuity, the location of the discontinuity relative to the excavation and the elastic modulus of the surrounding rock. The following sections discuss the results of a series of simulations performed to study the influence of these factors on loading stiffness.

The model configuration used for analyzing the effects of geometry and elastic modulus on loading stiffness is shown in Fig. 3-41. The extent of the excavated area is represented by d in the figure. To investigate the effect of the excavation extent, six different values of d (0, 4, 8, 12, 16 and 20 m] were used in six loading stiffness tests. The measurement point for these tests is Pd. To study the influence of the distance between the excavation roof and discontinuity, the excavation area was fully excavated and the discontinuity location was changed. The distance between the excavation roof and the discontinuity is represented by h in Fig. 3-41. Eight different values of h were used at 1 m increments, beginning at 1 m and ending at 8 m. The measurement point for the tests is Ph, which is at the center of the discontinuity. An elastic modulus of 50 GPa was assigned to the rock.

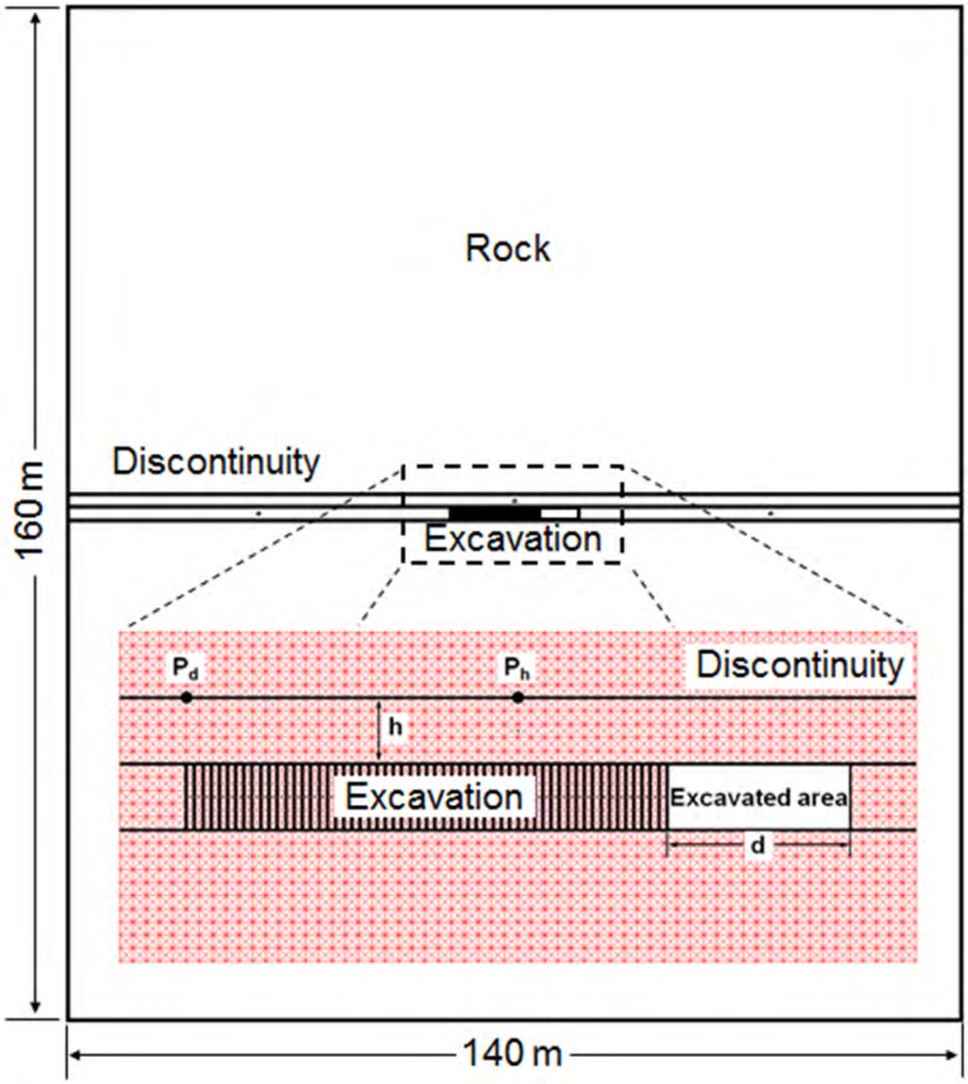

Fig. 3-41 Configuration of the loading stiffness tests to study the effects of the factors.

Effect of excavation extent

The results of the test for determining the effect of the excavated extent d on the loading stiffness of point P_d are shown in Fig. 3-42 as the blue curve. The loading stiffness at the point decreases as the excavation extent increases. Up to 4 m, the extent has no effect on the loading stiffness at the point. As the extent increases beyond 4 m, excavation starts affecting loading stiffness. The effect of an extensive excavated area becomes significantly larger when the excavation face is close to the measurement point. The change in the loading stiffness from the first test of d = 0 m to the last test of d = 20 m is 6.3 GPa/m. This result suggests that the extent of mining largely affects loading stiffness, which can affect the stability of failures of rock discontinuities.

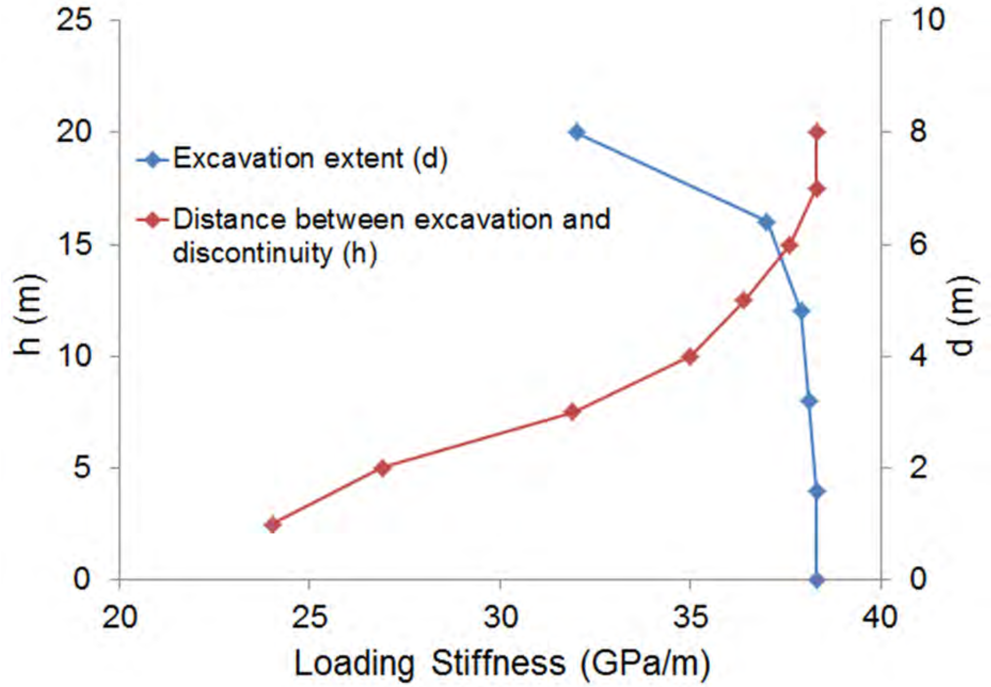

Fig. 3-42 Effects of the excavation extent (d) and distance between the excavation and discontinuity (h) on the loading stiffness of point Pd.

Effect of discontinuity plane location

The effect of discontinuity plane distance to mining level h on the loading stiffness at point P_h is shown also in Fig. 3-42 as the red curve. The loading stiffness at P_h increases as h becomes larger. At the completed excavation geometry of 20 m, the loading stiffness at P_h increases to a constant value when the distance between the excavation roof and the discontinuity reaches 7 m. Beyond this distance, the fully excavated area has no influence on the loading stiffness at the point. The loading stiffness at P_h increases 14.3 GPa/m as h increases from 1 m to 8 m. Although only one point, P_h, is used, the trend of loading stiffness changing with increasing distance is expected to be similar along the discontinuity. Based on the results shown in Fig. 3-42, it can be deduced that a larger distance h results in a smaller possibility of unstable shear failures of a rock discontinuity.

Effect of rock elastic modulus

To demonstrate the effect of the rock elastic modulus on the stability of rock discontinuities, the discontinuity stability test run was repeated with an elastic modulus of 50 GPa assigned to the rock. The shear stress–time plots of all measurement points are shown in Fig. 3-43. Compared to Fig. 3-36, which shows shear stress–time plots for elastic modulus of 70 GPa case, more unstable failures are observed at the points, and the intensity of unstable failures is larger.

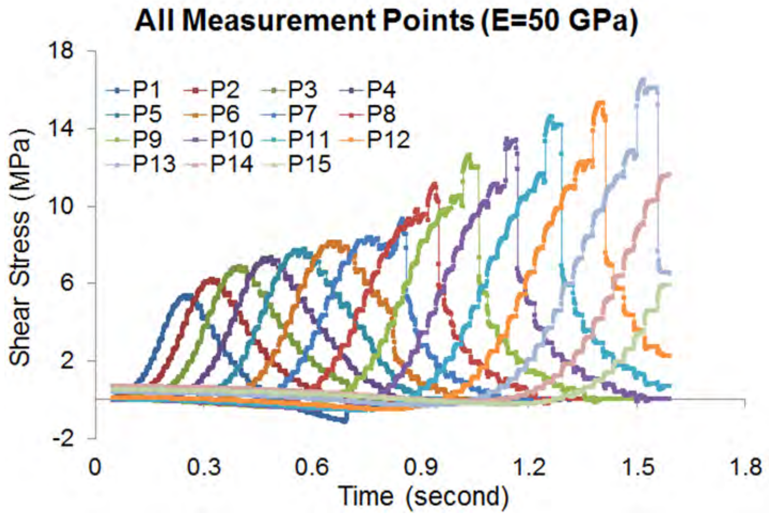

Fig. 3-43 Shear stress–time plots of all measurement points in the test with the elastic modulus of 50 GPa applied in the rock.

Effect of in situ stress field

To study the effect of in situ stress field on the discontinuity failure stability, the simulation with 50 GPa modulus was repeated after rotating the stress field 45° towards right. As seen from the results in Fig. 3-44, all shear failures on the discontinuity are unstable failures, and the intensities of these failures as defined by the size of the rapid shear stress drops are significantly larger than that in the un-rotated stress field case in Fig. 3-36. Clearly, the in situ stress field can have significant effect on the failure stability of the existing rock discontinuity and needs to be investigated in detail for rockburst-prone mining conditions.

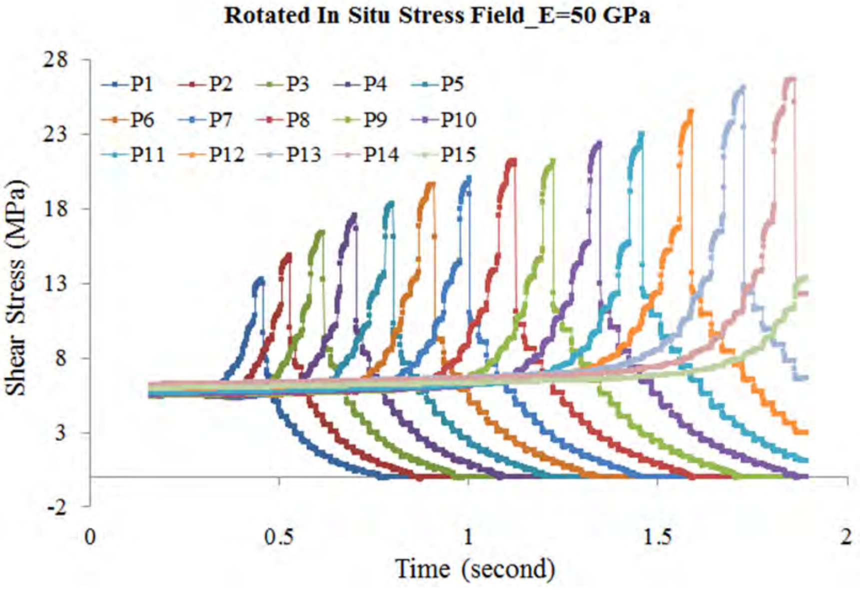

Fig. 3-44 Shear stress–time plots of all measurement points in the discontinuity stability analysis with an elastic modulus of 50 GPa in the rock mass and a rotated in situ stress field.

Compressive failure stability model validation

The capability of UDEC in modeling failure stability is investigated using the case of UCS test. According to Cook's failure stability criterion [13], during compressive loading, unstable failure in rock occurs if the loading system stiffness is softer than the post-peak stiffness of the rock. As such, for modeling failure stability, the constitutive law used in the numerical model needs to have the ability to model softening in rock's post-peak regime. In this this study, the Mohr-Coulomb strain softening (MCSS) constitutive model as incorporated into UDEC is used. The input parameters for of MCSS model are given in Table 3-5.

Table 3-5 Input parameter tables of the MCSS model for the rock specimen.

Cohesion (2nd column), MPa plastic strain (1nd column)	0.00000, 2.2
	0.00005, 2.2
	0.03600, 0.2
Friction angle (2nd column) plastic strain (1st column), degree	0.00000, 23.0
	0.00002, 30.0
	0.00780, 30.0
Dilation angle (2nd column) plastic strain, (1st column), degree	0.0000, 15.0
	0.0005, 15.0
	0.0010, 5.0
	0.0015, 5.0

The UDEC model constructed for the UCS simulations is shown in Fig. 3-45. The rock specimen is placed between two loading platens that represent the testing machine as shown in Fig. 3-45a. Two tests were performed to show the ability of UDEC in simulating stable and unstable compressive failures. Only the platen modulus was changed between the simulations. As the soft loading system, the platens were assigned an elastic modulus of 1 GPa and for the stiff loading system platens elastic modulus was set at 50 GPa. All the other properties were kept the same among the two tests. The vertical loading is applied by applying constant velocities over the free ends of the platens.

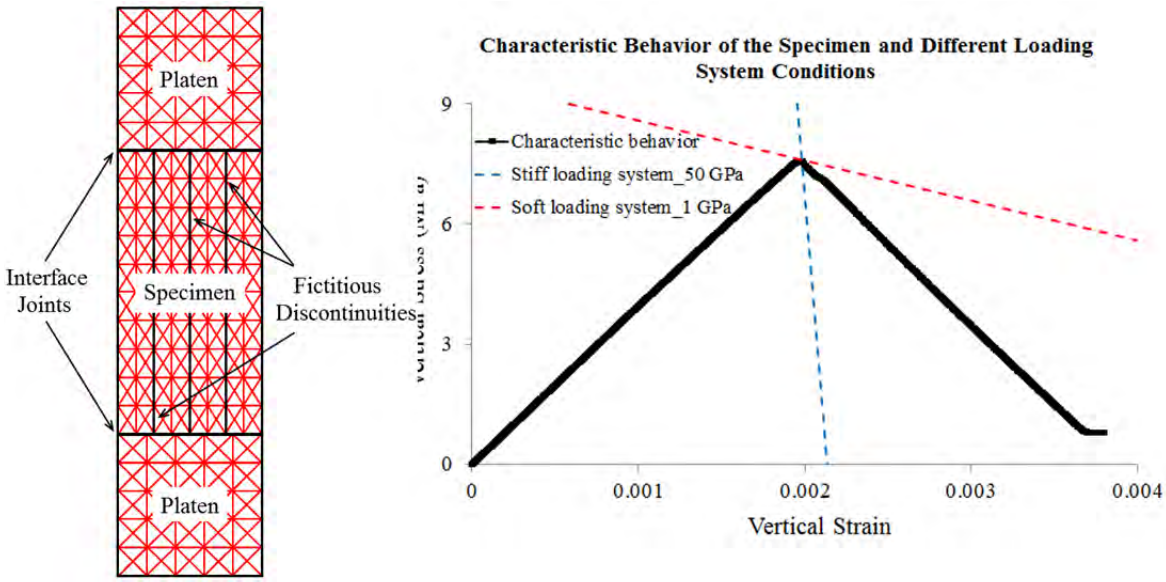

(a) (b)

Fig. 3-45 Compressive failure analysis: (a) UDEC model of UCS test setup, and (b) characteristic stress-strain behavior of the rock specimen obtained from the UDEC simulations.

Fig. 3-46 shows the results of the UCS tests under the stiff and soft loading system conditions. The red line shows the vertical stress–time plot from the test with the soft platen setting while the blue line represents the results of the stiff platen testing. The stability of failure can be distinguished by analyzing the vertical stress–time plots. The sudden stress drop in the red line indicates an unstable failure as the reduction of the specimen strength occurs rapidly in the failure process. The blue line in the post-peak regime indicates a stable failure as the vertical stress decreases in a gradual and continuous manner. These results show that UDEC with the MCSS model is capable of simulating stable and unstable compressive failures of rock materials.

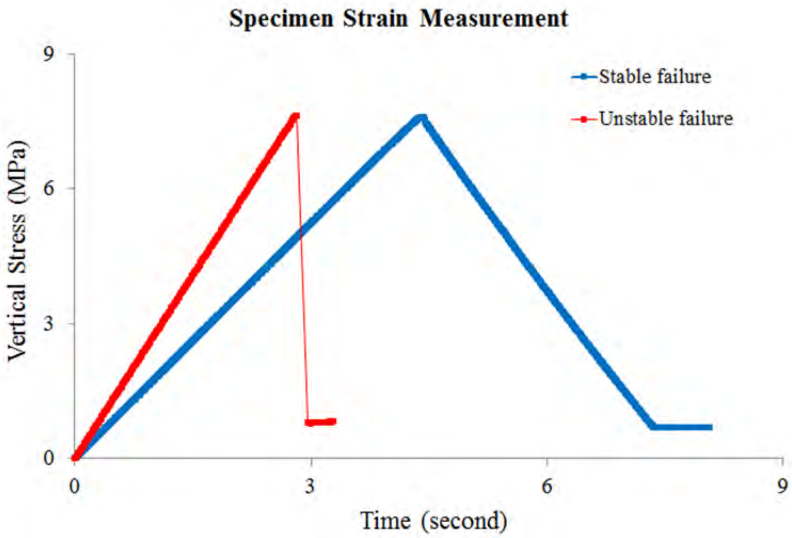

Fig. 3-46 Specimen vertical stress-time plots in different loading system conditions.

Unstable compressive failure and de-confinement mechanisms

Despite the developments in understanding of the mechanisms of failures in certain conditions, compressive failures of mining faces, sidewalls and pillars with large width-to-height ratios still require further studies. The resistance provided by the roof-coal and coal-floor interfaces is one of the important factors that impact the strength and failure stability of excavation walls. In this section, taking into consideration the mechanical behaviors of the interfaces, a de-confinement mechanism is forwarded to use for the analyses of unstable compressive failures of sidewalls in coal mines. The emphasis is placed on the de-confinements effects resulting from unstable shear failures of interfaces (Fig. 3-47a) and the existence of weak contact regions at the interfaces (Fig. 3-47b).

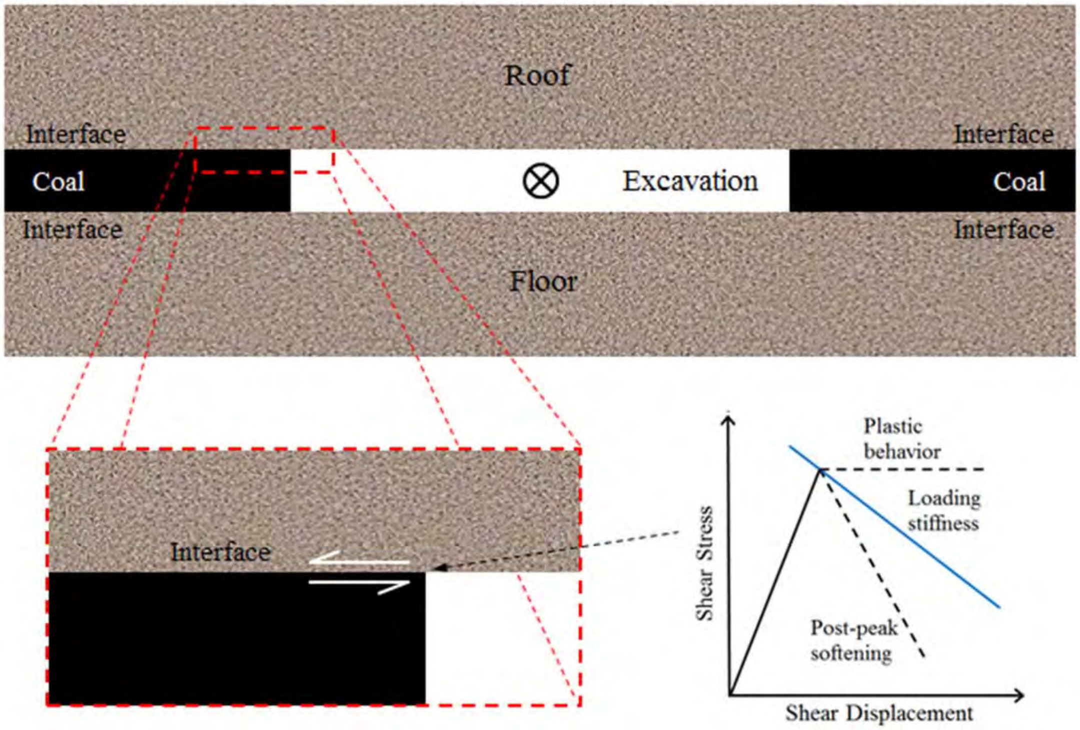

Fig. 3-47a Mining geometries used for modeling of de-confinement induced unstable compressive failures in mining faces and sidewalls. Mining advances perpendicular to the plane causing shear stress increase at the side abutments.

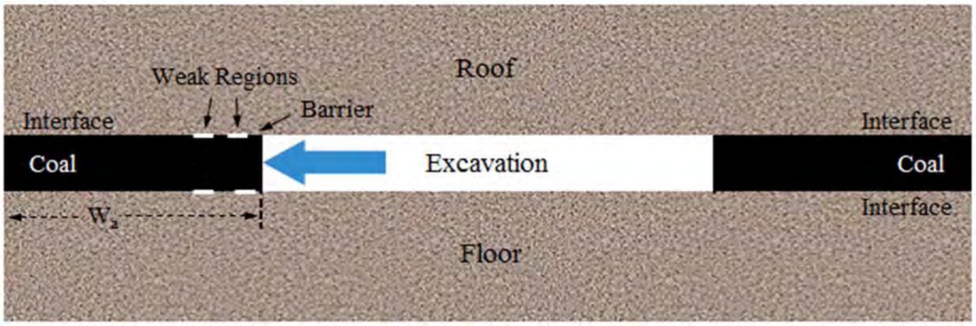

Fig. 3.47b The concept of weak region induced discontinuity failures. Unstable compressive failures of sidewalls can be triggered on the weak regions along the interfaces. Mining first advances left as shown by the blue arrow, and then moves perpendicular to the plane.

When the interfaces at the top and bottom of the coal seam are modeled to exhibit elastic-plastic behavior, the possibility of unstable failure on the interface is inherently ignored. Potential compressive unstable coal seam failures would also be inaccurately modeled under plastic interface shear failures. To study the de-confinement of sidewalls, two simulations were performed: one with the MC plastic joint model and the other with the CY joint model at the interfaces. In both cases, the coal seam is modeled as a MCSS material with the same input parameters as those in Table 3-2. The model geometry for the de-confinement analysis of the sidewalls is shown in Fig. 3-48. A constant velocity is applied at the top and bottom of the model to simulate mining advancing perpendicular to the plane. Six measurement regions in the coal seam (i.e., C1 to C6) are chosen to record normal stress in the simulation.

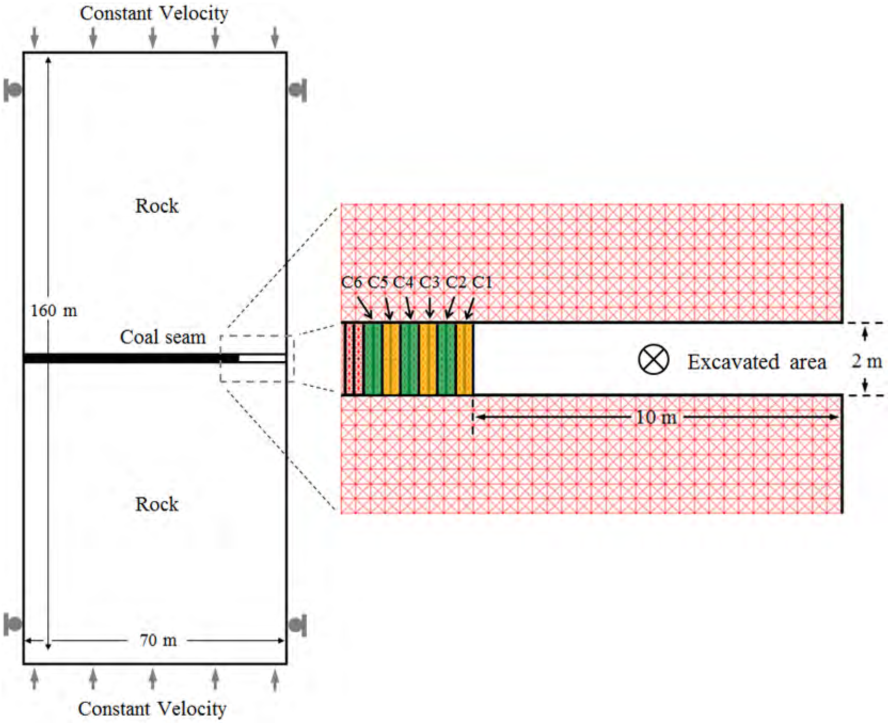

Fig. 3-48 Model for studies of de-confinement mechanisms involving unstable shear failures for the stability of sidewalls.

The MC interfaces result in only stable shear failures as shown in Fig.3.49, which lead to stable compressive failures in the sidewalls as indicated by the gradual, continuous changes in the normal stress. The CY joint model simulated interfaces experience unstable shear failures, which cause unstable compressive failures in the sidewalls as shown by the rapid, discontinuous decreases in the normal stress along with sparse data in Fig. 3-50.

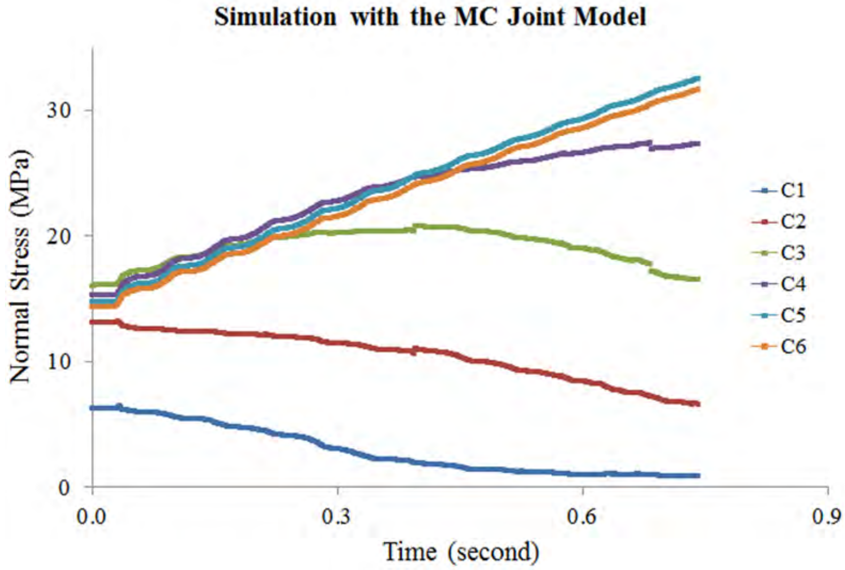

Fig. 3-49 Normal stress-time curves of the measurement regions in the simulation with the MC model.

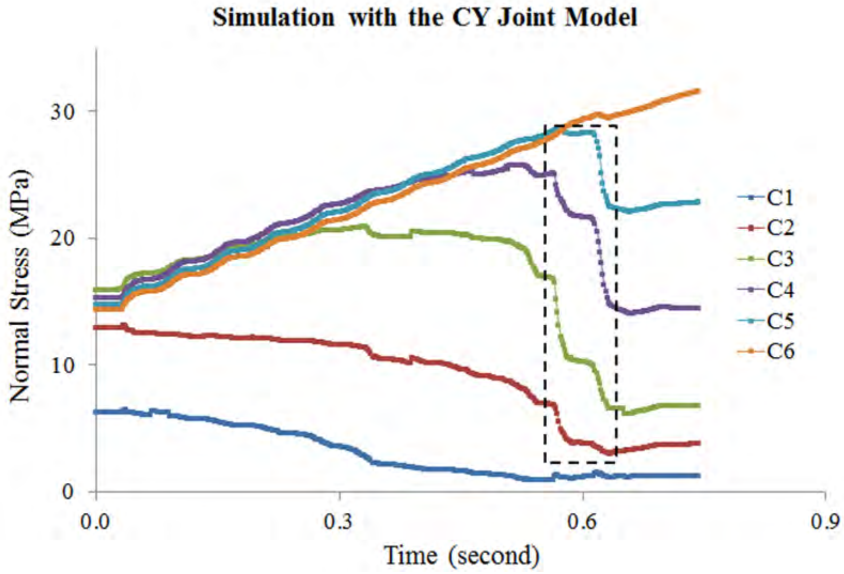

Fig. 3-50 Normal stress-time curves of the measurement regions in the simulation with the CY model.

The interfaces between different rock materials sometimes include weak regions due to weak infillings or reduced waviness or roughness. The failure of such weak regions may contribute to the formation and magnitude of unstable compressive failures in the coal seam. The effect of weak regions on creating unstable sidewall or mining face failures is analyzed using the model described in Fig. 3-51. The excavation advances in the direction indicated by the white arrow until it achieves 10 m in length. The white and red lines on the interfaces represent weak regions and the contact region with high strength between the weak region and the opening area, which will be referred as barriers.

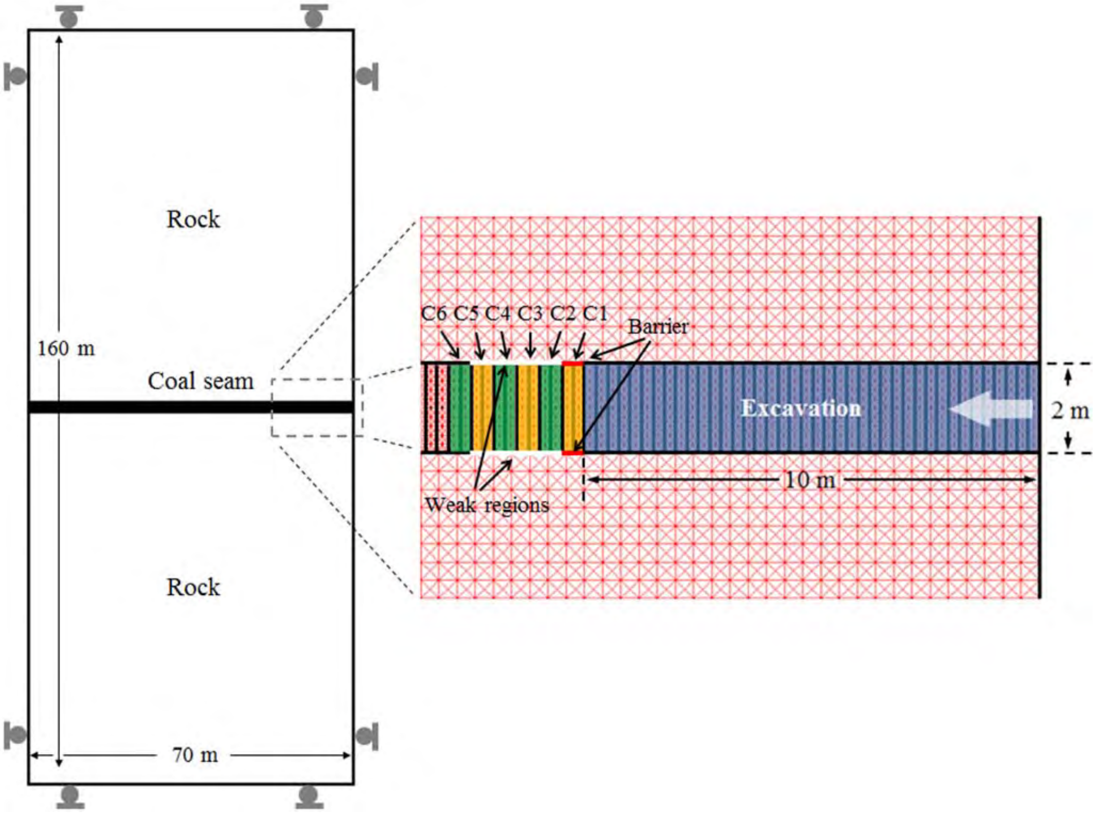

Fig. 3-51 Model for studies of de-confinement mechanisms involving weak regions for the stability of mining faces.

The results from the numerical simulations indicate that the stability and intensity of the failures at mining faces are largely affected by the presence of weak regions along the roof-coal and coal-floor interfaces. The normal stress records from a simulation with a weak region length of 2.0 m and a barrier length of 0.5 m are shown in Fig. 3-52 and 3.53. Comparing the results given in these figures, it can be seen that when there are weak regions present along the interface (Fig. 3-52), more unstable compressive failures can occur and the magnitude of these failures are larger than those in the case of no weak regions on interfaces (Fig. 3-53). Increased sections of coal material tend to fail over a short time period and they fail earlier than the ones in the simulation with no weak region.

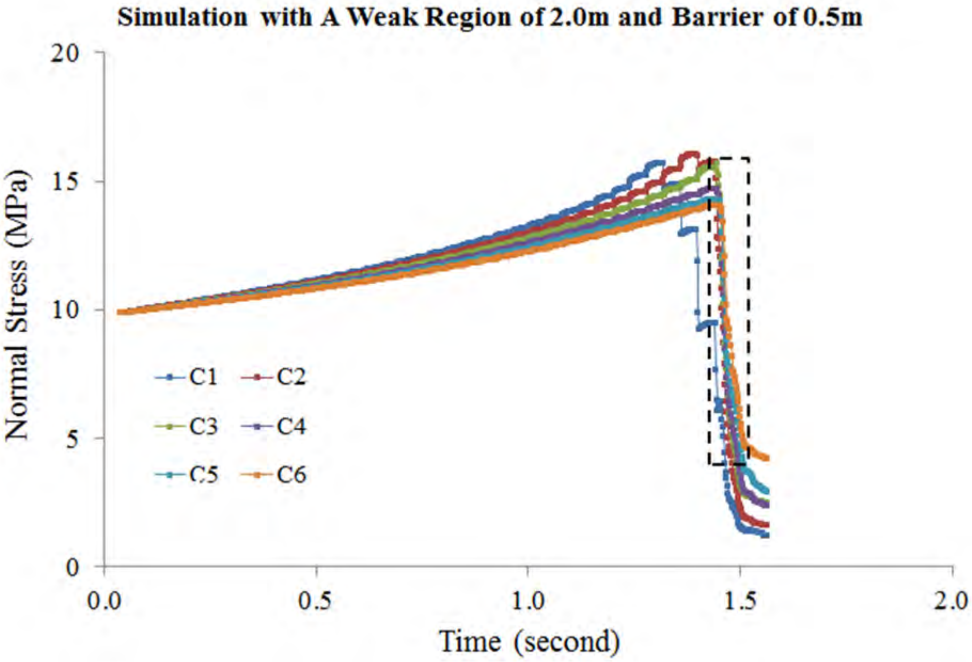

Fig. 3-52 Normal stress-time curves of the measurement regions in the simulation with a weak region of 2.0 m and a barrier of 0.5 m.

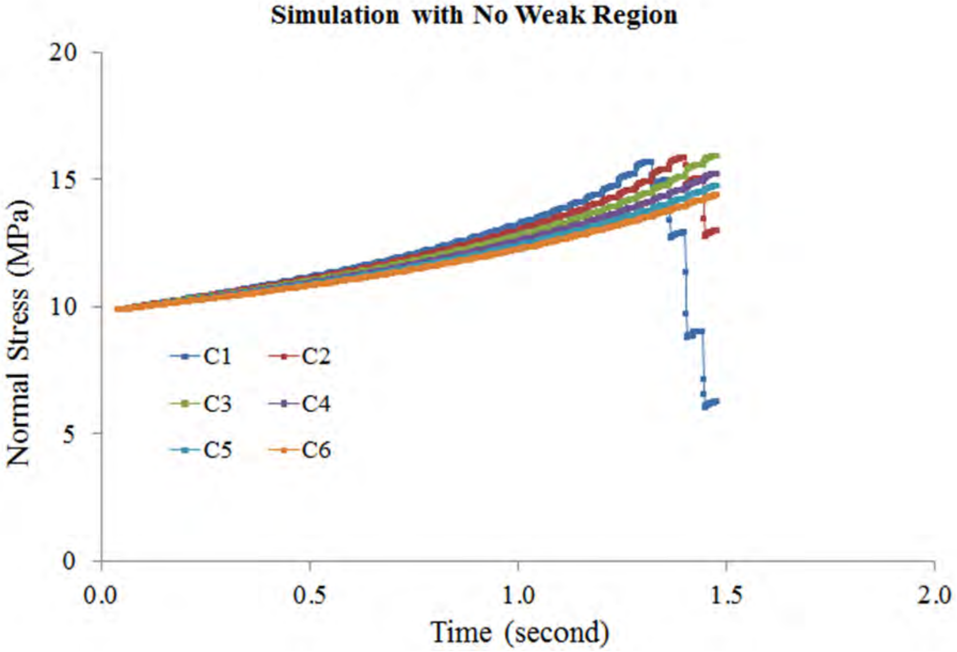

Fig. 3-53 Normal stress-time curves of the measurement regions in the simulation without weak region.

PFC analysis of compressive failure stability

This section describes the Discrete Element Method (DEM) modeling studies that are carried out to study failure stabilities in deep coal mine settings. As the modeling software, a DEM based program Particle Flow Code (PFC) by Itasca [28] is used. First, the suitability of PFC in modeling failure stability is studied. FLAC-PFC coupled models were then developed to save run times during simulations of laboratory UCS tests, pillars failure stabilities, and failure stabilities during mining face advances. Five stability identifiers are used to assess the failure stabilities, these are damping work, kinetic energy, mean unbalanced force, maximum unbalanced force, contact softening, and the number of broken contacts. A spatial distribution of the damping work and contact softening is also considered for each of the tests to determine the relationship between the spatial distribution of damage in the model and unstable failure.

Calibration of PFC models up to the point of failure is frequently done, but calibrating post-peak modulus is not. In its current form, it is difficult to achieve the desired post-peak modulus. In this study, material properties are calibrated using a specifically developed genetic algorithm described in [19]. A set of microparameters that results in the desired elastic modulus, Poisson's ratio, compressive strength, and post-peak modulus are used to generate the model material. Biaxial confinement tests are then conducted to determine the internal friction angle of the material. The model is calibrated to represent large scale properties of coal. Table 3-6 shows the set of microparameters as determined by the genetic algorithm and resulting macroscopic behavior.

Failure stability modeling in DEM

The ability of the DEM in PFC3D to simulate unstable failure was demonstrated previously in Chapter 2. These prior results are characterized in Fig. 3-54, showing stable and unstable failures in PFC3D. For 10 GPa and 100 GPa loading systems the measured post peak behavior assumes that of the characteristic material behavior. According to the equilibrium stability concept, when the loading system stiffness decreases below the post-peak stiffness of the material, the failure is unstable. In the 1.5 GPa case, when the failure is unstable the material suddenly loses load bearing capacity and, during the failure, the specimen strain shows the sudden rebound of the loading system. Consequently, as seen in Fig. 3-54, the post-peak behavior of the material appears to change to the stiffness of the loading system.

The simulations developed for failure stability are repeated using a two dimensional model in which the elastic platens are modeled using FLAC [27] and the coal material is modeled using PFC [28]. The two models are mechanically coupled at the top and bottom boundaries. The reaction forces on the PFC boundary particles are used to compute forces to be applied to FLAC grid points on the coupling boundary. After a calculation cycle in FLAC, grid point velocities at the coupling boundary are used to apply velocities to the PFC boundary particles. Constant velocity boundary conditions are applied to the outermost FLAC grid points. Vertical stress is recorded from FLAC zones and averaged across the width of the platen, and then averaged using top and bottom platen averages. Displacements of grid points at the coupling boundaries are used to calculate the specimen strain. The stiffness of the loading system and the specimen post-peak stiffness are calculated and compared to determine whether the failure is stable or unstable.

Table 3-6 Bonded particle model microparameters and material macroproperties.

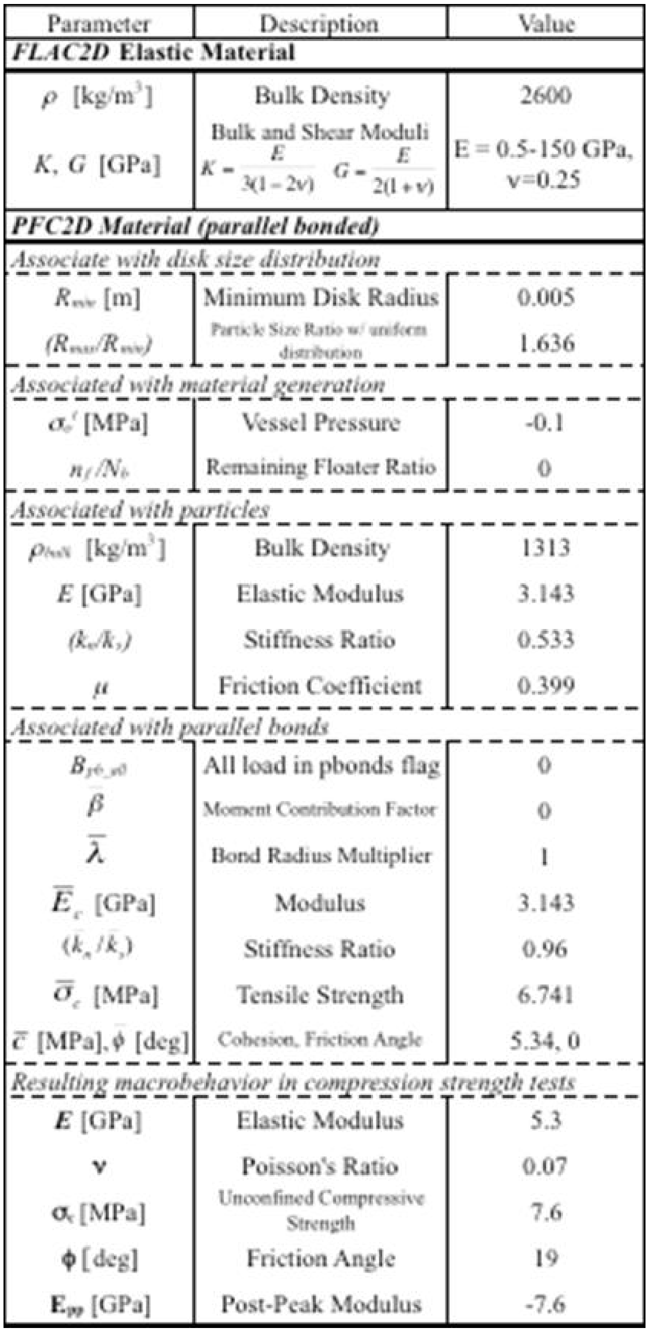

Parameter	Description	Value
***FLAC2D* Elastic Material**		
ρ [kg/m^3]	Bulk Density	2600
K, G [GPa]	Bulk and Shear Moduli $K = \frac{E}{3(1-2\nu)}$ $G = \frac{E}{2(1+\nu)}$	E = 0.5-150 GPa, ν=0.25
PFC2D Material (parallel bonded)		
Associate with disk size distribution		
R_{min} [m]	Minimum Disk Radius	0.005
(R_{max}/R_{min})	Particle Size Ratio w/ uniform distribution	1.636
Associated with material generation		
σ_0^f [MPa]	Vessel Pressure	-0.1
n_f/N_b	Remaining Floater Ratio	0
Associated with particles		
ρ_{ball} [kg/m^3]	Bulk Density	1313
E [GPa]	Elastic Modulus	3.143
(k_n/k_s)	Stiffness Ratio	0.533
μ	Friction Coefficient	0.399
Associated with parallel bonds		
B_{pb_pd}	All load in pbonds flag	0
$\bar{\beta}$	Moment Contribution Factor	0
$\bar{\lambda}$	Bond Radius Multiplier	1
$\bar{E}_c$ [GPa]	Modulus	3.143
$(\bar{k}_n/\bar{k}_s)$	Stiffness Ratio	0.96
$\bar{\sigma}_c$ [MPa]	Tensile Strength	6.741
$\bar{c}$ [MPa], $\bar{\phi}$ [deg]	Cohesion, Friction Angle	5.34, 0
Resulting macrobehavior in compression strength tests		
E [GPa]	Elastic Modulus	5.3
ν	Poisson's Ratio	0.07
σ_c [MPa]	Unconfined Compressive Strength	7.6
ϕ [deg]	Friction Angle	19
E_{pp} [GPa]	Post-Peak Modulus	-7.6

Evaluation of two different DEM for modeling failure stability

In PFC, two different particle bonds and contact models are available for selection, each having unique behavior during loading and failure. These two different models are evaluated to determine the better candidate for modeling unstable failure under compressive loading. The two models are the standard bonded particle model as described in [28,19] and the displacement-softening contact model described in [28].

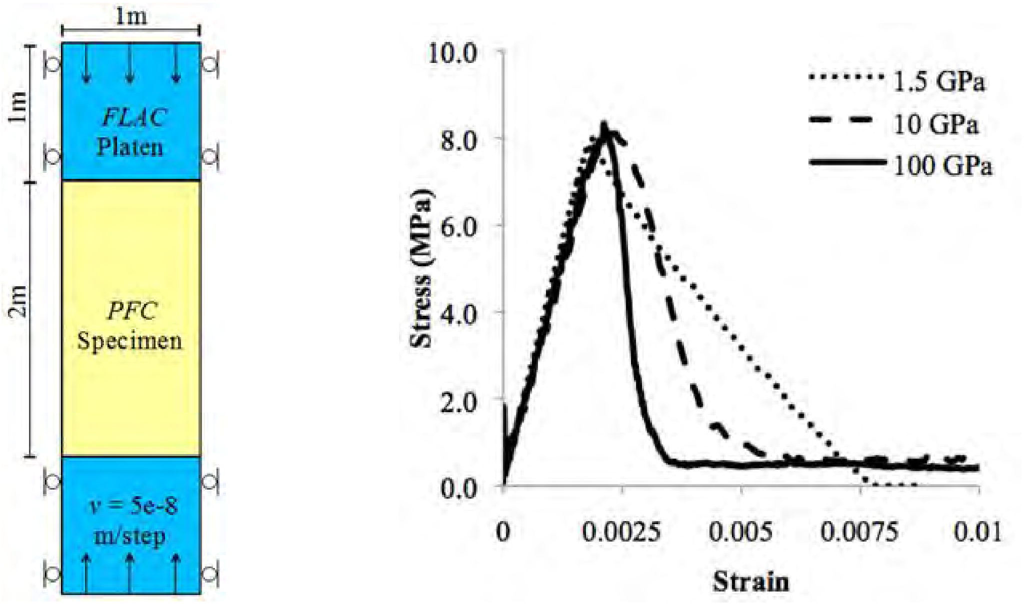

Fig. 3-54 FLAC-PFC coupled UCS model Elastic Platen Strength (EPS) test set up and results.

Both models tested in this study use an identical particle arrangement. Only the particle contact model and bonding method are different. The compression specimen is an assemblage of two square "bricks" that are created using the material generation procedure as described in [28]. This generation procedure uses periodic boundaries to assure that the bricks fit together seamlessly.

Both models are calibrated in UCS tests. The bonded particle model utilizes a linear contact model and is bonded using a parallel bond. The contact and bond parameters are calibrated using a computer aided calibration scheme described in [19]. The displacement softening model (DSM) uses a contact model that varies contact stiffness based on distance between particle centroids. Aside from this contact model, no additional bonding is present. The contact parameters are calibrated manually using an iterative calibration process.

The target behavior of the models can be described as a generic western US coal. Critical to the calibration is the ability to achieve a softening post-peak behavior approximately equal in magnitude to the elastic modulus. Table 3-7 shows the target UCS behavior for calibration and the achieved behavior for both models. The degree to which the models match the target reflect the difficulty in achieving a reasonable post-peak softening characteristic. Future work is needed to improve the calibration.

Table 3-7. Target and model characteristic behavior

	Target	D. S. Model	B. P. Model
E (GPa)	4.0	6.0	5.3
ν	0.2	0.4	0.1
σ_c (MPa)	7.6	8.7	7.7
E_{pp} (GPa)	4.0	3.0	7.9

A uniaxial compression test is used during calibration to determine the full stress-strain curve of each material. The test is displacement controlled, increasing the load monotonically via a constant velocity boundary condition at the top and bottom edges of the sample. In order to apply the velocity boundary condition, a series of grip particles on the top and bottom edges are assigned a constant vertical velocity and fixed in the horizontal direction. The test is run until the vertical stress in the softening region is less than half of the strength.

Fig. 3-55 shows the stress strain curves for the bonded particle specimen and the displacement-softening specimen. The curves show that both materials have a softening post-peak behavior. The post-peak modulus in both cases is similar in magnitude to the elastic modulus of the material.

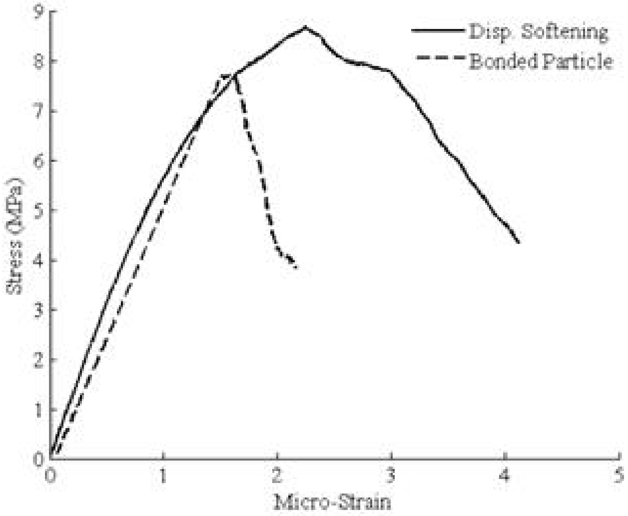

Fig. 3-55 Stress-strain curves from unconfined compression tests.

The internal friction angle of rock simulated by DEM is an emergent property rather than an assigned one. So, the friction angle must be determined by failing the material under various levels of confinement. Confinement is provided using a particle membrane. Four tests are conducted on each model. Fig. 3-56 shows the results of each test in terms of internal shear strength and normal stress. The internal friction angle is the slope of the linear interpolation of the data and is shown for each model. The results indicate that the friction angle of the bonded particle material is below the target value selected as 30˚ for coal. The displacement-softening material, on the other hand, has a friction angle higher than the desired friction angle. Variation from the desired friction angle will lead to lower or higher strength under confinement respectively.

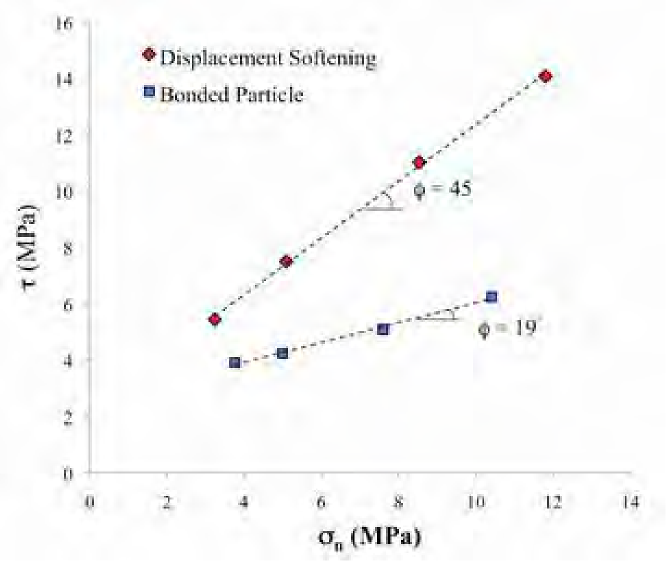

Fig. 3-56 Confined compression test results.

The velocity boundary condition is varied to determine the effect of loading rate on material properties. Uniaxial compression tests are performed on each material using four different loading velocities. The chosen velocities include the velocity used during the previous tests, 6.0e-5 m/s, and values that are both lower and higher in magnitude. Fig. 3-57a shows that, in the bonded particle model, as the loading velocity decrease the post-peak modulus increases in magnitude. While in the displacement-softening case in Fig. 3-57b, post-peak softening behavior persists despite the change in velocity.

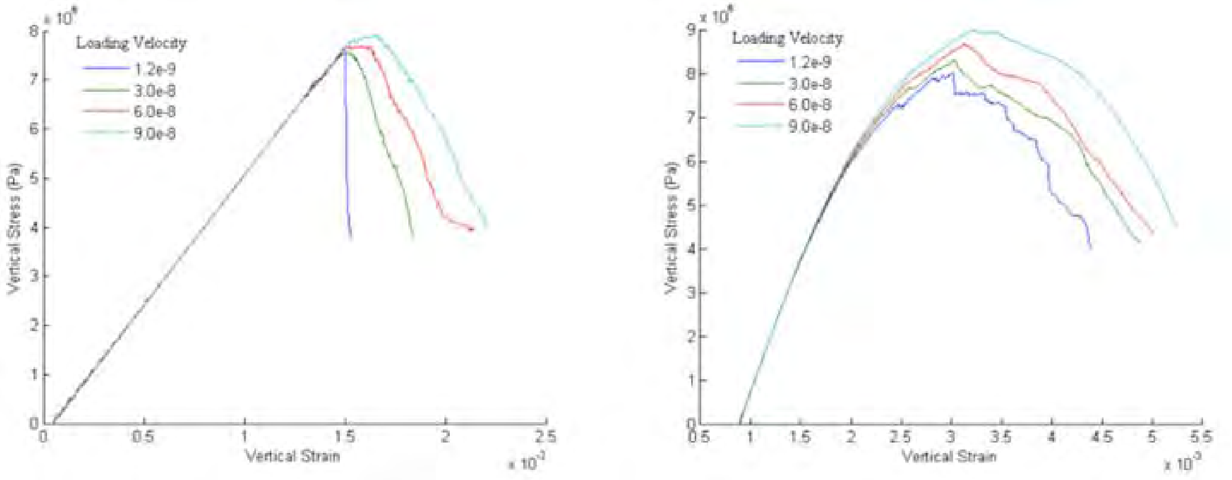

(a) (b)

Fig. 3-57 Variable loading velocity results.

The loading velocity variability tests revealed different post-peak behaviors for the two models. Fig. 3-57a shows that, with changes in the loading velocity, the bonded particle model will vary in its post-peak modulus. Such velocity dependence of the post-peak behavior presents complexities in modeling of loading during mining advances. The mining induced loading velocity is likely to vary spatially and can be difficult to determine in practice. The displacement-softening model with its consistent post-peak characteristic appears better suited for unstable failure studies in underground mining situations.

It appears that both the displacement-softening contact model and the bonded particle model can produce softening post-peak behavior. The bonded particle model shows a large change in post-peak softening characteristic as loading velocity decreases while post-peak softening in the displacement-softening model remains fairly constant. The latter can help to prevent inherent ambiguity in the stability of failure, thus is selected for modeling failure stabilities in underground mining conditions. Based on this conclusion, the displacement-softening was selected for the failure stability analysis.

Failure stability studies using coupled UCS test

Fig. 3-58 shows UCS model test results using the FLAC-PFC model (Fig. 3-54). The platen stiffness in these tests varied from 0.5 GPa to 50 GPa. Also included is a test with infinitely rigid loading condition intended to reveal the coal's characteristic material behavior. The rigid test is simulated by loading the specimen by applying a velocity boundary condition directly to the PFC boundary particles with no elastic platens present.

The results are plotted as average vertical stress – strain curves in Fig. 3-58. In the post-peak region, the plots show four lines deviating from remaining cluster of curves. The "Grip UCS" curve depicts the characteristic behavior of the coal. As the 0.5-5 GPa specimens fail, the post-peak behavior changes to reflect the rebounding platen rather than the characteristic behavior of the coal. The deviation from the characteristic behavior suggests unstable failure of the specimen.

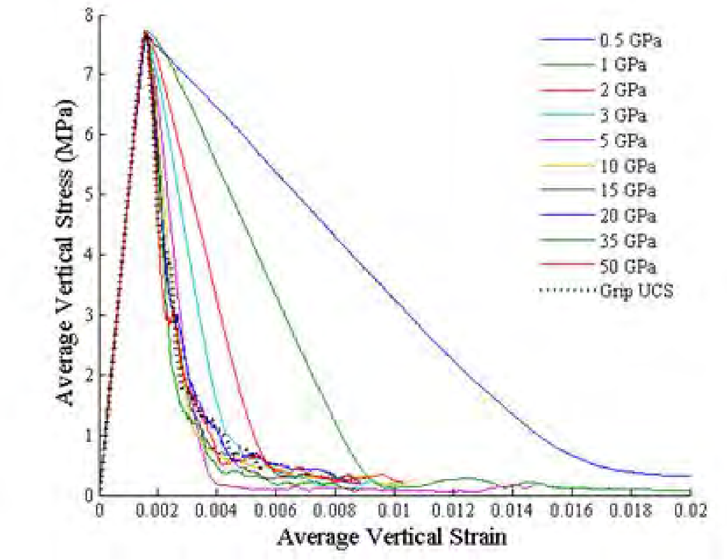

Fig. 3-58 Specimen stress-strain curves for FLAC-PFC coupled UCS tests.

Calculating the post-peak stiffness provides an additional tool as indication of stability. Fig. 3-59a and Fig. 3-59b show scatter plots of loading system stiffness and post-peak stiffness. The stiffness is calculated using a form of the equation for elastic beam axial displacement.

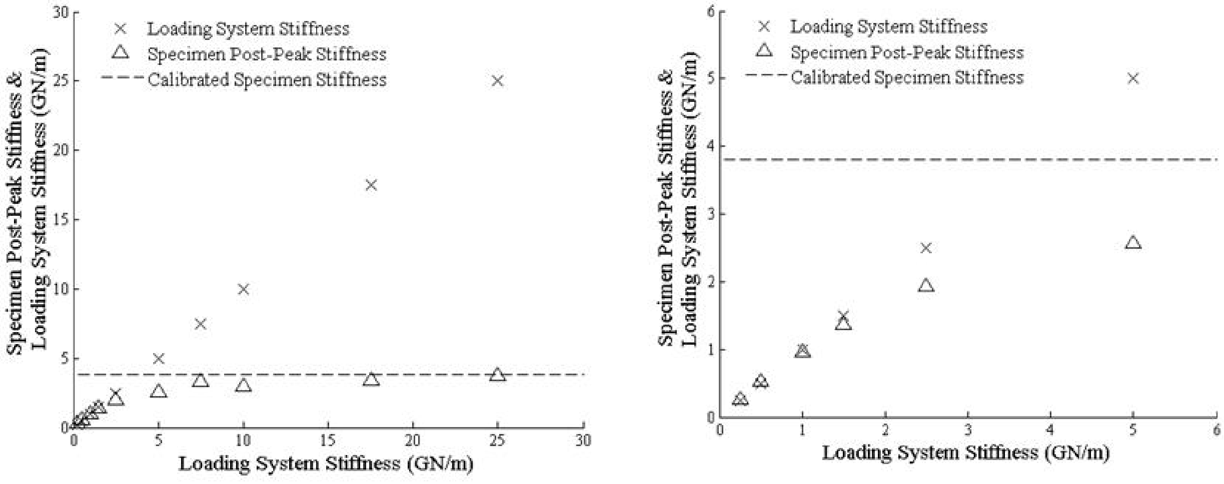

(a) (b)

Fig. 3-59 Loading system stiffness and specimen post-peak stiffness versus loading system stiffness for FLAC-PFC coupled UCS tests.

The horizontal dashed line indicates the post-peak stiffness of the coal under rigid loading conditions with the calibrated material behavior. For tests in which the loading system stiffness is less than this value, the measured post-peak stiffness is equal to the loading system stiffness. Fig. 3-59a shows all of the ten UCS tests. As loading system stiffness increases, the post-peak stiffness assumes that of the characteristic behavior. Fig. 3-59b shows more closely the tests with platen modulus below 10 GPa. As the stiffness increases, the specimen post-peak stiffness diverges from the loading system stiffness and approaches the characteristic post-peak stiffness.

Indicators of unstable compressive failures

Various measurements of DEM behaviors can be used to indicate whether failure is stable or unstable and give a measure of the degree of failure instability. Five stability identifiers used in the DEM studies, namely damping work, kinetic energy, unbalanced force, contact softening, and number of broken contacts. These identifiers are applied to the laboratory elastic platen strength (EPS) tests, mine pillars, and mining advances.

Stability identifiers in EPS tests

For the EPS tests, the spatial distribution of the damping work and contact softening is observed for each of the tests to determine the relationship between the damage in the model and unstable failure. The trends of indicators are shown by means of scatter plots of the indicator values versus elastic modulus of the platens used in the test. Values of indicators are determined from line plots of the indicator.

For some of the stability identifiers, a conceptual plot was used to illustrate the behavior in the post-peak regime of the failures. A generic form of this illustration is shown in Fig. 3-60. The section between the two dashed lines is the failure interval. The bold line in the figure represents the particular identifier behavior and the interval defined by dT in the example is time step.

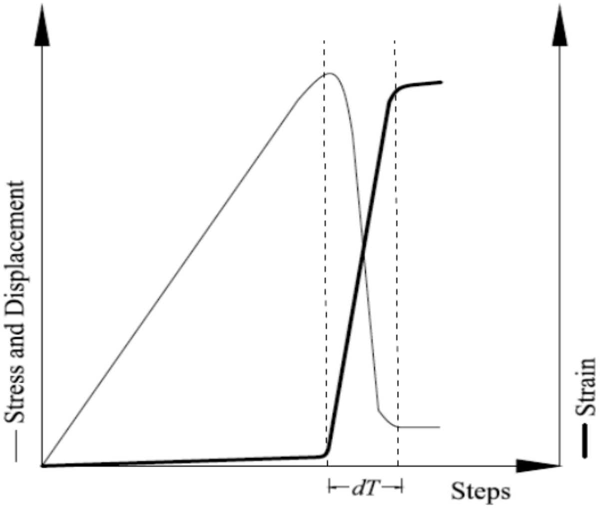

Fig. 3-60 The conceptual plot used for describing stability identifier performances.

Damping Work

PFC2D uses a damping mechanism to dissipate kinetic energy, so that a steady state solution may be arrived at within a reasonable number of calculation steps. The damping mechanism applies force to particles undergoing acceleration in the direction opposite that of motion. During failure, the damping mechanism applies larger forces in order to stabilize the failure process. Over a calculation time-step, the damping forces perform a quantifiable amount of work that can be summed over the entire model. Damping work is summed over each degree of freedom over all particles during a given time interval and the work is summed over the interval of failure.

The normalized damping work accumulated over the failure interval for each of the eight EPS tests is shown in Fig. 3-61. The normalizing is with respect to the drop in stress during the failure interval. As platen elastic modulus decreases from 50 GPa, the damping work does not change significantly. The damping work becomes increasingly higher as platen stiffness decreases beyond 5 GPa. This in accord with the previously established behavior that all tests with elastic modulus below 5 GPa are unstable with the 5 GPa test behaving in a quasi-stable manner.

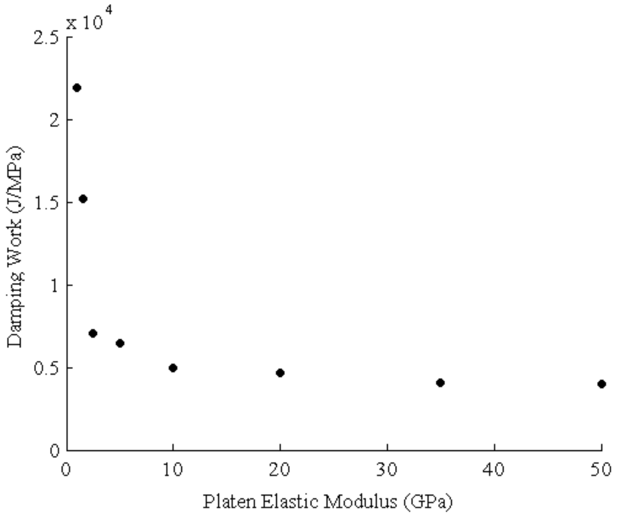

Fig. 3-61 Accumulated damping work during the failure interval in EPS tests.

Kinetic energy

The kinetic energy in PFC is calculated by summing the rotational and translational kinetic energies of all the particles during a single time step and these energy components are summed during each run. Both the maximum and the accumulated kinetic energy values were used as stability indicators.

Fig. 3-62 shows the instantaneous and cumulative kinetic energy during the EPS test with 5 GPa platens. During the loading phase of the test, the cumulative kinetic energy increases as a slow rate due to a consistent, low level of kinetic energy in the model. The kinetic energy increases when failure occurs, resulting in a sharp increase in the cumulative value of kinetic energy. After the majority of stress in the sample has been dissipated, the kinetic energy in the model reduces and the rate of change of cumulative kinetic energy decreases. The black vertical lines indicate the failure interval over which comparison is made to other tests. The failure interval is different for each test but the same for each indicator for a specific test.

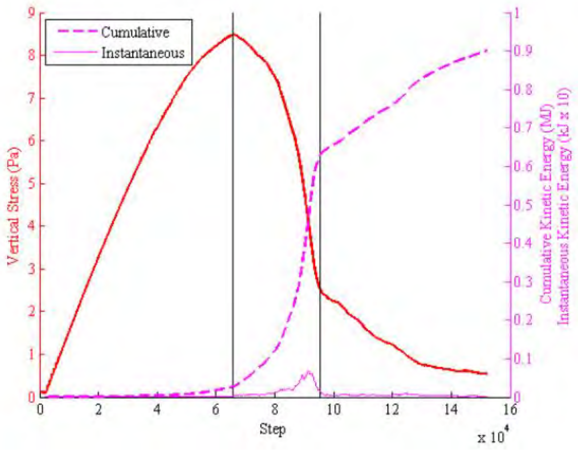

Fig. 3-62 Kinetic energy indicator results for EPS test with 5 GPa platens.

Fig. 3-63 shows the maximum kinetic energy during failure in log-scale as function of platen stiffness. The plot shows a well-defined increasing instability with reduced platen modulus. The three highest platen moduli exhibit consistent response, suggesting that this identifier may be particularly useful in identifying stable failure.

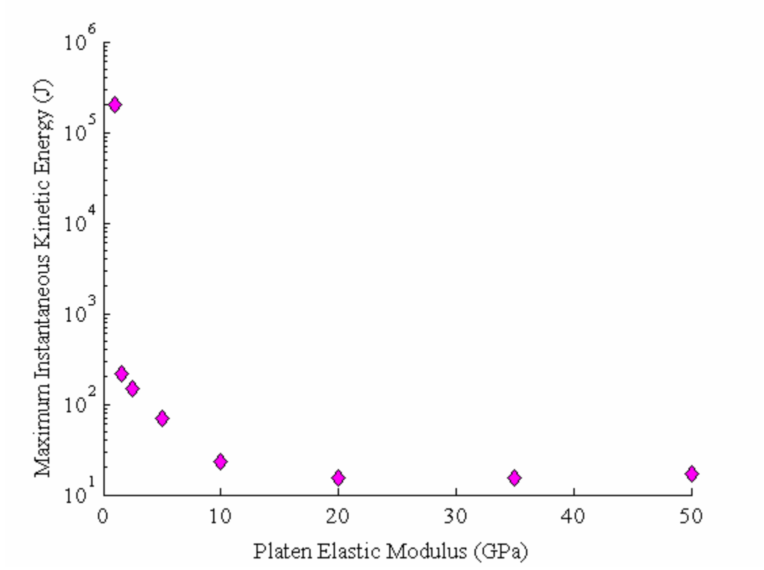

Fig. 3-63 Maximum instantaneous kinetic energy during failure in EPS tests.

Unbalance force

The mean unbalanced force is the average values of the out of balance force components for each particle. It is calculated for each time step and then averaged over all particles. The maximum mean unbalanced force and the cumulative amount are used as stability indicators. Figure 3.64 shows the results for the maximum instantaneous mean unbalanced force, which are similar to the maximum kinetic energy in that the most unstable failure has a significantly higher value than the next softest test, and the values for the most stable tests are consistent.

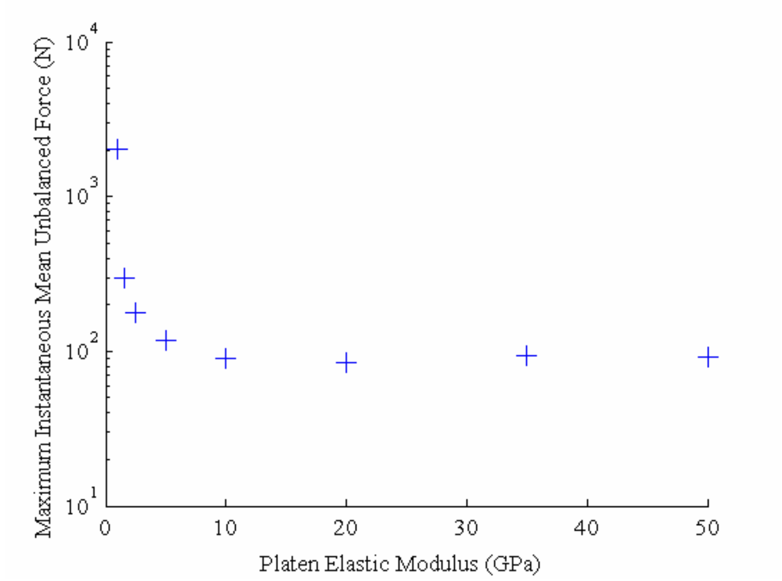

Fig. 3-64 Maximum instantaneous mean unbalanced force in EPS tests.

The maximum unbalanced force is shown in Fig. 3-65. The trend in maximum unbalance force is similar to kinetic energy and maximum mean unbalanced force although there exist some irregularity in the value for the stable failures.

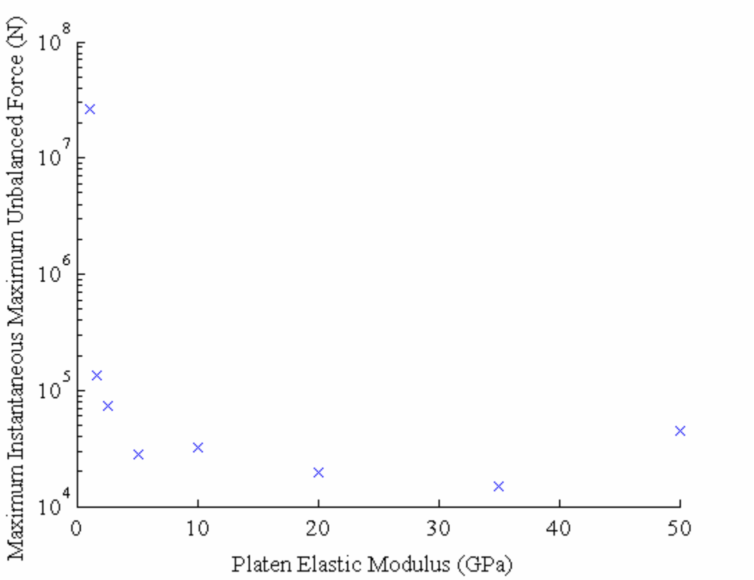

Fig. 3-65 Maximum instantaneous unbalanced force in EPS tests.

Contact softening

Contact softening during the failure interval for each EPS test is shown in Figure 3.66. The amount of softening is normalized with respect to the stress drop during the failure interval for each test respectively. The amount of contact softening remains consistent for the most stable failures. For unstable failures the amount of contact softening exhibits no particular trend as the two most unstable failure result in the most extreme cases of softening.

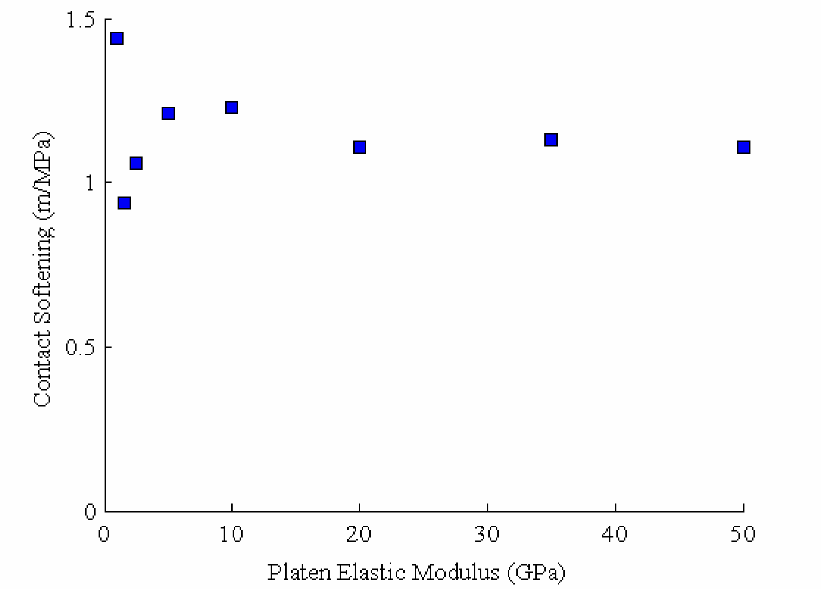

Fig. 3-66 Contact softening

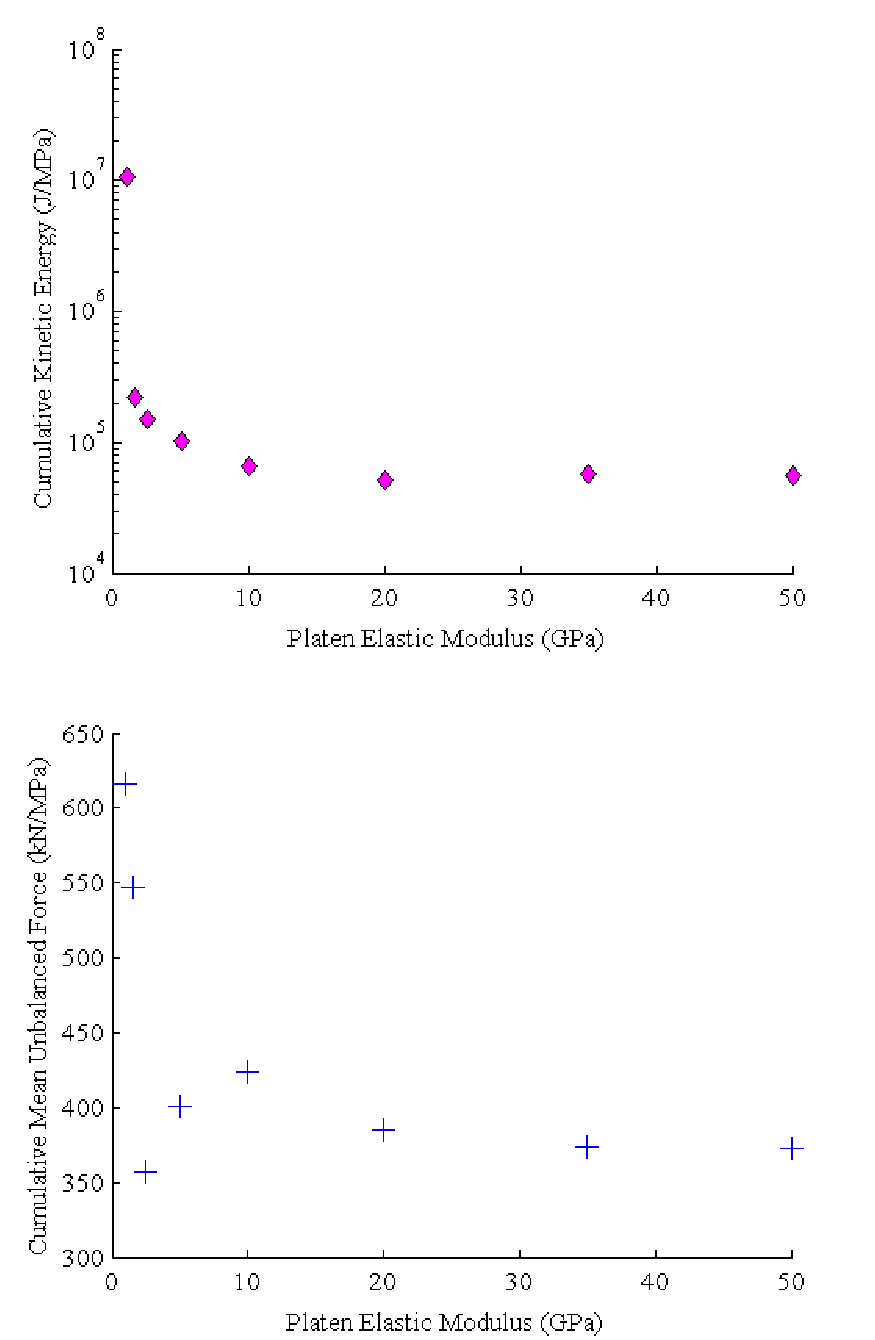

Fig. 3-67 Stability identifier performances during EPS tests

Fig. 3-67 shows the identifiers determined cumulatively. The cumulative kinetic energy is consistent for stable failures and increases as failure stability decreases. The cumulative mean unbalanced force generally shows the expected trends for stable versus unstable failure. Although, outlying results for the unstable failures using 2.5 and 5 GPa platens indicate that variability in mean unbalanced force in unstable failures can occur and caution should be exercised when using this indicator

Number of broken contacts

In a DSM, a contact between particles is deemed broken once the plastic displacement limit, U_{max}, is achieved at the contact. The number of contacts that have broken at a given time is used as a stability indicator.

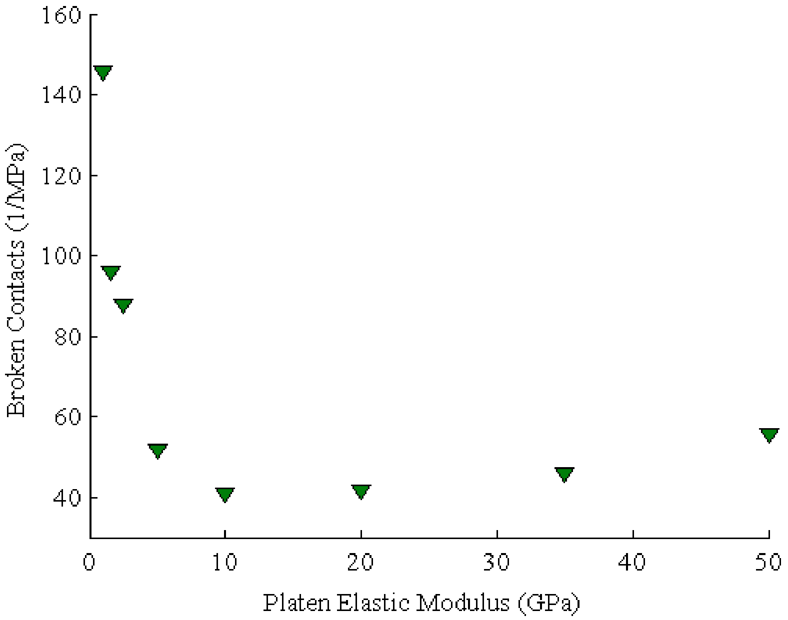

Fig. 3-68 Number of broken contacts in EPS tests.

EPS indicator results discussion

The indicators damping work, maximum mean unbalanced force, maximum kinetic energy and cumulative kinetic energy appear suitable indicators for tracking unstable failures. For each of these indicators, consistent values were measured for stable failures and as failure stability decreased, the indicator likewise increased to provide a qualitative measure of failure stability. Trends in cumulative values for kinetic energy, mean unbalanced force and maximum unbalanced force are helpful in describing failures in that the cumulative value contains information for the duration of the failure rather than a single calculation step. Each of these cumulative values performed with various levels of success in distinguishing between stable and unstable failures. The cumulative kinetic energy performs well in distinguishing between stable and unstable failure while the cumulative maximum unbalanced force loses the expression of instability for all unstable failures except for the 1 GPa test. The mean unbalanced force should be used with caution as there is some variability in the values of unstable failures. Additional work into methods of normalization may reveal the expected trends. Contact softening does not increase with decreasing failure stability but the variability in the value increases. Additional analysis could possibly reveal a trend similar to the other indicators, but is not pursued further in this study. Rather, since contact softening is a result of failure in contact bonds, it can be used to identify the locations and extent of damage in the model.

Stability identifiers in pillar models

The PFC based identifier methodology in the previous section is extended to failure stability analysis in coal pillars. A FLAC-PFC coupled model was developed (Fig. 3-68) and used for pillar tests. Five different width-to-height (w/h) ratio pillar models of w/h = 0.5, 1, 2, 3, and 4 were loaded beyond their strength. Each w/h ratio pillar test was repeated three times using three different elastic moduli of 5, 20, and 35 GPa for the roof and floor strata. Failure stability of pillars is assessed for all cases by considering loading stiffnesses against pillar performances in terms of selected stability identifiers.

The model geometry is shown in Fig. 3-68. A six-meter entry is simulated for each pillar size by adjusting the overall width of the model, M_w. Load is applied by a constant velocity boundary condition to the top and bottom boundaries. The FLAC2D grid is comprised of an inner region and an outer region so that a high-resolution grid can be used near the PFC2D inclusion while reducing memory cost with a grid graded in the vertical direction in the outer region.

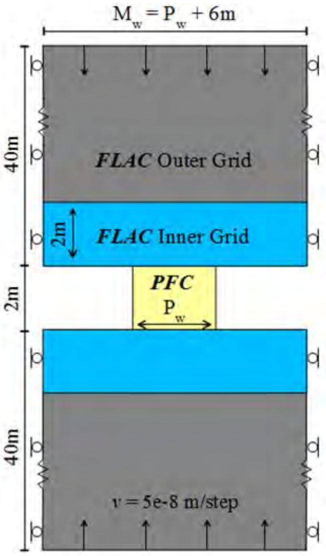

Fig. 3-69 Pillar strength test geometry and boundary conditions.

The stiffness of the roof and floor can be determined individually, using the spring equation given as

$$k = \Delta F_P \,/\, \Delta D$$

where ΔF_p is the change in force exerted on the roof or floor by the pillar and ΔD is the change in displacement in the roof and floor. ΔD is defined as the compression of the loading system averaged along the width of the pillar due to the moving, load application boundary and the reaction force at the boundary of the pillar. The pillar reaction force is calculated using average pillar stress and the cross sectional area of the pillar.

The local stiffness is calculated using ΔF_p and ΔD during the interval dT. Considering the roof and floor as a series of springs, one can calculate the local mine stiffness, LMS, by using the equation for stiffness of springs in series

$$LMS = \frac{k_r k_f}{k_r + k_f}$$

where k_r and k_f are the roof and floor stiffness respectively. The pillar post-peak stiffness is calculated using the equation

$$K_{PP} = \frac{E_{PP} A}{L} = \frac{\Delta\sigma A}{\Delta\varepsilon L}$$

where E_{PP} is the post-peak modulus, A is the cross sectional area of the pillar, and L is the height of the pillar. E_{PP} is determined according to the definition of Young’s modulus for $\Delta\sigma$ and $\Delta\varepsilon$ during the softening interval dT.

Results from nine pillar tests are organized into three plots. Each plot contains the stress-strain behavior of w/h =1, 2, and 3 pillar each loaded by 5, 20 and 35 GPa elastic modulus systems. Figs. 1.69, 1.70, and 1.71 show the results.

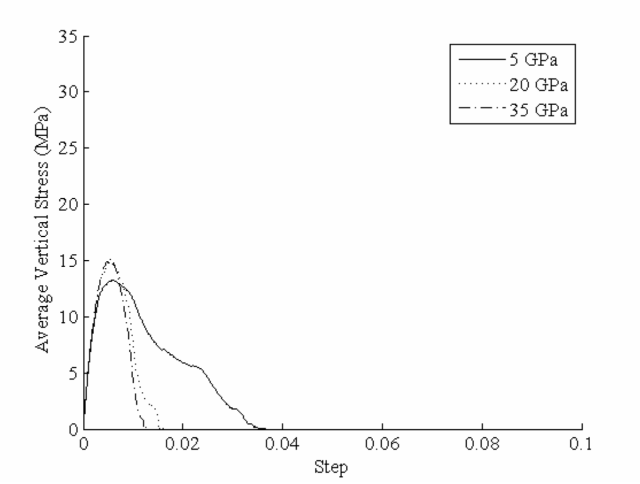

Fig. 3-70 Stress-strain curves for w/h = 1 pillar tests.

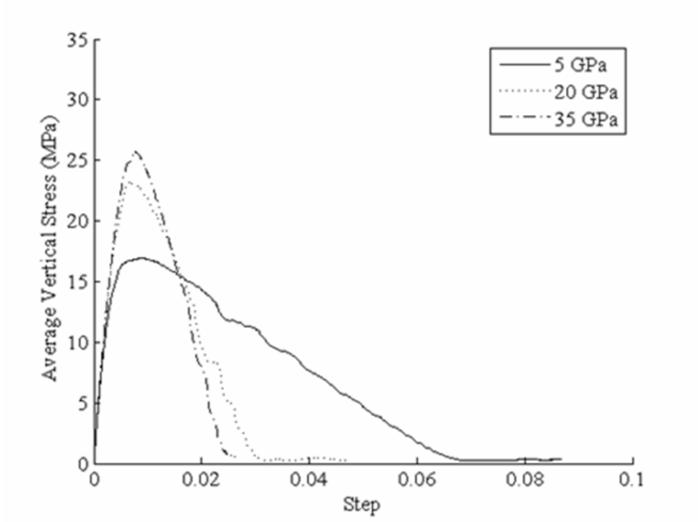

Fig. 3-71 Stress-strain curves for w/h=2 tests.

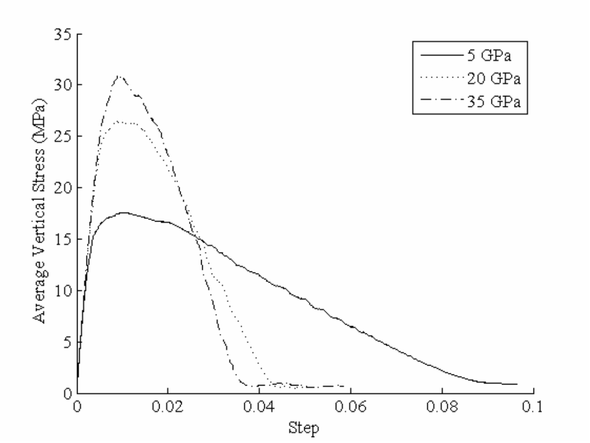

Fig. 3-72 Stress-strain curves for w/h=3 tests.

Each curve in a plot shows how pillar stress increases during the loading phase of the tests and then as the pillar fails, stress is reduced. Pillar strength is dependent upon the pillar w/h and the loading system stiffness. As pillar w/h increases the strength of the pillar increases, and as loading system stiffness decreases the pillar strength decreases. In the post-peak region, the post-peak modulus is dependent upon both the pillar w/h ratio and the loading system stiffness. As pillar w/h/ increases, the post-peak modulus decreases and as loading system stiffness increases the post-peak modulus increases. A significant change in post-peak behavior is apparent in each of the 5 GPa tests.

The displacements of the loading system in each of the nine tests are shown Figs. 3.72, 73, and 74 for the w/h = 1, 2, and 3 pillars. Loading system displacement increases during the loading phase of the tests and then decreases as the pillar fails. Displacement at the point of failure is higher when elastic modulus of the loading system is low and increases as the pillar size increases. In the post peak region, the 5 GPa tests show a fast decrease in loading system displacement, while tests with 20 and 35 GPa loading system exhibit a more gradual decrease in loading system displacement.

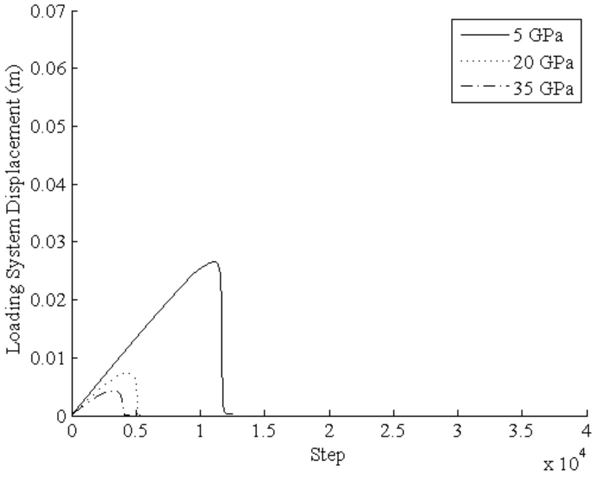

Fig. 3-73 Loading system displacements for width to height ratio one pillar tests.

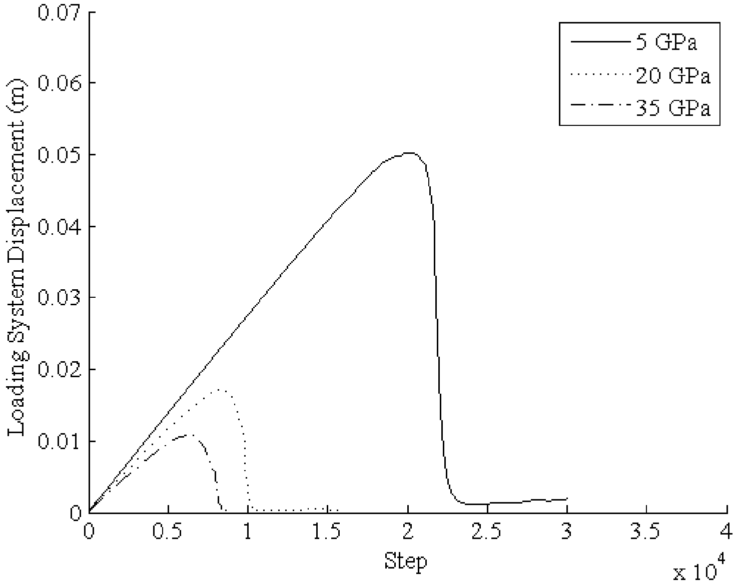

Fig. 3-74 Loading system displacements for width to height ratio two pillar tests.

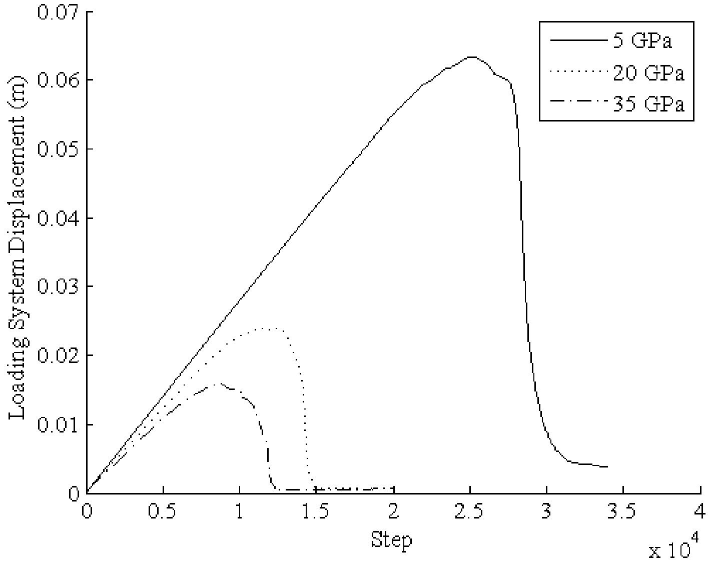

Fig. 3-75 Loading system displacements for width to height ratio three pillar tests.

Effect of pillar w/h ratio and loading stiffness on failure stability

Using data from the stress-strain and displacement plots, failure stability of different w/h ratio pillars can be assessed. Similar to the EPS tests, sudden rebound of the loading system (Figs. 2.3 and 3.54) should indicate unstable failure. A sudden rebound of the loading system can be detected by comparing the measured post-peak stiffness of the pillar to the loading system stiffness during failure. If these two values are similar, unstable failure is assumed to have occurred. Fig. 3-76 shows measurements of loading system stiffness and pillar post-peak stiffness during the failure interval (Fig. 3-60) for each test. Stability of the failure is determined by comparing the loading stiffness and post-peak stiffness for each test. The 20 GPa and 35 GPa tests show consistent difference between pillar behavior and loading system stiffness measurements indicating stability of pillar failures for all six tests. The 5 GPa tests show coincident values, indicating unstable failure for all three pillar sizes.

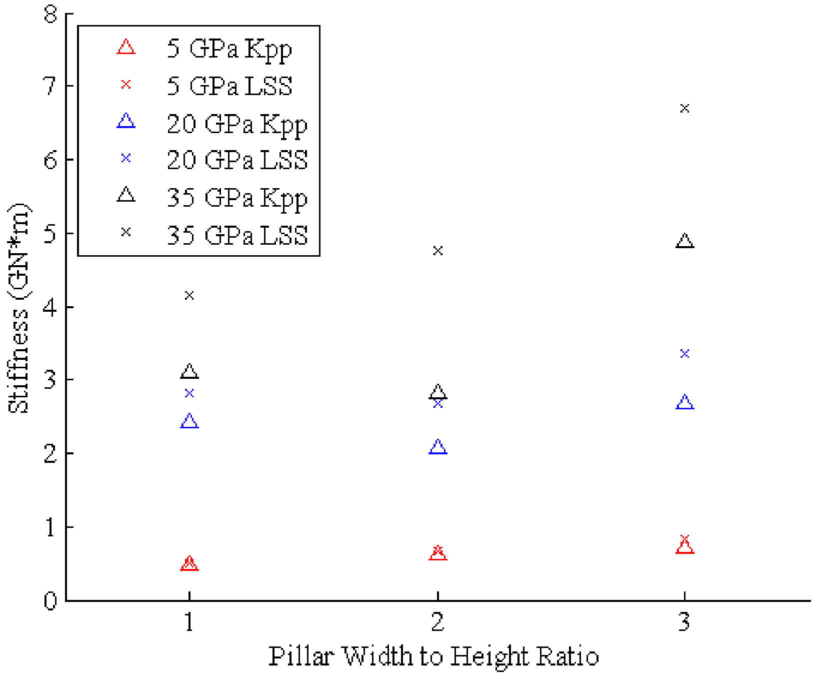

Fig. 3-76 Pillar post-peak stiffness (Kpp) and loading system stiffness (LSS) measurements.

Histories of nine different identifiers are recorded during each of the nine pillar tests. They are, damping work, kinetic energy, mean unbalanced force, maximum unbalanced force, contact softening, and number of broken contacts, all of which are plotted against pillar w/h ratio. All indicators are presented as a cumulative sum, although kinetic energy, mean unbalanced force, and maximum unbalanced force are also shown incrementally.

The results for stability indicator analysis are shown in Figs. 3.77 and 3.78. Each plot contains results for one indicator for each of the nine pillar tests.

The 5 GPa test results are given a grey colored marker and the 20 and 35 GPa tests are given black markers. This is done to signify that the 5 GPa tests resulted in unstable failures while the 20 and 35 GPa tests resulted in stable failures. Maximum value and cumulative results are provided for kinetic energy, mean unbalanced force and maximum unbalanced force. Damping work and contact softening, and broken contacts are cumulative values only. The cumulative values are each normalized by the stress drop during failure and the cross sectional area of each pillar, where a pillar width to height ratio of one equals 4 m^2, pillar width to height ratio of two equals 8 m^2, and pillar width to height ratio of three equals 12 m^2.

Damping work

Figure 3.76 shows damping work for the pillar tests. When unstable failure occurs the damping work is markedly increase, while for both the stable failures of each width to height ratio, the damping work is similar. Despite the normalization with respect to both stress drop and pillar size, the damping work is higher for larger pillars. As with the EPS tests, a larger amount of damping work suggests that the failures are more unstable.

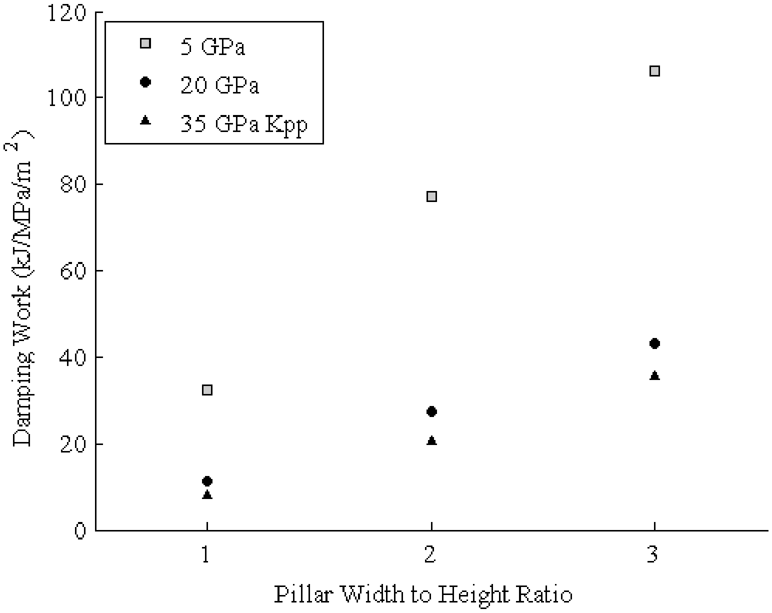

Fig. 3-77 Damping work in pillar strength tests.

The results from the remaining eight identifiers are given in Fig. 3-78. The identifiers maximum instantaneous kinetic energy, maximum instantaneous mean unbalanced force, and maximum unbalanced force show a lesser degree of difference between stable and unstable cases than the Damping work. Also, the maximum mean unbalanced force decreases for larger pillars. This likely bias is the result of averaging over a larger number of particles. These indicators contain model information for one calculation step, and therefore should be used with caution and in conjunction with other identifiers.

Cumulative values for kinetic energy, mean unbalanced force, and maximum unbalanced force express the failure stability of the model better because information is contained from the entire duration of failure. The cumulative kinetic energy describes the total amount of energy translated into motion that was initially stored in the specimen and loading system as strain energy. The kinetic energy increases drastically for unstable failures while values for stable failures are grouped at a noticeably lower magnitude. The cumulative mean unbalanced force shows a similar behavior only the stable values are grouped more closely.

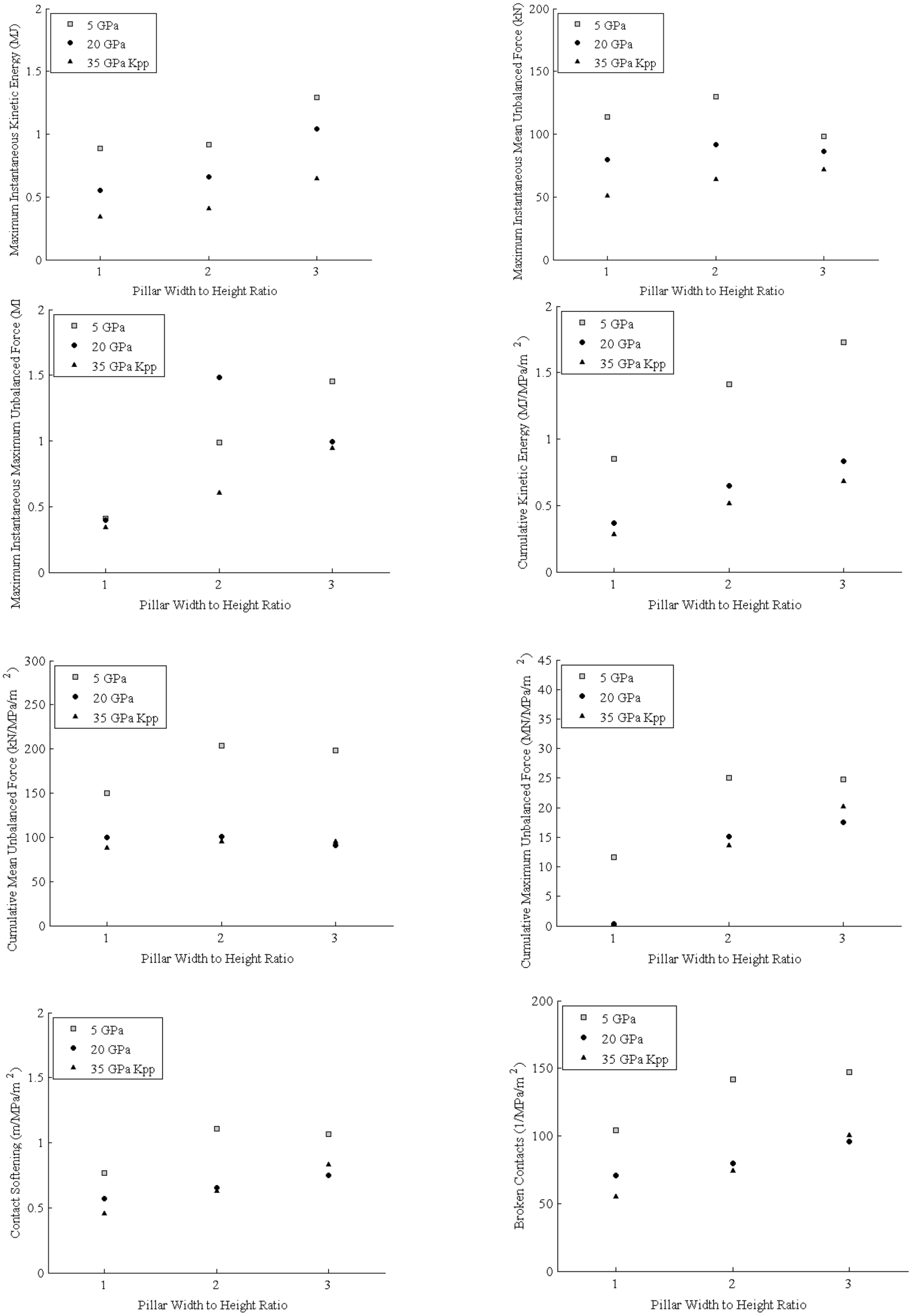

Fig. 3-78 Performance of the stability identifiers during failure of small w/h ratio pillars.

It is important to note that, as model size increases the number of elements over which the mean is averaged also increases, causing the mean unbalanced force tapering off. The values for stable failures decrease slightly as the model size increases. The cumulative maximum unbalanced force exhibits similar behavior, but values for stable cases increase for larger pillars. This trend suggests that for larger assemblies the maximum unbalanced for may not be able to clearly distinguish stable and unstable failure, but additional testing of larger pillars would need to be performed to verify this.

The cumulative amount of contact softening describes the plastic displacement of the model on the contact level. Contact softening distinguishes between stable and unstable failures in that stable failures for similar geometries exhibit similar amounts of contact softening while the unstable failures display a larger amount of contact softening. Although, as pillar size increases for unstable failures the amount of contact softening ceases to increase. Once again, additional tests on larger pillars may reveal additional features to the trend.

The number of broken contacts is the number of contacts that have reached the softening limit. Broken contacts are typically thought of as cracks in DEM models. Due to the softening component, this definition is debatable, but none the less the location of a broken contact identifies a location of significant damage in the model. The normalized number of broken contacts is consistently higher for unstable failures and there exists a large gap between closely grouped stable failures and the unstable failures. As with mean unbalanced force and softening identifiers, the number of broken contacts levels off as pillar size increases for unstable failures.

Grid based measurement technique

In the DSM version of PFC, the damage accumulates in the contacts before they are deleted an additional technique for observing damage is necessary. A grid based measurement technique is implemented to observe the behavior of the contact softening and damping work on a local level. To track contact softening and damping work spatially, a fictitious grid that is comprised of square pixels is superimposed onto the PFC assembly. The square pixels are 0.1 m on a side and grid resolution is kept constant in each model as model size changes. Each particle and contact is permanently assigned to a pixel at the beginning of the simulation, thereby ignoring effects of pixel-to-pixel movement. Irregular values at the model’s boundaries, due to empty space in the pixels, have been found to be irrelevant to model behavior and can also been ignored.

Fig. 3-79 compares the damping work plots of a stable and unstable failures triggered by a single mine step ahead of an advancing mining face. The image reveals a possible new failure surface further into the pillar than the most inner failure surface seen before the unstable mining step. Also, the magnitude of the damping work performed along the new failure surface far exceeds the values seen in the unstable mining step.

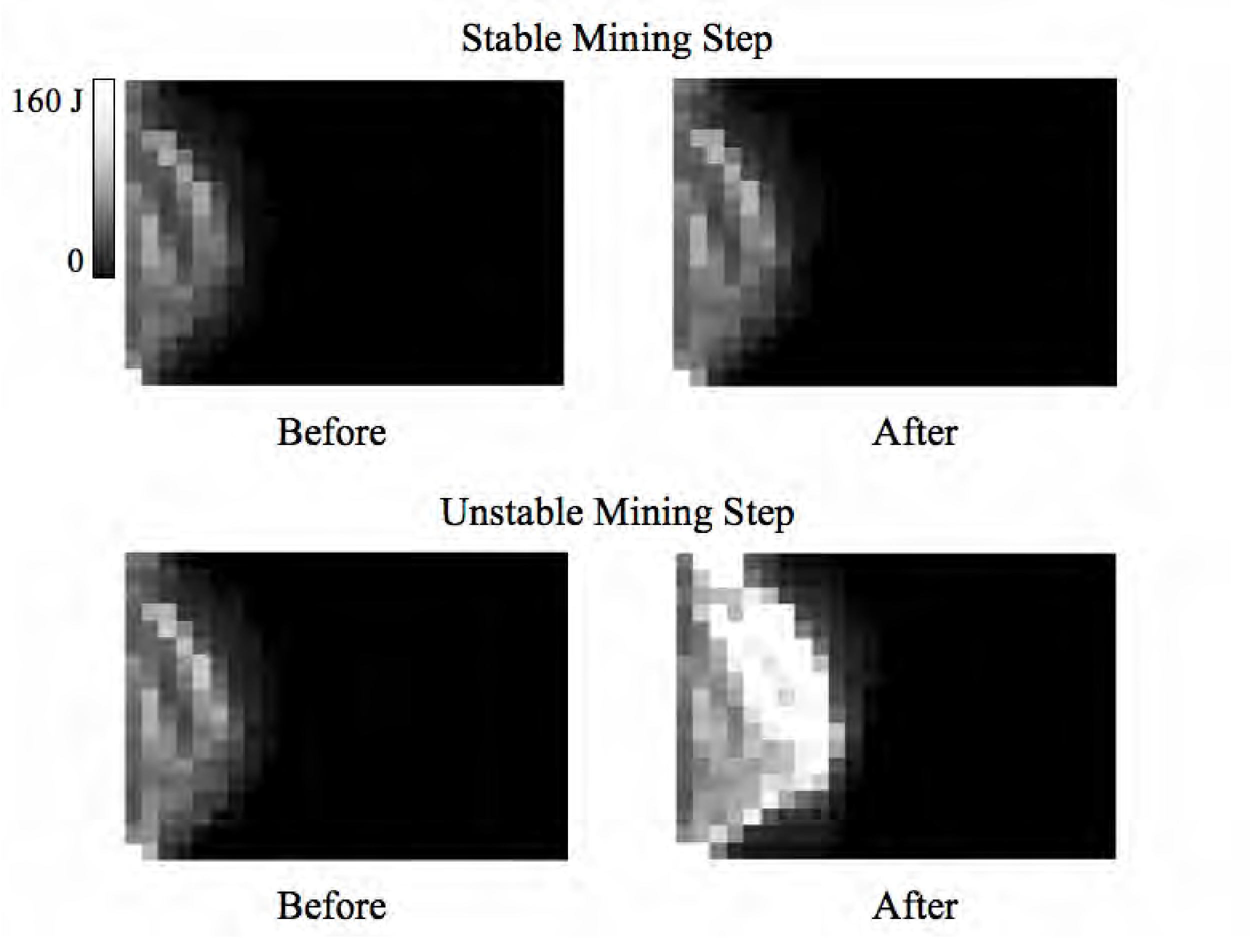

Fig. 3-79 Damping work in the rib during the ISP test

4. CONCLUSIONS

The numerical modeling studies on failure stability provide significant insight into the mechanisms of unstable failures encountered in deep coal mines. The advances made by the research efforts have given additional capacity to these models so that unstable failures may be assessed through the total excess energy which is released as a consequence of instability. The studies introduce numerical identifiers that can be used for evaluating failure stabilities in coal mines. A new methodology was also developed for assessing unstable failure intensities between different mine layouts.

Unstable failure was initiated within a series of FLAC3D explicit finite difference simulations using a comparatively soft loading system to fail a representative brittle coal specimen. It was shown that rapid dynamic motion resulting from quasi-static loading could be used for identifying instabilities within the simulated coal specimen. Maximum unbalanced forces, accelerations, velocities, and shear strain rates were all found to correlate well with the onset of unstable failure, as confirmed through the stress-strain behavior of the specimen. These tests were repeated under triaxial confinement conditions and compared against a perfectly plastic Mohr-Coulomb coal specimen under identical loading. It was found that an analysis of the proposed instability identifiers led to a clear distinction between stable and unstable failure results. The continuum model in FLAC3D provided a useful tool for assessing the likelihood and magnitude of unstable failure assuming a pre-defined brittle response for a calibrated rockmass. Localized or small magnitude unstable failures may also be assessed using this method.

The excess energy calculation provided a rational method for analyzing the bump-potential of room-and-pillar and gateroad layouts. During tributary area loading of the three-dimensional models, the smallest pillar geometries released the highest magnitudes of excess energy as is consistent with the scenario of a massive collapse of undersized pillars. In the two-dimensional gateroad, the excess energy increased with increasing pillar widths for the unstable, soft rockmass conditions. Additional testing of the energy balance is required to calibrate the plastic work consumed during unstable pillar failure to match the approximate values derived from in situ pillar failures. Future backanalysis studies should be conducted to validate the magnitudes of excess energy in the FLAC3D models against measures of the total kinetic energy released in historical cases of coal bumps.

A UDEC-based methodology was introduced to perform numerical simulations of unstable shear failures of large discontinuity planes triggered by advancing underground excavations. The results were in accordance with the stiffness criterion of Rice [48] and Salamon [50] such that for an unstable failure to occur; the stiffness of the loading system has to be less than the discontinuity post-peak stiffness. The CY joint model is reasonably capable of simulating stable and unstable shear failures of discontinuities loaded by a mining process. Using this model, it was confirmed that mining changes loading stiffness and stress distribution in the surrounding rock mass which lead to both stable and unstable shear failures along discontinuities. The signatures of unstable failures include sudden, discontinuous changes in shear stress and displacements along the discontinuity as compared to smoother and more gradual responses in the case of stable failures. As normal stress on the discontinuity increases, the proneness and intensity of unstable shear failures were observed to also increase. The proneness and intensity of unstable shear failures increase with increasing excavation extent, decreasing distance between the discontinuity and excavation, and decreasing elastic modulus of the rockmass. The deconfining effect of mining faces on the failure stability of a nearby discontinuity was shown to potentially lead to unstable compressive failures at mining faces and sidewalls which may cause rockburst events. The existence of weak regions and barriers at the interfaces can result in unstable compressive failures at mining faces. Interfaces with loose, cohesionless infill materials can be problematic for the management and control of rockburst problems.

The discrete element model Particle Flow Code (PFC) was used for the analysis of failure stabilities in underground coal mines. Compared to the continuum models, discrete element models have the advantage of inducing explicit fracturing into the modeled material. According to the literature, applications of discrete element models to post-peak behavior studies are rare and are likely to have never been previously used for failure stability analyses. Initial validation studies had to be carried out to assess the applicability of the code for modeling failure stability. It was found that the PFC displacement softening contact model is better suited than the more commonly used bonded particle contact model, thus the former was selected for the studies. As in the case of FLAC modeling, stability indicators were developed and tested on their ability in distinguishing stable and unstable failures. Failure stability studies were conducted for the cases of unconfined compression tests, slender pillar compressive strength tests, and large in situ pillar tests which also incorporated progressive mining induced failures. Additionally, cumulative indicators were developed as failure stability identifiers which in some cases were found to better distinguish stable and unstable failures as they consider the localized regions of rock throughout failure rather than the entire model for a single calculation step. For the unconfined compressive strength and small pillar test cases, the damping work and kinetic energy were good indicators of unstable failures. Some indicators are affected by the size of the pillars; typically the difference in unbalanced force was somewhat less in large pillars. The change in particle bond length was found to not as clearly distinguish between stable and unstable failures, although this indicator was useful in providing information on the location and extent of damage in the model. Grid based visual measurements were introduced as an additional failure stability indicator which showed larger, more localized measurements of instability for unstable failures than in the cases of stable failures.tests, which incorporated also progressive mining induced failures. Additionally, cumulative indicators were developed as failure stability identifiers. In some cases, these were found to better distinguish stable and unstable failures as they consider the failure regions rather than a single calculation step. For the unconfined compressive strength and small pillar test cases, the damping work and kinetic energy identifiers were good indicators of unstable failures. Some indicators are affected by the size of the pillars, typically the difference in unbalanced force was somewhat less in large pillars, even though the small magnitude differences were consistent with the findings from damping work and kinetic energy indicators. The contact softening indicator was found to not as clearly distinguishing between stable and unstable failures, although this indicator was useful in providing information on location and extent of damage in the model. Grid based visual measurements were introduced as an additional failure stability indicator. Compared to damping work and contact softening, grid based measurement showed larger local values for unstable failures and similar values for stable failures.

References

1. Badr, S. [2004] Numerical Analysis of Coal Yield Pillars at Deep Longwall Mines, PhD Dissertation, Colorado School of Mines.
2. Bajpayee T.S, Schilling S.R. [2009] Stability mapping to examine ground failure risk: a field study at a limestone mine. In: Proceedings of the 28th International Conference on Ground Control in Mining. Morgantown; 28-30 July 2009. p. 135-42.
3. Barton, N. R. [1972] A study of rock-joint deformation. Int. J. Rock Mech. Min. Sci. 9, 579–602.
4. Barton N, Bandis S, and Bakhtar K. [1985] Strength, deformation and conductivity coupling of rock joints. Int. J. Rock Mech. Min. Sci. & Geomech. Abstr. 3: 121–40.
5. Bieniawski, Z. T. [1967]. Mechanism of brittle fracture of rocks, parts i, ii, and iii. Int. J. Rock Mech. Min. Sci. 4, 395–430.
6. Bolstad, D. D. [1990]. Keynote lecture: rockburst control research by the US Bureau of Mines. In Proceeding of the Second Symposium on Rockburst and Seismicity in Mines, Rotterdam, pp. 371–375. A. A. Balkema.
7. Bukowska, M. [2006]. The probability of rockburst occurrence in the upper Silesian coal basin area dependent on natural mining conditions. J. Min. Sci. 42 [6].
8. Cai, M. [2008]. Influence of stress path on tunnel excavation response – numerical tool selection and modeling strategy. Tunn. Undergr. Sp. Tech. 23, 618–628. CAMIRO-Mining-Division [1990]. Mining in burst-prone ground, Rockburst Research Handbook, Volume 1. CAMIRO Mining Division.
9. Caldwell, J. [2009] SME on Crandall Canyon and mining bumps. http://ithinkmining.com/2009/02/25/sme-on-crandall-canyon-and-miningbumps/, Accessed on 2/20/2013.
10. Cho, N., C. D. Martin, and D. C. Sego [2007]. A clumped particle model for rock. Int. J. Rock Mech. Min. Sci. 44, 997–1010.
11. Clark, F.R. [1928] Castlegate, Wellington, and Sunnyside quadrangles, Carbon County, Utah. US Geol. Survey Bulletin 193.
12. Coates, D. F. [1965]. Rock Mechanics Principles. Roger Duhamel, F.R.S.C. Cook, N. G. W. [1965a]. The failure of rock. Int. J. Rock Mech. Min. Sci. 2, 389–403.
13. Cook, N. G. W. [1965b]. A note on rockbursts considered as a problem of stability. J. South Afr. Int. Min. and Metallurgy 65, 437–446.
14. Cundall P.A, Hart RD [1984] Analysis of block test no. 1 inelastic rock mass behavior: phase 2—A characterization of joint behavior [Final Report]. Itasca Consulting Group Report, Rockwell Hanford Operations, Subcontract SA-957.
15. Cundall P.A., Lemos J.V. [1990] Numerical simulation of fault instabilities with a continuously-yielding joint model. In: Rockbursts and Seismicity in Mines, Fairhurst [ed.], Balkema, Rotterdam.
16. De Borst, R. [2001] Some recent issues in computational failure mechanics. International Journal for Numerical Methods in Engineering. vol 52:63-95.
17. DeMarco, M.J., Koehler, J.R., and Lu, P.H. [1988] Characterization of chain pillar stability in a deep western coal mine - case study. SME Annual Meeting, Phoenix, Arizona, January 25-28, 1988, Pre-print 88-76.
18. Flamand R, Archambault G, Gentier S, Riss J, Rouleau A. [1994] An experimental study of the shear behavior of irregular joints based on angularities and progressive degradation of the surfaces. In: Proceedings of the Can. Geotech. Conf., p. 253–62.

19. Garvey R, Ozbay, U: [2011] Computer aided calibration of PFC3D coal samples using a genetic algorithm. Proceedings of the 2nd FLAC/DEM Symposium, Melbourne, Australia
20. Gates, R. A., M. Gauna, T. A. Morley, J. R. O’Donnell-Jr., G. E. Smith, T. R. Watkins, C. A. Weaver, and J. C. Zelanko [2007]. Underground coal mine, fatal underground coal burst accidents. Report of investigation, Mine Safety and Health Administration, 1100 Wilson Boulevard, Arlington, Virginia, 22209.
21. Hagan, T. O., A. M. Milev, S. M. Spottiswoode, B. Vakalisa, and N. Reddy [1998]. Improvement of worker safety through the investigation of the site response to rockbursts [Draft Final Project Report ed.]. Safety in Mines Research Advisory Committee. 170
22. Haramy, K.Y., Hanna, K. and McDonnell, J.F.T [1984] Investigations of undergroundcoal mine bursts. Proceeding of the Fourth Conference on Ground Control in Mining (ICGCM).
23. Hedley, D. G. F. and J. E. Udd [1989]. The Canada-Ontario-industry rockburst project. Page 129, 661–672.
24. Hill, R. [1958] A general theory of uniqueness and stability in elastic-plastic solids. Journal of the Mechanics and Physics of Solids, vol. 6, 1958, pp. 236-249.
25. Iannacchione, A. T. and J. C. Zelanko [1995a]. Occurrence and remediation of coal mine bumps: a historical review. In Special Publication 01-95, NTIS No. PB95-211967, pp. 27–67. U.S. Department of the Interior, Bureau of Mines.
26. Iannacchione, A.T. and J. Zelanko. 1995. Occurrence and remediation of coal mine bumps: a historical review. In Proceedings of the Mechanics and Mitigation of Violent Failure in Coal and Hard-Rock Mines, U.S. Bureau of Mines Special Publication 01-95, 27-68.
27. Itasca Consulting Group Inc. [2010] FLAC [Fast Lagrangian Analysis of Continua in 2 Dimensions]. Version 6.0. Minneapolis, MN.
28. Itasca Consulting Group Inc. [2010] PFC2D [Partical Flow Code in 2 Dimensions]. Version 6.0. Minneapolis, MN.
29. Itasca Consulting Group Inc. [2010] 3DEC [3 Dimensional Distinct Element Code in 3 Dimesions], Version 4.1. Minneapolis, MN.
30. Itasca Consulting Group Inc. [2010] FLAC3D [Fast Lagrangian Analysis of Continua in 3 Dimensions], Version 4.0. Minneapolis, MN
31. Itasca Consulting Group Inc. [2010] PFC3D [Particle Flow Code in 3 Dimensions], Version 4.0. Minneapolis, MN.
32. Itasca Consulting Group Inc. [2010] UDEC [Universal Distinct Element Code in 2 Dimensions] Version 4.0. Minneapolis, MN.
33. Itasca-Consulting-Group [1987]. Evaluation of rockburst potential at the Hanford site. Technical report. Itasca-Consulting-Group [2010]. UDEC [Universal Distinct Element Code], Version 4.0. Minneapolis, MN: Itasca Consulting Group Inc.
34. Koehler, J.R., DeMarco, M.J., and Wuest, W.J. [1995] The critical pillar concept in yield pillar-based longwall gate road design. SME Annual Meeting, March 6-9, 1995, Denver, CO.
35. Krishnamurthy, R. and S. B. Shringarputale [1990]. Rockburst hazards in kolar gold fields. In Proceedings of the Second Symposium on Rockburst and Seismicity in Mines, Rotterdam, pp. 411–419. A. A. Balkema.
36. Kripakov, N. and Kneisley, R. [1992] Pillar design in bump-prone deep western U.S. coal mines. 11th International Conference on Ground Control in Mining, The University of Wollongong, N.S.W., pp. 72-83.

37. Leichnitz W. [1985] Mechanical properties of rock joints. Int. J. Rock Mech. Min. Sci. & Geomech. Abstr. 22: 313–21.
38. Lemos, J. V. [1987]. A distinct element model for dynamic analysis of jointed rock with application to dam foundations and fault motion. Ph. D. thesis, University of Minnesota.
39. Li, T., M. F. Cai, and M. Cai [2007]. A review of mining-induced seismicity in china. Int. J. Rock Mech. Min. Sci. 44, 1149–1171.
40. Li, Z., L. Dou, C. Lu, Z. Mu, and A. Cao [2008]. Study on fault induced rock bursts. J. China Uni. Min. Tech. 18, 321–326.
41. Mark, C. [2006] Extreme multiple seam mining in the central Appalachian coal fields. 2006 SME Annual Meeting March 27-29, St. Louis, Missouri, p. 7.
42. Mark, C. [2009] Deep cover pillar recovery in the US. 28th International Conference on Ground Control in Mining, Morgantown, WV, pp. 1-9.
43. Notley, K. [1984] Rock mechanics analysis of the Springhill mine disaster. Mining Science and Technology, vol. 1, no. 2, pp. 149-163.
44. Ortlepp, W. D. [2005]. Keynote lecture: Rasim comes of age-a review of the contribution to the understanding and control of mine rockbursts. In Y. Potvin and M. Hudyma [Eds.], Controlling Seismic Risk: Sixth International Symposium on Rockburst and Seismicity in Mines proceedings, Australia. Australian Centre for Geomechanics.
45. Osterwald, F.W. [1962] USGS relates geologic structures to bumps and deformation in coal mine workings. Mining Engineering, vol. 14, pp. 63-68, Apr. 1962
46. Pan, Y. S., Z. H. Li, and M. T. Zhang [2003]. Distribution, type, mechanism and prevention on rockburst in china. Chinese Journal of Rock Mechanics and Engineering 22 [11], 1844–1851.
47. Peperakis, J. [1958] Mountain bumps at the sunnyside mines. Transactions AIME, vol. 211, pp. 982-986, Sep-1958.
48. Rice, J. R. [1983]. Constitutive relations for fault slip and earthquake instabilities. Pageoph. 121, 443–475.
49. Salamon, M.D.G. and Munro, A.H. [1967] A study of the strength of coal pillars. J. S. Afr. Inst. Min. Metall. September 1967.
50. Salamon M.D.G [1974] Rock mechanics of underground excavations. Advances in Rock Mechanics, Proc. 3rd Cong. Int. Soc. Rock. Mech. 1B: 951-1099.
51. Schneider HJ. [1976] The friction and deformation behavior of rock joint. J. Rock Mech. 8: 169-84.
52. Wagner, H. [1974] "Determination of complete load deformation characteristics of coal pillars." In: Proceedings of 3rd ISRM Congress, Denver, Colorado, USA, pp. 1076-1081.
53. Whyatt, J. K., W. Blake, T. J. Williams, and B. G. White [2002]. Sixty years of rockbursting in the Coeur d' Alene district of Northern Idaho, USA: Lessons learned and remaining issues. In Proceedings of the 109th Annual Exhibit and Meeting, Society for Mining, Metallurgy, and Exploration, Volume 2, Phoenix, AZ, pp. 164–174.
54. Whyatt, J. K. and M. C. Loken [2009]. Coal bumps and odd dynamic phenomena – a numerical investigation. In The 28th International Conference on Ground Control in Mining, Morgantown, WV, pp. 175–180.

Publications

Ph. D. Theses

Garvey, R. J. [2013] A Study of Unstable Rock Failures using Finite Difference and Discrete Element Methods, Ph.D. Thesis, Colorado School of Mines.

Gu, R. [2013] Distinct Element Model Analyses of Unstable Failures In Underground Coal Mines, Ph.D. Thesis, Colorado School of Mines.

Kias, M. C. K. [expected Dec 2013] Micro-mechanical Behavior of Rock in Unstable Equilibrium, Ph.D. Thesis, Colorado School of Mines.

Papers

Gu, R. and Ozbay, U. [2013] Distinct element model analyses of unstable rock failures under shear and compressive loadings. Rock Mech. Rock Eng. Under review 2013.

Gu, R. and Ozbay, U. [2013] Distinct element model analysis of unstable shear failure of rock discontinuities in underground mining conditions. Int. J. Rock Mech. Min. Sci. 2013. In Press.

Gu R., Mustoe, G., and Ozbay U. [2013] Evaluation Of Two Discrete Element Models For Studying Unstable Rock Failure In Compression, 6th International Conference on Discrete Element Methods (DEM6). Colorado School of Mines.

Gu R, Ozbay U. [2013] Distinct Element Analysis Of Unstable Failure In Underground Mines, 6th International Conference on Discrete Element Methods (DEM6), Colorado School of Mines.

Garvey R, Ozbay U. [2013] Assessing Coal Bumps from Excess Energy in Finite Difference Models. The 32nd International Conference on Ground Control in Mining, Morgantown.

Kusaka A, Garvey R, Ozbay, U. [2013] A Study of the Influence of Tunnel Shape on Rockburst Proneness Using Numerical Modeling, The 47th US Rock Mechanics / Geomechanics Symposium, San Francisco, CA, USA, 23-26 June.

Gu R, Ozbay, U. [2013] Distinct Element Analysis of Discontinuity Stable and Unstable Shear Failure, The 47th US Rock Mechanics / Geomechanics Symposium, San Francisco, CA, USA, 23-26 June.

Kias E.M.C, Ozbay U. [2013] Modeling unstable failure of coal pillars in underground mining using the discrete element method, The 47th US Rock Mechanics / Geomechanics Symposium, San Francisco, CA, USA, 23-26 June.

Gu R, Ozbay U. [2012] Distinct Element Model Analysis of Unstable Failure of Rock Discontinuities. The 46th US Rock Mechanics / Geomechanics Symposium, Chicago, IL, USA, 24-27 June 2012.

Garvey R, Ozbay U. [2012] Identifying Unstable Failure in Brittle Rock using the Finite Difference Method. The 46th US Rock Mechanics / Geomechanics Symposium, Chicago, IL, USA, 24-27 June 2012.

Gu R, Ozbay U: [2012] Distinct Element Analysis of Unstable Failure and Consideration of Local Mine Shear Stiffness. Topical Issues of Rational Use of Natural Resources, St. Petersburg State Mining University, April 25-27, 2012

Garvey, R., and U. Ozbay. [2011]. Computer Aided Calibration of PFC3D Coal Samples Using a Genetic Algorithm. In Proceedings of the 2nd International FLAC/DEM Symposium, Melbourne 14-16 February 2011. Eds. Sainsbury et. al, 493–499. Itasca, Minneapolis.

Kias, E. M. C., R. Gu, R. Garvey, and U. Ozbay. [2011]. Modeling Unstable Rock Failure during Uniaxial Compressive Strength Test. Proceedings of the 45th US Rock Mechanics/Geomechanics Symposium, San Francisco 26-29 June 2011. Ed. Iannacchione, A., 825-833. Curran Assoc. Inc. New York.